

RICE UNIVERSITY

**Snapshot Hyperspectral Imaging for Complete Fundus
Oximetry**

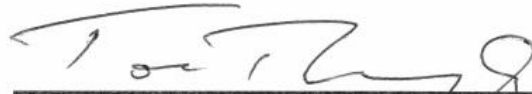
by

Jason G Dwight

A THESIS SUBMITTED
IN PARTIAL FULFILLMENT OF THE
REQUIREMENTS FOR THE DEGREE

Doctor of Philosophy

APPROVED, THESIS COMMITTEE



Tomasz S. Tkaczyk, Chair
PhD, Associate Professor in
Bioengineering, Associate Professor in
Electrical and Computer Engineering, Rice
University



Michael R. Diehl
PhD, Associate Professor in
Bioengineering, Associate Professor in
Chemistry, Rice University



Richard G. Baraniuk
PhD, MS, Victor E. Cameron Professor,
Rice University



Christina Y. Weng
MD, MBA, Assistant Professor in
Ophthalmology, Baylor College of
Medicine

HOUSTON, TEXAS
April 2017

ABSTRACT

Snapshot Hyperspectral Imaging for Complete Fundus Oximetry

by

Jason G. Dwight

In this work, a snapshot hyperspectral imager capable of tuning its average spectral resolution from 22.7 nm to 13.9 nm in a single integrated form is presented. The principle of this system will enable future snapshot systems to dynamically adapt to a wide range of imaging situations. Additionally, the system overcomes datacube size limitations imposed by detector array size limits. The work done in this thesis also advances oximetry of the retina using data collected by the Image Mapping spectrometer (IMS), a snapshot spectrometer. Hyperspectral images of the retina are acquired, and oximetry of individual vessels in four diseased eyes is presented. Further, oximetry of the entire fundus is performed using a novel algorithm with data collected with the IMS. We present oxyhemoglobin concentration maps of the eye and demonstrate oxygen sensitivity of the maps by comparing normal and diseased eyes. The aim of this work is to advance the general capabilities of snapshot hyperspectral imagers and to advance the integration of retinal oximetry into the standard ophthalmology instrument repertoire.

Acknowledgments

My first and foremost acknowledgement goes to Dr. Tomasz Tkaczyk, for his patience, help, and the contributions he has made to my life over the course of my PhD. I have appreciated his friendship and mentorship even when I struggled at various aspects in my work.

I am also deeply indebted to committee members, Dr. Richard Baraniuk, Michael Diehl, and Christina Weng. It has been an honor to have worked with you all. Thank you for taking time out of your lives to enrich mine with guidance and friendship.

Thank you Michal Pawlowski for all of your help. It has been a pleasure to co-author with you. I have enjoyed our conversations and friendship greatly. I would also like to give thanks to lab members, past and present: Thuc-Uyen Nguyen, Hamin Jeon, Cindy Wong, John Gawedzinski, Ye Wang, Isabella Yang, Alessandra Forcucci, Adam Shadfan, Matt Kyrish, and Brian McCall.

Funding: This work is supported by the National Institute of Health (R01CA186132 and R21EB016832) and the IBB Medical Innovation Grant

Contents

Acknowledgments	iv
Contents	v
List of Figures	viii
List of Tables	xi
List of Equations	xii
Nomenclature	xiii
Introduction	1
1.1. Objectives and Specific aims	1
1.2. Overview.....	2
Background	5
2.1. Motivation and Significance	5
2.2. The Physiology of the Human Eye.....	6
2.3. Age-related Macular Degeneration (AMD)	9
2.4. Spectrometers	11
2.5. Hyperspectral Imaging (HSI).....	12
2.6. Snapshot Hyperspectral Imaging (sHSI)	13
Construction of a Tunable Snapshot Imaging Spectrometer*	17
3.1. Introduction.....	18
3.2. General Principle	22
3.2.1. Integral Field Spectroscopy with Lenslet Arrays.....	22
3.2.2. Tunability Principle of LATIS	25
3.3. Instrument Description	28
3.4. Imaging Results	33
3.4.1. Calibration and Reconstruction	33
3.4.2. Spectral Resolution measurements for LATIS	35
3.4.3. Spectral Accuracy of LATIS.....	37
3.5. Bead Imaging Experiments with LATIS.....	38
3.6. Fluorescence Imaging with “Static” LATIS.....	40

3.7. Discussion	43
Oximetry of Retinal Vessels using the Image Mapping Spectrometer*	46
4.1. Introduction.....	47
4.2. Materials and Methods	50
4.2.1. Image Mapping Spectrometry	50
4.2.2. Oximetry	52
4.2.3. Oximetry Maps	55
4.2.4. Patients	56
4.3. Results	56
4.3.1. Hyperspectral Images	56
4.3.2. Oximetry	58
4.3.3. Oximetry map	61
4.4. Discussion	62
Oxygen signal extraction and the measurement of oxyhemoglobin concentration from heterogeneous fundus tissue using hyperspectral Image Mapping Spectrometry	66
5.1. Introduction.....	67
5.2. Methods	70
5.2.1. IMS and Fundus Camera setup.....	70
5.2.2. Oxygen signal Extraction.....	71
5.2.3. Non-negative matrix factorization algorithm.....	74
5.2.4. Finger oximetry model.....	75
5.2.5. Oxyhemoglobin radial maps	77
5.2.6. Patients	80
5.3. Results	81
5.3.1. Composite images of eyes.....	81
5.3.2. Finger Oximetry	82
5.3.3. Non-negative matrix factorization	85
5.3.4. Oxyhemoglobin radial maps	90
5.4. Discussion	92
Conclusion	95
References	99

List of Figures

Figure 2-1. Branches of the ophthalmic artery.....	7
Figure 2-2. Cross-section of the retina.....	8
Figure 2-3. Conceptual representation of the 4 data acquisition methods for imaging spectrometers	13
Figure 2-4. System architectures for snapshot HSI.....	16
Figure 3-1. Lenslet array principle as an IFS for microscopy	24
Figure 3-2. The tunability principle of LATIS.....	27
Figure 3-3. A range of tuning settings in an example LATIS system	28
Figure 3-4. Illustrated schematic for LATIS.....	30
Figure 3-5. Lenslet array mount and characterization of the lenslet array surface.....	31
Figure 3-6. Raw unprocessed images of dispersed sub-pupil images acquired with the Retiga EXi.....	32
Figure 3-7. A photograph of the static LATIS system.....	33
Figure 3-8. Reconstruction of images for LATIS.....	34
Figure 3-9. The mean spectral response of LATIS.....	36
Figure 3-10. Spectral accuracy comparison of 1-nm filters between LATIS and an Ocean Optics USB4000 spectrometer.	38
Figure 3-11. Fluorescent beads measured with LATIS.	39
Figure 3-12. BPAE cell imaging with the static LATIS.	41
Figure 3-13. Quantum dot imaging of sectioned lymph node mouse tissue using the static LATIS.	42
Figure 4-1. The IMS mounted onto a TRC-50EX fundus camera.....	52

Figure 4-2. The normalized extinction coefficients of oxygenated and deoxygenated blood.....	55
Figure 4-3. Selected spectral channels from an image stack acquired from a patient with AMD.	57
Figure 4-4. Composite images of 8 spectral channels.	58
Figure 4-5. Oxygen saturation calculations for two 50-pixel regions.	60
Figure 4-6. Oxygen saturation map of the patient with AMD and borderline glaucoma.	61
Figure 5-1. IMS setup on Fundus.....	71
Figure 5-2. The calculated absorbances in an eye by dividing 4 regions by a low oxyhemoglobin region (R4).	74
Figure 5-3. Recorded image using the IMS of the finger oximetry setup.....	77
Figure 5-4. Noise reduction of the absorbance spectrum.....	78
Figure 5-5. Segmentation of a radial map for retinal tissue oximetry.	79
Figure 5-6. Example absorbance spectra from a normal eye, pointing out the isobestic point at 500 nm and the peak oxygen signal between 540-580 nm..	80
Figure 5-7. Composite images of patient eyes.....	82
Figure 5-8. Finger oximetry absorbance data.....	83
Figure 5-9. Plot of finger OD difference vs time and oxygen saturation vs time.	84
Figure 5-10. Standards curve based off of finger oximetry data.	85
Figure 5-11. Spectral decomposition using NMF for all eyes.....	87
Figure 5-12. Variance between spectral endmember 2 after 50 repetitions of NMF.	88
Figure 5-13. Results of NMF decomposition for 5 segments in all 4 eyes.....	89

Figure 5-14. Mean absorbance from the 5 radial regions in the normal eye and th	90
Figure 5-15. OD NMF maps for all eyes.....	91
Figure 5-16. HbO₂ concentration maps for all eyes.....	92

List of Tables

Table 3-1. Spectral response of LATIS	36
Table 4-1. Average oxygen saturation in 4 diseased eyes	59

List of Equations

Equation 3-1. Linear Dispersion	25
Equation 3-2. PSF width in Lenslet system	25
Equation 4-1. Absorbance of whole blood.....	53
Equation 4-2. Conversion from transmittance to absorbance	53
Equation 4-3. Transmittance approximation in the eye	53
Equation 5-1. Reflectance in eye.....	71
Equation 5-2. Division of the reflectance from eye regions	72
Equation 5-3. Simplification of Equation 5-2	72
Equation 5-4. Weighted abundances of different chromophores.....	73
Equation 5-5. Cost function for NNMF.....	74
Equation 5-6. Oxygen saturation	84

Nomenclature

LATIS	Lenslet Array Tunable Imaging Spectrometer
IMS	Image Mapping Spectrometer
HSI	Hyperspectral Imaging
HFM	Hyperspectral Fluorescence Microscopy
sHSI	Snapshot Hyperspectral Imaging
SNR	Signal-to-Noise Ratio
FOV	Field-of-View
NA	Numerical Aperture
AMD	Age-related Macular Degeneration
IFS	Integral Field Spectroscopy
IFS-L	Integral Field Spectroscopy with Lenslets
IFS-M	Integral Field Spectroscopy with Mirrors
IFS-F	Integral Field Spectroscopy with Fibers
CTIS	Computed Tomography Imaging Spectrometry
CASSI	Coded Aperture Snapshot Spectral Imaging
IRIS	Image-replication Imaging Spectrometer
SHIFT	Snapshot Hyperspectral Imaging Fourier Transform Spectrometer
FA	Fluorescein Angiography
NNMF	Non-negative matrix factorization
ALS	Alternating-least squares

Chapter 1

Introduction

1.1. Objectives and Specific aims

The objective of the work presented here is to (1) enhance the capabilities of snapshot hyperspectral imagers by adding tunability, (2) improve hyperspectral techniques for the oximetry of retinal vessels, and (3) create novel hyperspectral oximetry algorithms for fundus tissue.

Specific Aim 1: Design and build a tunable snapshot hyperspectral imager. This aim includes the construction of snapshot hyperspectral imager capable of controlling its spectral resolution in one integrated form. The impact of such a system will enable snapshot hyperspectral imaging to overcome datacube size restrictions due to detector array size limitations and to improve the data collection for

unexplored imaging scenarios. This prototype system will give vital preliminary information before installation onto a fundus camera.

Specific Aim 2: Acquire hyperspectral images of the fundus and develop algorithms for oximetry of retinal vessels using the IMS snapshot imager. We will demonstrate that oximetry is possible for a variety of disease states in the human eye by looking at the reflectance spectrum from vessels in the eye for different patients with different retinal diseases.

Specific aim 3: Develop protocols and new algorithms for hyperspectral analysis of fundus tissue. For this aim, we will use clinical data and hyperspectral analysis to develop new algorithms to perform oximetry for regions of the eye with unresolvable vasculature. The impact of these techniques will enable clinicians to co-locate oxyhemoglobin quantities within the eye, an improvement over existing retinal oximetry techniques.

1.2. Overview

In the succeeding chapters, a novel snapshot spectral imaging device capable of tunability, called LATIS (Lenslet Array Tunable Imaging Spectrometer), will be discussed and conveyed in terms of its design, operating principle, and advantages in biological imaging. Further, a discussion of snapshot spectral imagers and their use in retinal oximetry imaging will occur. This includes the development of algorithms using the high spectral sampling capabilities of a hyperspectral snapshot imager known as the Image Mapping Spectrometer (IMS) to enable the detection of oxygen

3

saturation in the retina and the retinal vessels. The general purpose of this thesis is to improve modern retinal oximetry methods using hyperspectral measurements and to prototype the development of a new snapshot spectral imager capable of integrating into a fundus camera. This system is advantageous over snapshot systems such as the IMS because it will be on-axis, improving its form factor over the IMS. Additionally, spectral resolution control will give greater insight into understanding the optimal spectral resolution for oximetry of the retina. Understanding the minimum required spectral content for a particular application such as oximetry, allows the improvement for non-tunable, dedicated HSI systems. The organization of the dissertation is as follows

Chapter 1 details an overview for the entire thesis while presenting specific aims.

Chapter 2 provides background information on the physiology of the human eye, the clinical significance of retinal oximetry, and snapshot hyperspectral imagers.

Chapter 3 presents the design and construction of LATIS along with its validation tests on a fluorescence microscope.

Chapter 4 presents clinical data acquiring from four diseased eyes using the IMS. It further explores the development of oximetry algorithms for oxygen saturation measurement in resolvable retinal vessels. The IMS acquires preliminary data of the eye, but future work is being planned to replace this system with LATIS.

4

Chapter 5 discusses the development of a new technique for oximetry of bulk retinal tissue with no resolvable retinal vessels. The results include a comparison between normal and diseased eyes to validate the sensitivity of the new technique to oxygen.

Chapter 6 provides a discussion of the work as a whole, enumerating the benefits of the present work and outlining the future work being planned.

Chapter 2

Background

2.1. Motivation and Significance

A restricted amount of oxygen delivered to the retina harms retinal function and processes. This eventually progresses to vision dysfunction and blindness. In fundus photography, the reflected light from the fundus captured with an imaging detector contains spectral information about the state and composition of retinal tissue. The absorption of light by specific chromophores modulates the spectrum of the initial illumination source. The shape of this reflectance spectrum offers a means to assess the quantity of individual chromophores such as hemoglobin in the eye. Hyperspectral imagers are capable of acquiring all spatial and spectral information of a given scene (x,y,λ) . A possible way to monitor the effectiveness of a treatment is to monitor the oxygen saturation of hemoglobin using these spectrometers. Oximetry of

the eye has a long history [Hickman 1959], and the oxygenation level in vessels has been correlated with disease progression [Hardarson 2013]. Snapshot imaging can remove motion artifacts of a moving eye [Johnson 2007]. Post-acquisition image registration is required for time-scanned hyperspectral images of the eye [Mordant 2011] due to eye saccades. Hyperspectral snapshot imaging does not require any image processing to remove eye movements, giving the technology a unique advantage over existing technologies. However, due to the limited chip size of both scientific grade detectors and low cost detectors, there is generally a compromise between the amount of spectral and spatial information that can be acquired in a non-scanning hyperspectral imager. The integration of tunability, which is the ability to dynamically tune the pixel sampling of the detector to either spectral or spatial values, allows a single system to meet a broad set of imaging demands. Additionally, this ability enables these exploratory tunable spectral imagers to ascertain the minimal spectral and spatial content for new imaging scenarios such as hyperspectral fundus imaging.

2.2. The Physiology of the Human Eye

The human eye is supplied with oxygenated blood via the ophthalmic artery (Figure 2-1). From this artery, the central retinal artery, the short and long posterior ciliary arteries, and the anterior ciliary arteries branch off. The iris and ciliary body are supplied by the anterior ciliary arteries and the long posterior ciliary artery. The retina is supplied by the central retinal artery and the short posterior ciliary arteries. After piercing the sclera, the central retinal artery branches and supplies the inner

retina. About two-thirds of the retina are supplied by the central retinal artery. The central retinal artery after exiting from the optic nerve divides into the superior and inferior papillary arteries. Retinal venules and veins merge to form the central retinal vein, which exits the eye and merges with the superior and inferior ophthalmic veins [Regatieri 2014]. In pig models, the retinal venous saturation was found to be about 55%, meaning the arterio-venous difference of retinal vessels is about 30% [Tornquist 1979]. The short ciliary artery pierces the sclera of the eye and supplies the choroid with oxygen.

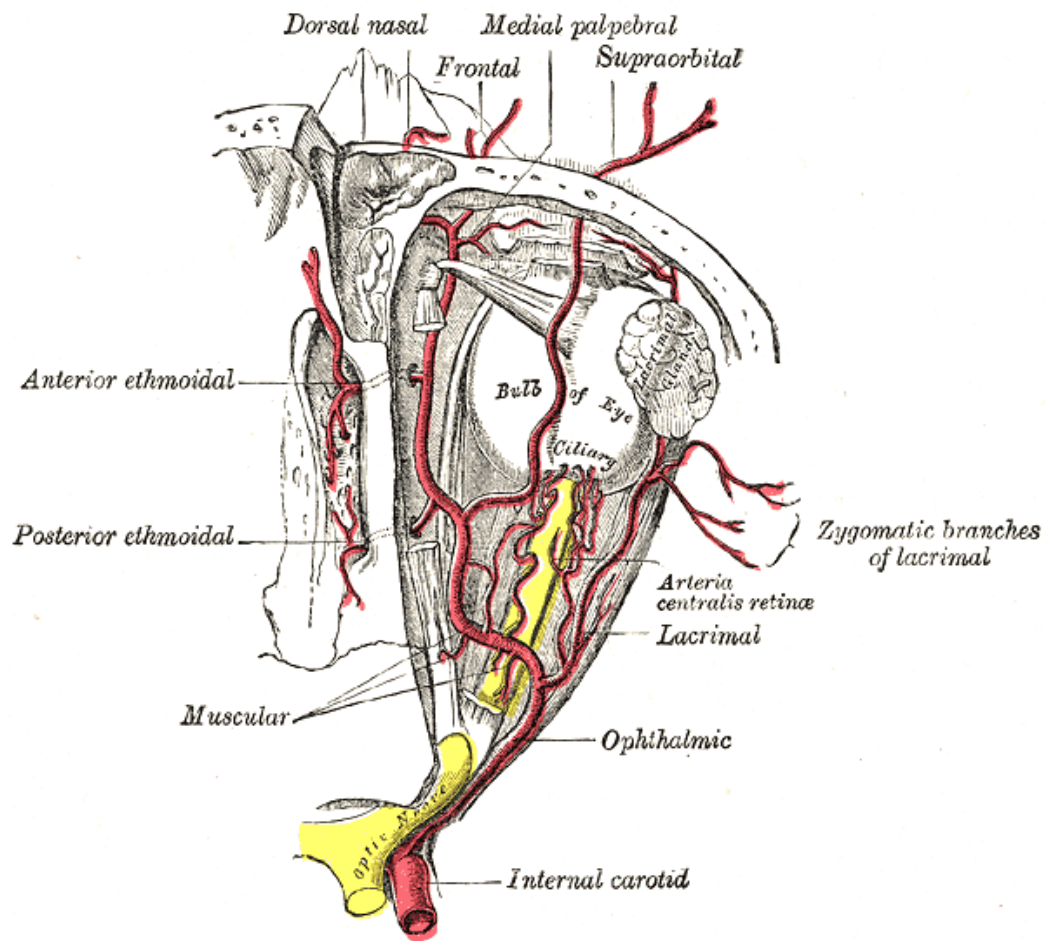


Figure 2-1. Branches of the ophthalmic artery

[Gray 1918]

The retina is composed of several layers, consisting of a neural layer, which possesses photoreceptors, the retinal pigmented epithelium (RPE), the Bruch membrane and a choroidal vascular network [Ambati 2013]. On the basal side of the choroid, lies the reflective sclera.

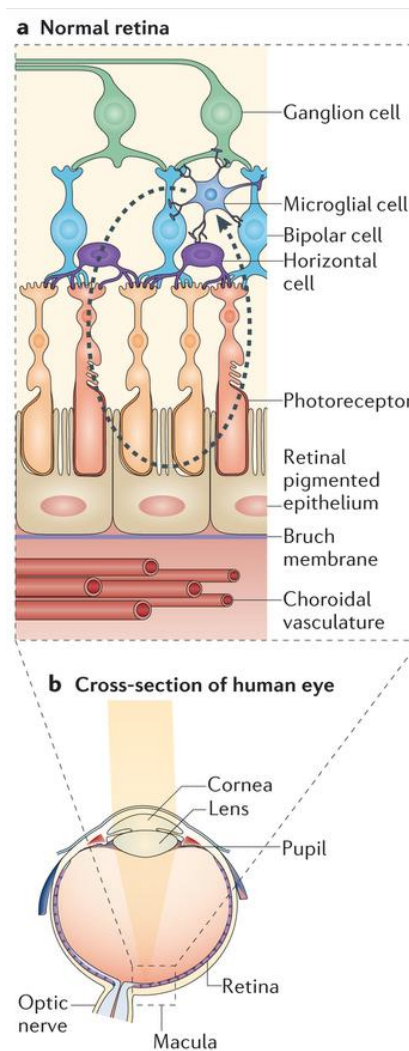


Figure 2-2. Cross-section of the retina
[Ambati 2013]

The choroid is the most vascular portion of the eye by weight. Proper blood flow and oxygenation through choroid maintains the retinal pigment epithelium and photoreceptors. Its other functions include light absorption, heat dissipation (thermoregulation), modulation of intraocular pressure. The choroid is organized into five layers: Bruch's Membrane, Choriocapillaris (Layer of capillaries), Sattler's Layer (Layer of medium diameter blood vessels), Haller's Layer (Layer of large diameter blood vessels), Suprachoroidea (transitional zone between choroid and sclera). The blood-retinal barrier (BRB) controls the exchange of metabolites and waste products between the vascular lumen and the neural retina. The RPE helps regulate this exchange as well with tight junctions and adherents junctions [Marmor 2005]. A breakdown of the BRB leads to leakage of blood components into the neural retina. The choroid has one of the highest rates of bloodflow in the body, several times greater than the bloodflow in the retina. Blood flow in the Choroid decreases with advancing age and due to different diseases AMD, Glaucoma, proliferative/non-proliferative diabetic retinopathy [Regatieri 2014]. Oxygen saturation difference between choroidal arteries and veins in a cat model has reported to be very low at around 3% [Alm 1970].

2.3. Age-related Macular Degeneration (AMD)

A potential far-reaching goal of this work is to apply the techniques developed here for the monitoring of the disease progression of AMD and its treatment. Globally, AMD is the third leading cause of blindness in the world and the leading of cause of blindness in the developing world [Resnikoff 2002]. In the U.S., The overall presence

10

of neovascular AMD or geographic atrophy in people aged 40 and over is 1.57%, placing 1.75 million Americans with AMD based on U.S. census information in 2000 [Friedman 2004]. This prevalence only increases with age. AMD becomes quite common after 75 years of age. The total number of cases of AMD to increase to 2.95 million in 2020 [Friedman2004].

AMD is marked by the degradation of photoreceptors, RPE, and the choriocapillaris in the macula, which results in vision in the center of the visual field. The disease has two different forms: wet and dry. The dry form accounts for most cases of AMD and is non-neovascular. The wet form accounts for most cases of visual impairment in patients with AMD, and it is marked by neovascularization in the macula. Vision loss can occur in dry forms of AMD due to geographic atrophy [Nunes 2013]. The progression of the disease starts as lipids deposited in Bruch's membrane with a possible reason being the RPE unable to handle cellular debris. These deposits eventually progress into drusen, which become the earliest visual sign of AMD. Hard drusen, which are small, yellow-white spots are less concerning than soft drusen, which are large, amorphous and carry an increased risk of vision impairment. A contributing factor to the development of AMD is also due to abnormalities in Bruch's membrane, which impedes the flow of fluid and nutrients between the choroid and retina. Neovascularization from the choriocapillaris can pierce the RPE and Bruch's membrane and impede vision in the macula. The disease can also lead to the detachment of the RPE through various mechanisms, including serous fluid buildup, fibrovascular tissue, or hemorrhaging.

Work has been done to estimate the mean oxygen saturation in retinal arteries and veins. While oxygen saturation in the arteries of patients with geographic atrophy AMD remains similar to the oxygen saturation in the arteries of non-diseased patients, geographic atrophy AMD patients have significantly higher oxygen saturation values in their veins compared to normal patients [Pollreisz 2014]. Oximetry studies suggest that oxygen metabolism is altered with exudative AMD [Geirsdottir 2014]. Retinal veins have higher oxygen saturation values compared to normal patients. Despite this, the role of reduced oxygen delivery to the macula is not well understood in the context of AMD, requiring more powerful tools to understand this mechanism.

2.4. Spectrometers

The purpose of a spectrometer is to measure the intensity of light at different regions in the electromagnetic spectrum. The independent variable in the measurement is wavelength. The dependent variable is the light's intensity at that wavelength measured by the instrument. Wavelength separation for the purpose of measurement is achieved by including a dispersive element in the system such as a prism or a grating. By using a grating or prism, light from different regions of the electromagnetic spectrum can be spatially separated. The simplest design of the spectrometer consists of light entering a pinhole or slit. This light is collimated by optics and sent through a prism. Different wavelengths refract at different angles through the prism. These refracted wavelengths are focused onto a detector, creating an image of a dispersed pinhole or slit.

2.5. Hyperspectral Imaging (HSI)

Hyperspectral imaging (HSI) is the collection of a spectrum for each pixel that images a scene. HSI has been widely used in the biomedical sciences [Lu 2014]. For example, spectroscopy in the field of Biology has seen increasing use due to the ability to unmix or delineate between different manufactured fluorophores, biological fluorophores, or autofluorescence in microscopy samples [Lerner 2006]. There are four general categories for the techniques used to acquire hyperspectral data cubes:

Point Scanning (“Whiskbroom spectrometer”): A scene is imaged onto a point aperture. The point image is dispersed onto a 1-D detector array. Each point image is equivalent to a single point (x, y) in the HSI datacube. The spectral information is collected via the 1-D array. To acquire the entire datacube, the point aperture or the scene being imaged needs to be scanned in both x and y directions

Line Scanning (“Pushbroom Spectrometer”): This technique is similar to the point scanning except the point aperture is a slit aperture. The slit image is dispersed onto a 2-D array, and each image is equivalent to a single column or row in the HSI datacube. As with the point scanning, the slit or the scene needs to be scanned to construct the entire datacube; however, only one spatial direction (x or y) needs to be scanned.

Wavelength Scanning: The spectral information is scanned and collected over time. Typically, both spatial directions (x and y) are collected at using a 2-D

detector array and a filter that limits the bandwidth of the spectrum. By changing the filter, different spectral scenes can be acquired

No Scanning (“Snapshot Spectrometer”): This technique collects the entire 3-D datacube (x, y, λ) on a 2-D detector array in a single integration time. There many methods of accomplishing this. A common method is to spatially separate regions of a scene on a detector, giving room for dispersion. This can be done with arrays of fibers, lenslets, or mirrors.

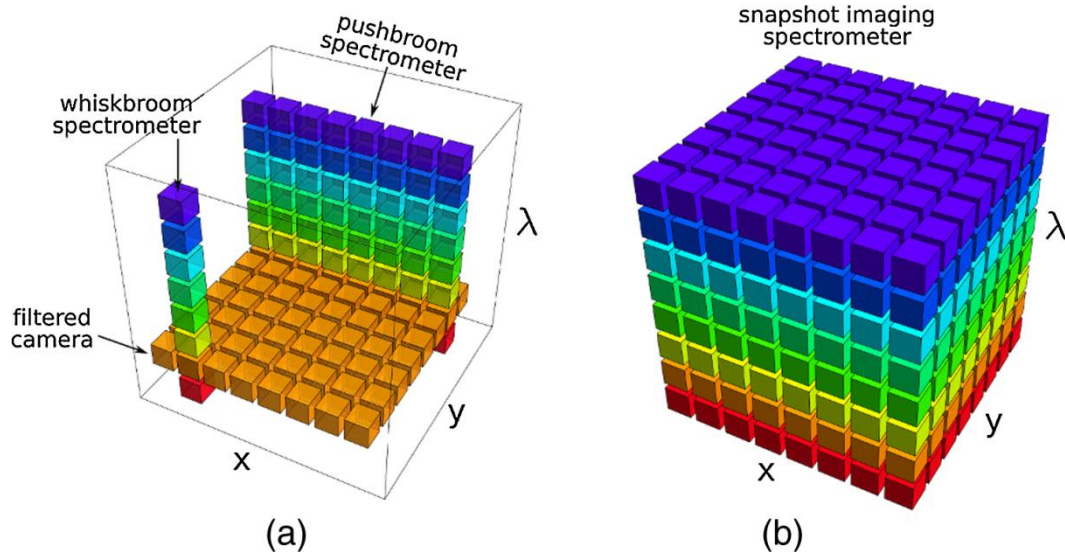


Figure 2-3. Conceptual representation of the 4 data acquisition methods for imaging spectrometers [Hagen 2013]

2.6. Snapshot Hyperspectral Imaging (sHSI)

Snapshot HSI can be achieved with a variety of different methods. Common approaches in astronomy are integral field spectroscopy (IFS) techniques. These techniques break the image on the detector into regions. Between these regions is

blank space, which is then used for spectral information by dispersing the fragmented image regions on the detector. Commonly employed methods for breaking apart images are mirror arrays (IFS-M), lenslet arrays (IFS-L), and fiber bundles (IFS-F). Other snapshot techniques include Computed Tomography Imaging Spectrometry (CTIS) [Ford 2001], Image-replication Imaging Spectrometer (IRIS) [Gorman 2010], Coded Aperture Snapshot Spectral Imaging (CASSI) [Wagadarikar 2009], Snapshot Hyperspectral Imaging Fourier Transform Spectrometer (SHIFT) [Kudenov 2012], and Image Mapping Spectrometer (IMS) [Gao 2010]. Snapshot HSI have been summarized and compared [Hagen 2013].

Also elucidated in prior work is the advantage of snapshot HSI [Hagen 2012] called snapshot advantage, which states that HSI light collection efficiency is proportional to the size of the datacube seen at one integration time of the detector. For a point scanning detector under geometric considerations, light is only collected for a single dimension (N_λ) for a datacube (N_x, N_y, N_λ) in one exposure time; thus, the overall light collection efficiency is the inverse of the number elements that are left in datacube that have not been acquired. This is $1/(N_x, N_y)$ for point scanning. For line scanning, this factor is improved since two dimensions are acquired (N_x, N_λ) equaling a light collection efficiency of $1/N_y$. For wavelength scanning, this efficiency is $1/N_\lambda$. In snapshot systems, the light collection efficiency is one since all dimensions are acquired at once, this advantage stems for the fact that all datapoints in the hyperspectral datacube receive the same exposure time as the datacube as a whole.

Snapshot techniques that do not have the improvement in light collection efficiency are techniques with a division of aperture. Such techniques can use multi-apertures in a system, which limit light collection proportionally to the number of filters or apertures used in the system. Full throughput snapshot techniques are in theory 100% in the light collection efficiency. They do not require filters or a division of aperture. These techniques include IFS, CTIS, IRIS, CASSI, SHIFT, and IMS. Although the techniques are classified as full throughput, they are not always 100% efficient in practice; light loss can occur due to deficiencies in optics. These systems are typically more computationally and optically complex, which can be considered a trade-off when compared to the simplicity of scanning techniques

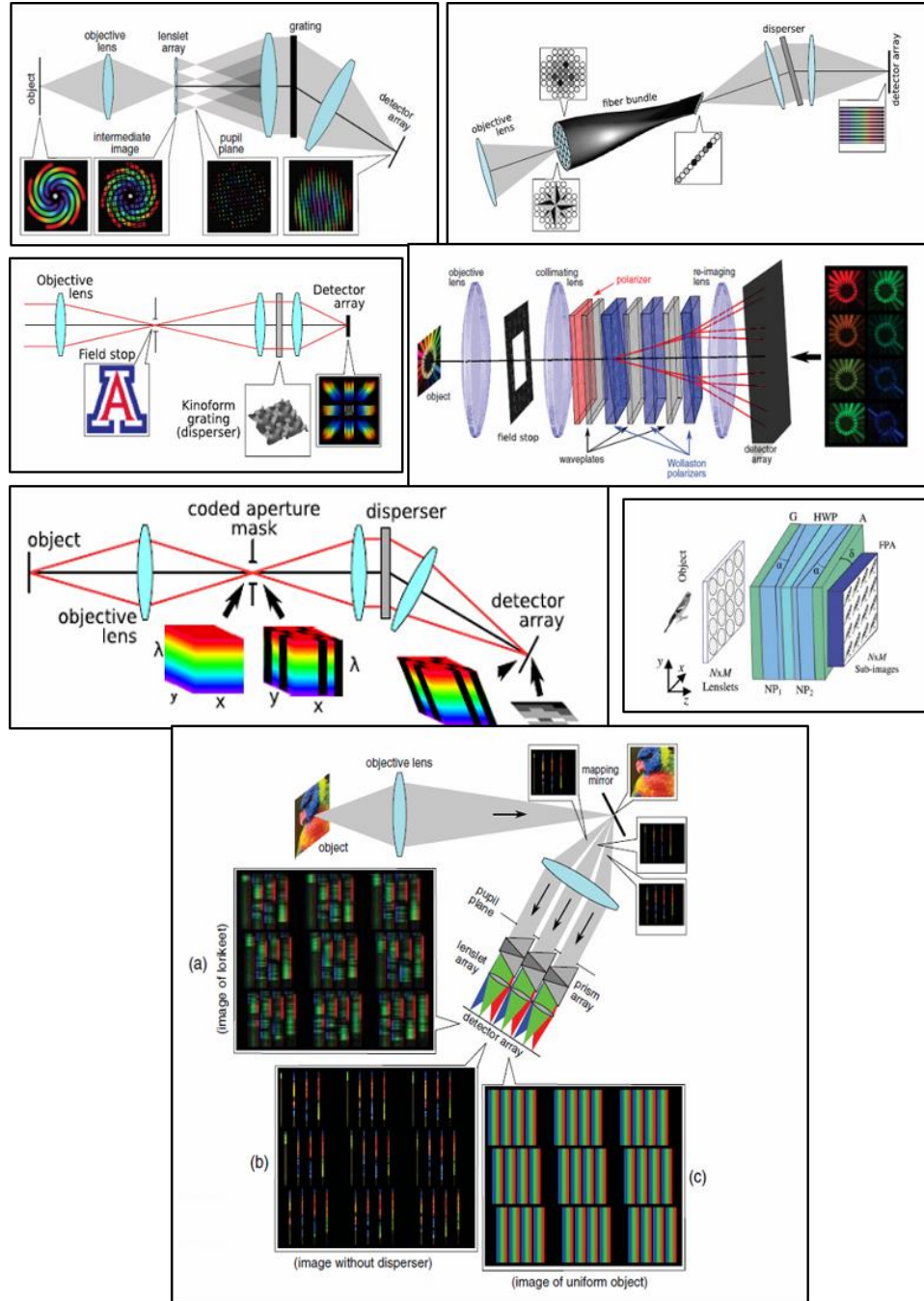


Figure 2-4. System architectures for snapshot HSI.

(a) IFS-F (b) IFS-L (c) CTIS (d) IRIS (e) CASSI (f) SHIFT (g) IMS, which is similar in principle to IFS-M [Hagen 2013]

Chapter 3

Construction of a Tunable Snapshot Imaging Spectrometer*

*The contents of this chapter have been published in the following journal article: J.G. Dwight and T.S. Tkaczyk, "Lenslet array tunable snapshot imaging spectrometer (LATIS) for hyperspectral fluorescence microscopy," *Biomed. Opt. Express* 8(3), 1950–1964 (2017).

This chapter presents a novel snapshot spectral imager capable of dynamically trading spatial content for spectral content in one integrated system to offset datacube limits set by present-day detectors and optics. By enabling “tunability”, a single snapshot imager can acquire a controllable amount of spectral and spatial information as dictated by the needs of the imaging scenario. The theory behind its operation and the construction of a working prototype are detailed.

3.1. Introduction

Fluorescence microscopy has become widespread in its use in biology over the last few decades [Lichtman 2005]. Thousands of fluorophores have been developed to label selectively biological samples and to identify cellular level features. Fluorescence emission at different wavelengths allows features of interest to be separated spectrally. Applications include FISH [Tkachuk 1991], FRET [Pietraszewska-Bogiel 2011], and live-cell imaging [Chudakov 2005]. Fluorescence imaging is complicated by the spectral proximity of fluorophores [Schultz 2001] and the use of many fluorophores in a single scene [Zimmerman 2003, 2005]. Hyperspectral Fluorescence Microscopy (HFM) acquires many spectral bands of a scene to create hyperspectral data cubes (x,y,λ) , also called lambda stacks, and can provide high spectral resolution for demanding fluorescence imaging applications [Sutherland 2007, Vermaas 2008]. Spectral data enables the ability to linearly unmix many different co-localized fluorophores with closely overlapping emission and absorption profiles to determine their abundance at a given point in the scene [Zimmerman 2005].

HFM data cubes can be acquired in various ways. Point-scanning techniques collect spectral data (λ) at discrete spatial positions (x,y) with the most common technique being laser point-scanning confocal microscopy [Sinclair 2006, Frank 2007]. The 2-D scan required by single-beam laser confocal microscopy typically moves at one μ s per pixel, which limits typical acquisitions to .5 to 2 seconds per

lambda stack [Toomre]. Dynamic scenes requiring high temporal resolution can be limited by the speed of point-scanning. Another drawback with point-scanning is the short pixel dwell time, which limits the number of photons acquired per pixel and reduces the signal-to-noise ratio (SNR) of the system. Line-scanning techniques can partially offset these problems by instead collecting at once a slice of the datacube (x,λ) requiring scanning in only one spatial direction (y) [Cutler 2013]. Wavelength-scanning systems acquire spectral bands (λ) sequentially by collecting wide-field images (x,y) with filters. Variable filters such as acousto-optic filters (AOTF) [Kasili 2006] and liquid crystal tunable filters (LCTF) [Woltman 2007] possess no moving parts and provide fast wavelength acquisition times but suffer from poor transmission efficiencies.

With recent advances in CCD technology, a class of spectrometers called snapshot hyperspectral imaging has emerged. The term “snapshot” refers to the spectrometer’s ability to record a lambda stack in a single exposure of the camera. They were first employed in astronomy [Sparks 2002] and remote sensing [Vane 1993]. These spectral imagers can be designed to be advantageous over existing scanning spectrometers due to longer pixel dwell times, permitting their use in dim applications, and higher speeds, which eliminate motion artifacts for dynamic scenes [Hagen 2013]. The advantages of these spectral imagers have seen their increased use in microscopy applications over the last few years [Elliot 2012, Elliot 2013] and in vivo tissue imaging [Johnson 2007, Kester 2011, Gao 2012, Bedard 2013, Khoobehi 2015]. Each pixel’s exposure time to the collected light is the same as the time used

to acquire the datacube, which increases irradiance per pixel in comparison to scanning techniques with the same datacube acquisition time or frame rate. Hence, situations with low signal such as fluorescence emission collection in microscopy benefit from snapshot hyperspectral imaging. The greater irradiance per pixel collected can reduce the need for high excitation energy, thus reducing the amount of photobleaching of fluorophores. Integral Field Spectroscopy (IFS) is a subset of techniques in snapshot hyperspectral imaging [Allington-Smith 1998]. IFS uses either optical fibers, mirror arrays, or lenslet arrays to break apart an image, leaving void pixel space dedicated to spectral dispersion on the detector. The concept of using lenslet arrays as an IFS technique was first illustrated in the 1980s with a series of publications [Courtes 1980, 1982, 1988]. IFS with lenslet arrays continues to be used in the field of astronomy [Bacon 1995a, Bacon 2001, Lee 2001] and remote sensing [Bodkin 2009, 2012]. However, this technique has seen limited use in microscopy. IFS with mirrors for HFM has been demonstrated with a camera called the Image Mapping Spectrometer (IMS) [Gao 2009, 2010]. The IMS has acquired video rate speeds [Bedard 2012] with high light throughput, long pixel dwell time, and low computational costs.

In this paper, we present a novel adaptive snapshot spectral imager incorporating lenslet arrays for HFM called the Lenslet Array Tunable Snapshot Imaging Spectrometer (LATIS). We incorporate tunability, which is the ability to control the spectral resolution. The relatively straightforward geometry of a lenslet array system only requires minor changes to the system's optics to incorporate this

feature. Tunability allows for the re-arrangement of spatio-spectral pixel mapping on the detector. A fixed pixel region can record either more spectral pixel values (higher spectral resolution) at the cost of spatial pixel values (less field-of-view) and vice versa. Gaining spectral resolution results in the ability to resolve spectrally similar fluorophores. On the other hand, the reduction of spectral resolution results in fewer pixels mapping the same spectral range, which results in higher irradiance recorded per light sensing element and effectively increases the signal-to-noise (SNR) per photodetector. The LATIS principle can fit a wide range of HFM datacube requirements in one integrated system. Other systems in the past have provided tunability by the replacement of the dispersive element [Larson 2006] at the cost of spectral range. To provide tunability with LATIS, we have integrated variable focal length lenses in place of fixed focal length lenses. The use of variable focal length lenses to implement tunability has been mentioned in prior art, but was never expanded upon in terms of its operating principle, design, implementation, and advantages [Bodkin 2006]. With LATIS, the user can control the spectral resolution and datacube dimensions by changing the focal length of the varifocal optics and the rotation of the lenslet array while keeping the same dispersive element and spectral range. Our proof-of-concept tunable instrument uses off-the-shelf optics and provides two datacube settings as a demonstration: 80x80x22 and 88x88x46 (only limited in size due to the performance of consumer grade off-the-shelf optics). In addition, we built a fixed focal length (“static”) system, optimized for larger data cubes but not capable of tunability. Large field-of-view (FOV) images of bovine

pulmonary artery endothelial (BPAE) cells and sectioned mouse tissue were acquired with this system. The system was configured for two different spectral ranges for each sample, 200x200x27 (515 to 635 nm) for BPAE cells and 200x200x17 (570 to 670 nm) for mouse tissue. To the best of our knowledge, this is the first implementation of lenslet arrays as an IFS for biological samples and the first snapshot spectral imager capable of tuning spectral resolution.

3.2. General Principle

3.2.1. Integral Field Spectroscopy with Lenslet Arrays

IFS with lenslet arrays, though proposed in the early 1980s, was not realized until its first installation on the Canada-France-Hawaii Telescope (CFHT) in 1987 [Bacon 1995b]. The operating principle for lenslet arrays as an IFS for microscopy is the same as its operating principle for astronomy. To implement lenslet array IFS with microscopy, the microscope's side port image is magnified and relayed by imaging optics onto a lenslet array as shown in Figure 3-1. The lenslet array samples the enlarged image. The point spread function (PSF) of the imaging subsystem in the image space must be preserved by subsequent optical sub-systems in accordance with the Nyquist sampling theorem in order for the system to maintain diffraction-limited performance. At the focal plane of each lenslet, an image of the exit sub-pupil will form, comprising of all the light from the image that fell onto the spatial extent of the lenslet's diameter. The lenslet takes a slower beam (high f-number) from the

image and focuses it into a faster beam (low f-number), producing void space between adjacent sub-pupil images. The spatial location of each sub-pupil image corresponds to the spatial location in the image sampled by the lenslet array. The void space now allows for dispersion of each sub-pupil image without spatial and spectral overlap. The first lens from the re-imaging optics sub-system collimates the sub-pupil images. The light then passes through the dispersive element followed by the focusing lens, which forms images of dispersed sub-pupils on the 2-D photodetector. Each pixel sampling the sub-pupil image will correspond to a unique (x,y) location in the image plane with pixels along the long axis of an elongated sub-pupil image carrying information about the spectral signature of the scene (λ) . The combination of both allows us to build a unique correspondence between object points (X,Y) and the position in the hyperspectral datacube (x,y,λ) . To prevent spectral overlap, the separation between adjacent dispersed sub-pupils on the detector must be ≥ 1 pixel. To efficiently utilize detector space, the lenslets can be rotated to more compactly fit dispersed sub-pupil images. Possible rotations are the result of both the pixel spacing between adjacent dispersed sub-pupil images and the lenslet array geometry. The two common lenslet array geometries, hexagonal and rectangular, have different possible rotations due to their inherent lenslet arrangements. In general, larger rotations more compactly fit dispersed sub-pupil images, giving more room for spectral dispersion; but consequently, they require greater adjacent spectra pixel separation. Due to the correspondence between sub-pupil image position and the side

port image, reconstruction only requires a re-arrangement of pixel values into a lambda stack, which may be reduced to a simple 2-D lookup table.

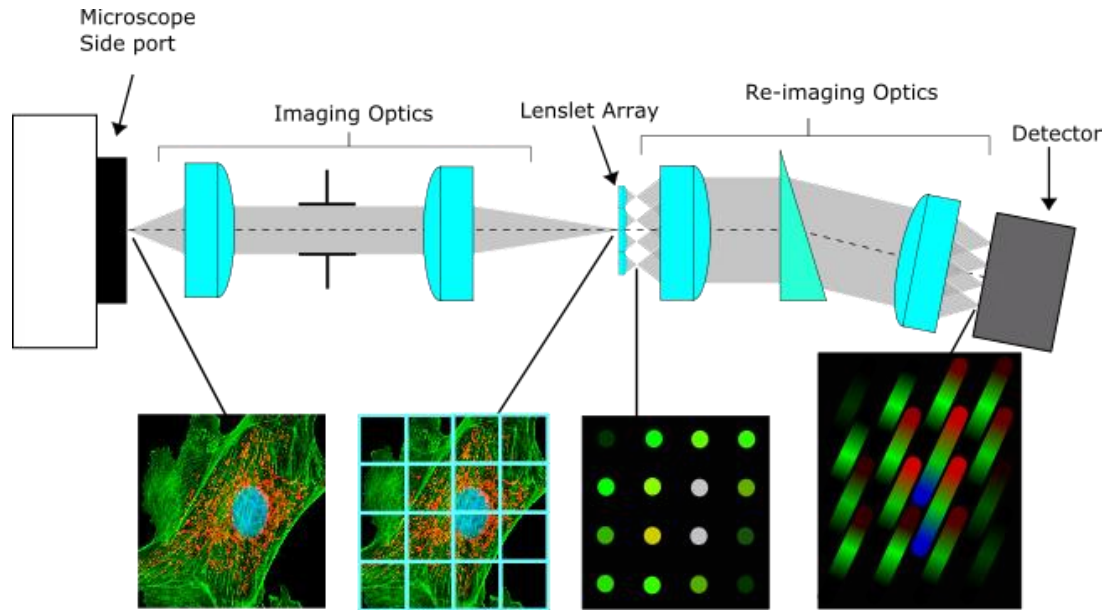


Figure 3-1. Lenslet array principle as an IFS for microscopy

Each sub-pupil image can be treated as an equivalent to an exit pinhole in a standard point spectrometer. The lengths and widths of sub-pupil images on image detector depend on the re-imaging optics system. The width is directly dependent on the system's magnification and the length is bound by the spectral dispersion of the prism element. The spectral range of the instrument is limited physically by the spectral transmission of the optical train and the spectral sensitivity of the detector. Since the sub-pupil rather than the field is imaged on the detector, the resolution of the microscope's image is independent of the spectral resolution on the detector. The

sub-pupil images given by the optical system on the imaging detector must be sampled in accordance with the Nyquist theorem in order to preserve the spatio-spectral content and avoid unwanted intensity beating and aliasing effects.

3.2.2. Tunability Principle of LATIS

With integrated tunability, LATIS is able to control its spectral resolution without an exchange of optical components. The re-imaging system in LATIS images sub-pupil images onto the detector and consists of a collimating lens with a focal length of f_{coll} , a prism, and a refocusing optic with a focal length of f_{focus} . Dispersion, denoted by $\frac{dx}{d\lambda}$, is a function of the angular dispersion of the dispersive element, $\frac{d\delta}{d\lambda}$, and f_{focus} and is equivalent in the following manner

$$\frac{dx}{d\lambda} = f_{focus} * \frac{d\delta}{d\lambda}$$

Equation 3-1. Linear Dispersion

The PSF width, w , is a function of the magnified image of the lenslet's sub-pupil image diameter, $pupil_{image}$, on the detector and is equivalent to

$$w = pupil_{image} * \frac{f_{focus}}{f_{coll}}$$

Equation 3-2. PSF width in Lenslet system

under the assumption of diffraction-limited imaging conditions between the collimating and refocusing optic. A demonstration of tunability is shown in Figure 3-2 based on these equations. In this example, the initial value for f_{coll} and f_{focus} is the value f , giving a magnification of 1, and the initial separation between adjacent spectra is 2 pixels due to the set pitch of this lenslet array. The physical distance is presented in terms of pixel size for this hypothetical detector. The lenslet pitch is 7.7 pixels. The width of the dispersed sub-pupils is 2 pixels and the length is 12 pixels. When f_{focus} is increased to $2.5f$, w and $\frac{dx}{d\lambda}$ increase by 2.5x as long as the aperture stop size remains constant. However, by additionally increasing f_{coll} to $1.5f$, the factor by which w scales is $1.6\bar{6}x$ instead of 2.5x, which results in increased spectral dispersion. This is seen as overlap between collinear dispersed sub-pupil images as seen in Figure 3-2. To remove this overlap, the lenslet array rotation, θ , is changed from 0° to 11° . The magnified image of the lenslets is overlaid onto the dispersed sub-pupils to illustrate rotation. Achievable rotation angles depend on lenslet array geometry with this particular example using a hexagonal arrangement. This new rotation is possible due to the increased adjacent spectra separation. After the focal length change, the adjacent spectra separation is 3.34 pixels. After the lenslet array rotation, the adjacent spectra separation is 1 pixel, preventing adjacent overlap between spectra. Note that as a consequence of increased magnification, spectral sampling improves for each sub-pupil at the cost of reduced FOV, resulting in a reduced count of sub-pupil images recorded by the image detector.

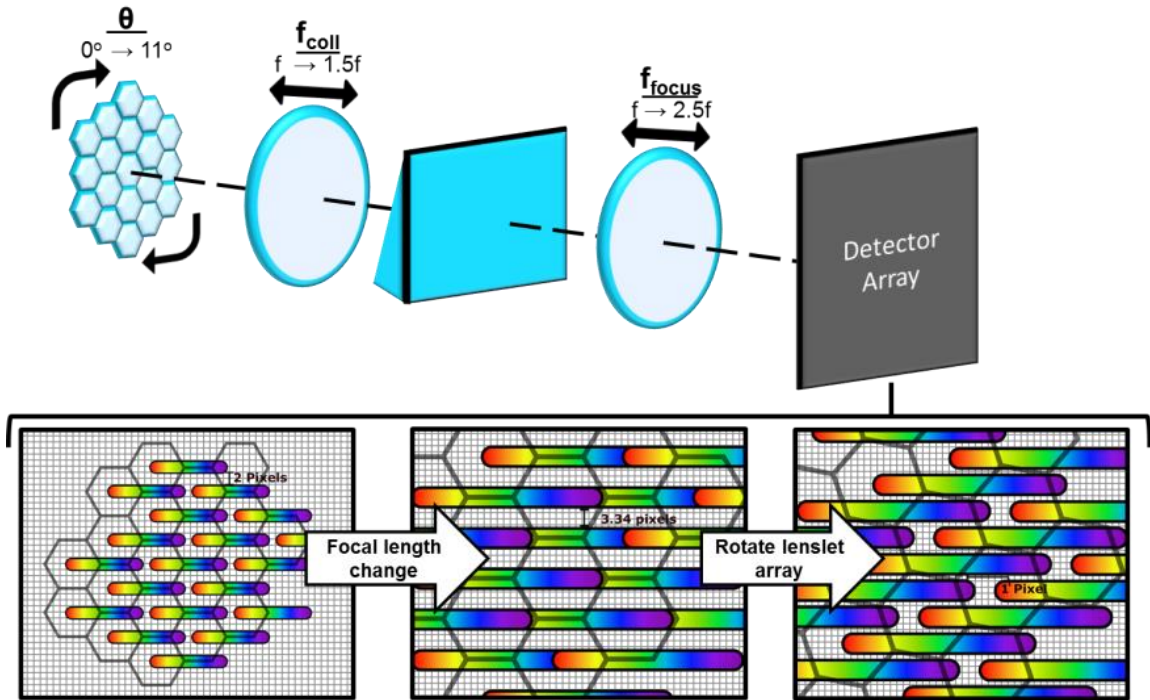


Figure 3-2. The tunability principle of LATIS

In this example, sub-pupil images from a hexagonal lenslet array are collimated and refocused onto the detector array. The lenslets are overlaid in grey on top of the dispersed sub-pupils to illustrate the rotation. Adjacent separation is 2 pixels between dispersed sub-pupil images. By changing f_{coll} from f to $1.5f$ and f_{focus} from f to $2.5f$, spectral dispersion increases causing overlap of collinear dispersed sub-pupil images. Adjacent spectra separation is now 3.34 pixels. Rotating the lenslet array by 11° fits spectra on the detector with no spectral overlap and an adjacent spectra separation of 1 pixel.

Varifocal lenses and lenslet array rotations can be adjusted further. Figure 3-3(a) presents a range of settings in a table based on eq. 1 and 2 to demonstrate the extent of spectral resolution improvement (smaller spectral PSF). Spectral PSF change in width is modeled in Figure 3-3(b) to conceptually present the spectral resolution improvement. Varifocal lenses have continuous focal length change; thus, LATIS is capable of achieving a multitude of tuning settings. Tuning settings are

arranged in an order of increasing spectral resolution in reference to tuning setting 1, which is provided in the first row of Figure 3-3(a). The lenslet array is assumed to be rotated between settings to accommodate increased spectral dispersion.

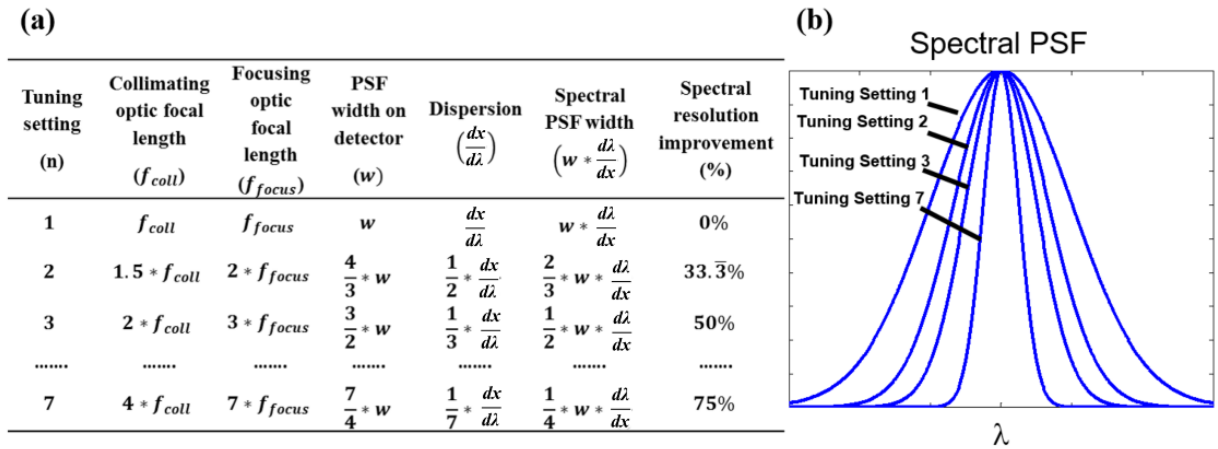


Figure 3-3. A range of tuning settings in an example LATIS system

Fig. (a). A table of 4 tuning settings based on eqs. 1 and 2 to demonstrate the effect of focal length change on spectral PSF width. Fig. (b). A plot of the spectral PSF at each tuning setting.

3.3. Instrument Description

LATIS is a universal imaging system that can be coupled to a wide array of imaging modalities such as microscopes, endoscopes, and fundus cameras. Our prototype has been coupled to the side port of a Zeiss AX10 inverted microscope to demonstrate HFM in the visible light range. It is presently configured for two tuning settings. A photograph of the prototype is shown in Figure 3-4(a), and the schematic is presented in Figure 3-4(b), displaying the configuration change between the two tuning settings. Changes between settings require no additional optics.

Tunability utilizes the built-in mechanics of the system. The intermediate image at the side port is re-imaged by the 5x telescope, which consists of an $f = 30$ mm achromatic doublet and an $f = 150$ mm achromatic doublet, onto the lenslet array. In the infinity space of the telescope, a spectral bandpass filter limits the wavelength range (485 nm to 660 nm) to prevent spectral overlap between sub-pupil images. The lenslet array (APH-P(GB)-P30-F0.0480(633), Flexible Optical B.V.) samples the re-imaged side port image. The array's dimensions act as a field stop. The lenslet array is a 17 mm x 17 mm array with transparent polymer lenslets on a glass substrate arranged hexagonally with a 0.03 mm pitch. This lenslet array was chosen for the high NA of each lenslet (0.3 NA at 633 nm) and the high density of lenslets (>1000 lenslets per 1 mm^2). High density gives better sampling of the image on the array, and a high NA gives a smaller sub-pupil image size, increasing void space between adjacent spots. As a trade-off, high NA demands higher performance optics that follow. The lenslet array is mounted in a rotation mount (Thorlabs LCRM2) using an acrylic mask cut to the dimensions of the array which acts as an adapter in Figure 3-5(a). This mount provides 360° of rotation around the optical axis. The lenslet array contains defective lenslets and imperfections and can be seen under a stereomicroscope (see Figure 3-5(b)). The lenslet array was imaged under a white light interferometer and displayed in Figure 3-5(c). The profiles are incomplete due to the steep curvature of the lenslets presented in Figure 3-5(d). In Figure 3-5(b), each sub-pupil image is collimated by the first varifocal lens (Olympus Zuiko ED 14-42mm $f/3.5-5.6$). The collimated sub-pupils are then dispersed by a 5° right angle fused silica prism, and

then refocused by a second varifocal lens (Olympus Zuiko ED 40-150mm, F/4.0-5.6). To adjust from the first tuning setting to the second, the varifocal lens' focal lengths are changed, and the lenslet array is rotated. The system is altered as follows: the focal length of the first varifocal lens is changed from 20 mm to 30 mm, the focal length of the second varifocal lens is changed from 50 mm to 100 mm, and the lenslet array is rotated to 11° . As a consequence of the varifocal lens focal length difference, the dispersed sub-pupil images on the detector become defocused due to the shifted axial position of the image plane, requiring a slight camera axial position shift via a translation stage.

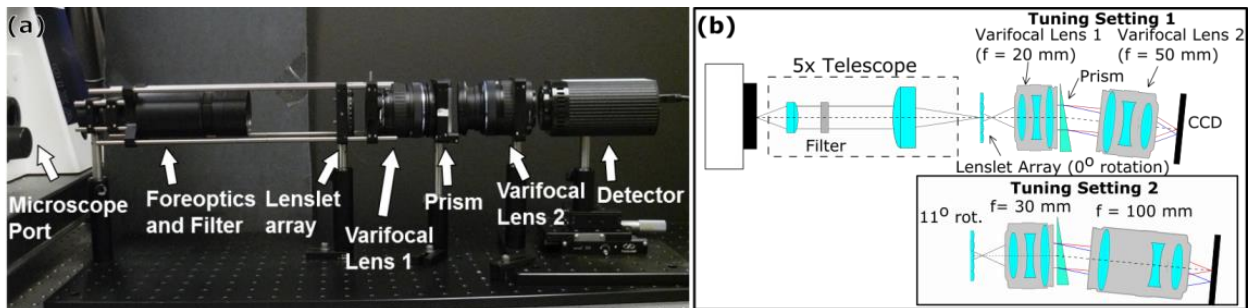


Figure 3-4. Illustrated schematic for LATIS.

Illustrated schematic for LATIS. Fig. (a). Shows a photograph of the system at tuning setting 1. Fig. (b). Shows the schematic of the system. The filter has a bandpass of 485-660 nm to prevent spectral overlap. Red rays represent the longest wavelength passed by the filter. Blue rays represent the shortest wavelength. Only one sub-pupil image is shown to simplify the schematic. The adjustment from tuning setting 1 to 2 is done by changing the focal length of varifocal lens 1 from 20 mm to 30 mm, the focal length of varifocal lens 2 from 50 mm to 100 mm, and the lenslet array rotation from 0° to 11° . The detector is translated axially via a translation stage to refocus dispersed sub-pupil images between tuning settings.

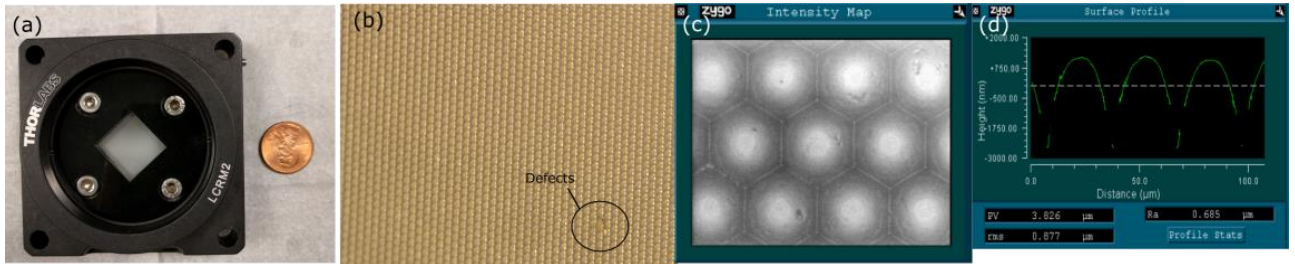


Figure 3-5. Lenslet array mount and characterization of the lenslet array surface
 Fig. (a). Photograph of the lenslet array in the rotation mount. Fig. (b). Photograph of the lenslet array through a stereomicroscope. Missing lenslets and defects can be seen and are easy to spot through the stereomicroscope. Fig. (c). Intensity map of lenslets taken with a white light interferometer. Individual lenslet dents and imperfections can be seen. Fig. (d). The surface profile acquired with the white light interferometer. Due to the lenslet curvature, the surface profile is incomplete for steep portions of the lenslets' surfaces.

Due to the FOV vignette limit using this off-the-shelf varifocal lens combination, only 80x80 spots can be imaged at setting 1 and only 88x88 spots can be imaged at setting 2. The camera is a 1040x1392 CCD array (Retiga EXi 1394 Fast). Since not all sub-pupil images formed by the array can be imaged as shown in Figure 3-6, the size of the camera array is sufficient for imaging all refocused sub-pupil images. The first setting gives a spectral sampling of 22 pixels, and the second setting increases that spectral sampling to 46 pixels. Since the magnification of the lenslet array sub-pupil image width changes by a factor of $1.3\bar{3}$ whereas the dispersion changes by a factor of 2, there is a theoretical spectral resolution improvement of $33.3\bar{3}\%$ (see imaging results).

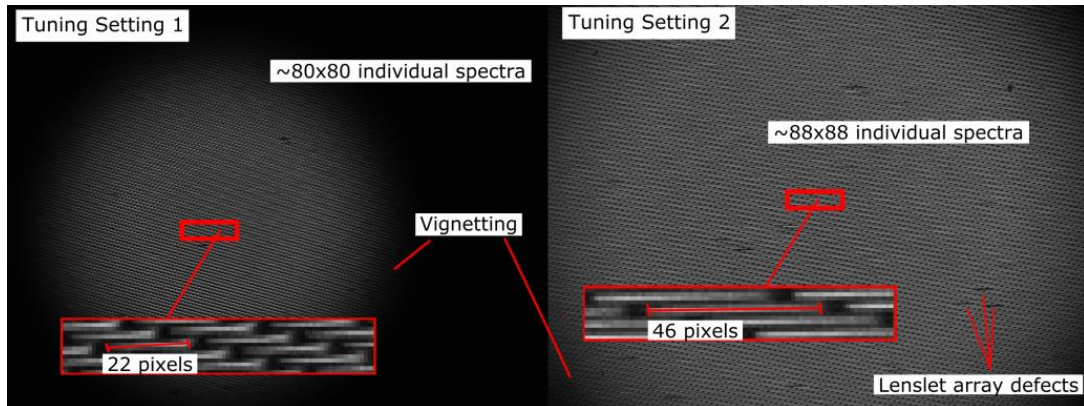


Figure 3-6. Raw unprocessed images of dispersed sub-pupil images acquired with the Retiga EXi. The system is illuminated with a halogen source from the Zeiss AX10. Datacubes for tuning setting 1 and 2 are $80 \times 80 \times 22$ and $88 \times 88 \times 46$, respectively. Lenslet array defects manifest as missing or obscured dispersed sub-pupil images and are marked with arrows on right hand image.

To demonstrate that larger data cubes are possible, we set up a fixed magnification system, which we will refer to as the static LATIS system. The collimating optic is a Nikon 1.4D 50 mm prime lens and the refocusing optic is a Canon EF 100-400 mm varifocal lens set at 250 mm (see Figure 3-7). This combination re-images sub-pupil images onto the detector with a 5x magnification and is necessary to prevent spectral overlap in this system. The number of sub-pupil images capable of being imaged on the detector is 200×200 . To reduce chromatic aberration, the manual aperture on the prime lens was set to F/5.6, sacrificing light throughput for improved chromatic performance. To accommodate the new FOV, the detector array is changed to a 16 MP full frame camera (Imperx IPX-16-M3-LMFB) to acquire all 200×200 spots on the detector. Captured images are binned on the detector by 2 pixels vertically to increase SNR in the system and reduce exposure times, so the actual raw image size was 1624×4872 (7.9 MP).

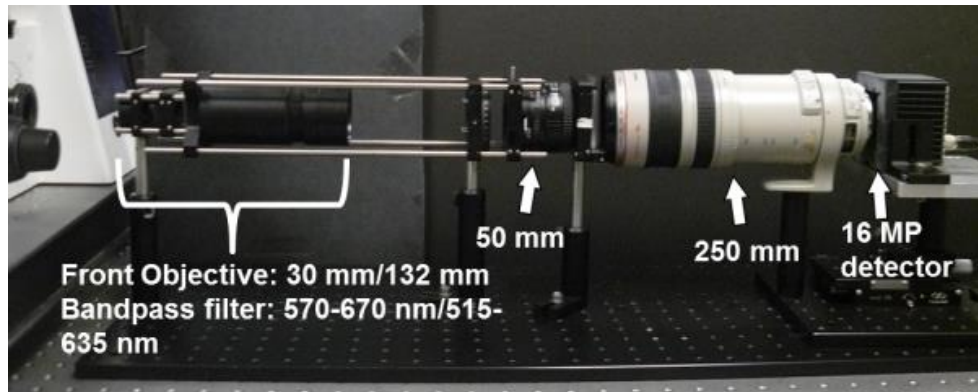


Figure 3-7. A photograph of the static LATIS system.

Changes to optical setup from the previous tunable system are indicated with white arrows. The front optics and the bandpass filter were changed between specimens imaged and are detailed further in the Imaging results section.

3.4. Imaging Results

3.4.1. Calibration and Reconstruction

Due to the uniform hexagonal arrangement of lenslet arrays, the spatial position of each spot on the detector is linearly related to the (x,y) position of the reconstructed datacube (x,y,λ) . Each spot is thus assigned a unique position in the datacube based upon its location on the detector.

To assign the pixels on the detector to a unique λ position, three flatfield images, images with no specimen or sample, were taken successively with three 1-nm bandpass filters in the illumination path of the AX10 microscope. Imaging with the filters, centered at 514, 589, and 633 nm, gives the spectral response of the LATIS system at those wavelengths. Figure 3-8(a) shows a superposition of the three filter

images in a sub-pupil image along the direction of dispersion. Blue, green, and black markers signify the centroids for 514, 589, and 633 nm and are used to interpolate the centroid positions for additional wavelengths as shown in Figure 3-8(b). Reconstruction of unprocessed images was performed in MATLAB®. Interpolated positions are represented by red markers and spaced every 3 nm along the detector-sampled spectrum. Red marker density increases towards the longer wavelengths due to the prism's nonlinear dispersion. Wavelength positions and values are interpolated to a sub-pixel position to provide smooth and continuous reconstructed images using the `interp2()` function in MATLAB®. Images for each spectral channel are then reconstructed with the known wavelengths and positions. The result of the interpolation creates images and spectra that are free of artifacts caused by missing lenslets and defects. Examples of reconstructed resolution targets for the tunable LATIS and the static LATIS are shown in Figure 3-8(c) and Figure 3-8(d).

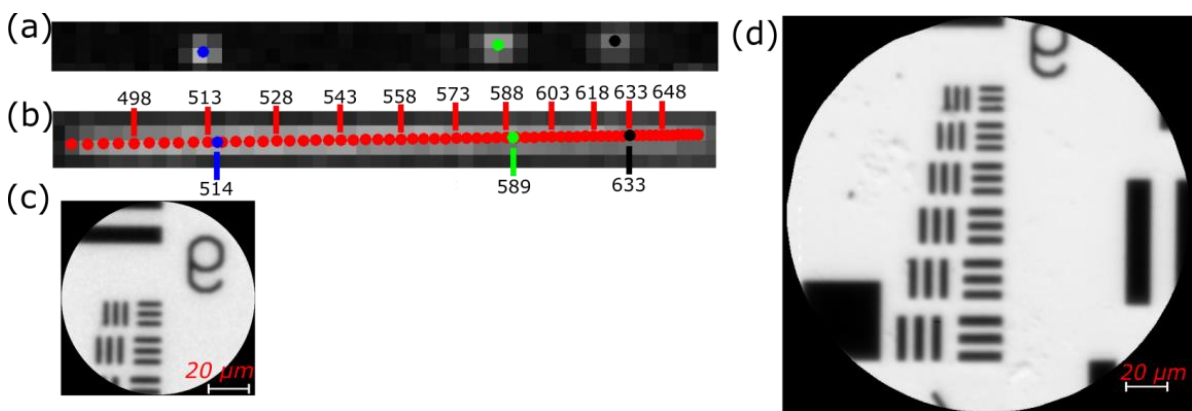


Figure 3-8. Reconstruction of images for LATIS.

Fig. (a). The spectral response of three narrow band filters with a 1-nm spectral bandpass. Each marker (blue, green, black) represents the centroid for each narrow band filter imaged. Fig. (b).

Using the calculated centroids, wavelength positions are interpolated (represented by red markers). Due to the prism's nonlinearity, pixel sampling of the spectrum is also nonlinear. Fig. (c). Reconstructed panchromatic image of a resolution target acquired with the tunable LATIS. Fig. (d). Reconstructed panchromatic image of a resolution target for the static LATIS. The FOV is larger due to the greater number of spatial samples (200x200 vs. 88x88).

3.4.2. Spectral Resolution measurements for LATIS

Spectral resolution is defined as the smallest resolvable spectral feature in a spectrometer. Datacubes for four flatfield images were acquired, each taken with a different 1-nm filter in the illumination path of the AX10. The center wavelengths for the filters were 514, 532, 589, and 633 nm. The width of the transmission curves of these filters measured with LATIS gives the spectral PSF at each wavelength since the transmission bandwidth is smaller than LATIS's spectral resolution. Datacubes were reconstructed using the calibration method outlined in section 4.1. The spectrum for each filter as recorded by LATIS was found by taking the mean pixel value over all spatial locations at each spectral channel. The results for both tuning settings are shown in Figure 3-9. Measurements of the full width half maximum (FWHM) are shown in Table 1. The FWHM changed between settings from 13.25 (± 1.82) to 8.90 (± 1.31) nm, 14.46 (± 1.90) to 9.55 (± 1.37) nm, 24.31 (± 4.16) to 15.22 (± 1.64) nm, and 38.62 (± 9.88) to 22.09 (± 3.03) nm for wavelengths 514, 532, 589, and 633 nm, respectively. The spectral FWHM at longer wavelengths is larger due to the non-linearity of the prism dispersion. Shorter wavelengths experience greater dispersion, which translates into a smaller spectral width as seen in Table 3-1.

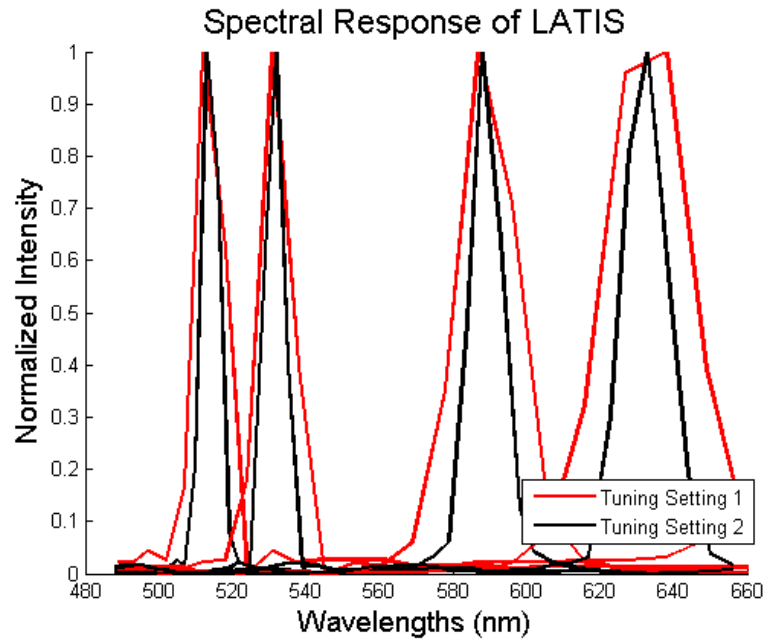


Figure 3-9. The mean spectral response of LATIS. The red lines represent the spectral response at tuning setting 1, and the black lines represent tuning setting 2.

Table 3-1. Spectral response of LATIS

Filter center wavelength (nm)	Tuning setting 1 (nm)	Tuning setting 2 (nm)	Improvement between settings (%)
514	13.25 ± 1.82	8.90 ± 1.31	32.83
532	14.46 ± 1.90	9.55 ± 1.37	33.96
589	24.31 ± 4.16	15.22 ± 1.64	37.39
633	38.62 ± 9.88	22.09 ± 3.03	42.80

3.4.3. Spectral Accuracy of LATIS

To measure the LATIS spectral accuracy, the transmission spectra of the three 1-nm filters, 532, 589, and 633 nm, were acquired, normalized, and compared to an Ocean Optics USB4000 spectrometer. Spectra for all filters and both spectrometers were superimposed in Figure 3-10. The values for LATIS are interpolated every 1 nm, which results in a smooth appearance for the spectra. Sub-pixel values are found through this interpolation. The peaks observed with LATIS occur at exactly 532, 589, and 632 nm. This result is expected because these filters were used to calibrate this system; center wavelengths were assumed to be perfectly located at these spectral values when calibrating. Peaks observed with the Ocean Optics spectrometer occur at 531.3, 589, and 632.4 nm, revealing that the true center wavelengths fall short of the expected center wavelengths, but they are still within tolerance provided by the filter specifications. Small peaks occur at 560 and 630 nm for data acquired with the 532 nm filter. The existence of these peaks is due to lateral chromatic aberration on the detector images acquired with 532 nm illumination; thus, the source of the noise is unexpected crosstalk and not a reconstruction error.

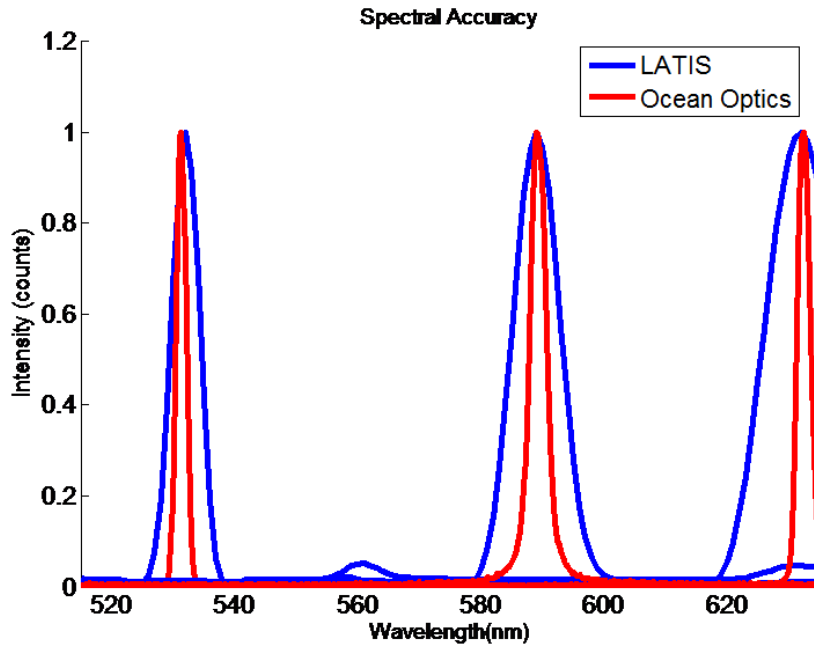


Figure 3-10. Spectral accuracy comparison of 1-nm filters between LATIS and an Ocean Optics USB4000 spectrometer.

3.5. Bead Imaging Experiments with LATIS

To observe the spectral difference between the two tuning settings of LATIS, data cubes were acquired of a fluorescent sample containing two different beads with close emission peaks (605 and 613 nm). The sample (Invitrogen FocalCheck test slide #2) was illuminated by a 120W X-Cite metal halide lamp, and fluorescence signal was gathered by a Zeiss EC Plan-Neofluar 20x (.5 NA) objective. Figure 3-11(a) shows 8 selected spectral channels of the total 46 channels of both beads acquired using tuning setting 2. Figure 3-11(b) and (c) show plots of the superimposed spectra- for both beads acquired with tuning settings 1 and 2, respectively. Hyperspectral data

cubes were acquired in a single exposure time of the camera and reconstructed post-acquisition. Spectral channels were pseudocolored with a wavelength-to-RGB conversion algorithm [Bruton]. Smaller emission widths can be seen at tuning setting 2 when compared against tuning setting 1. The peaks in setting 1 overlap each other; however, they are distinguishable and separated by about 8 nm spectrally in setting 2.

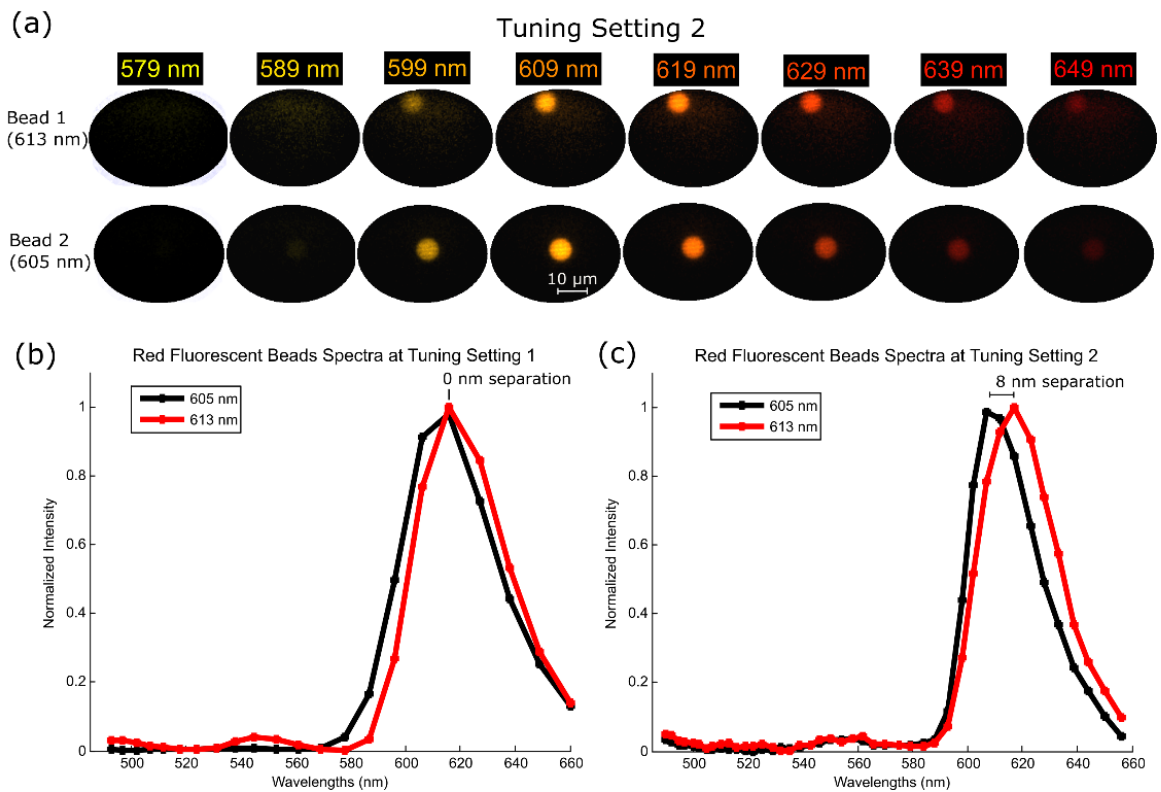


Figure 3-11. Fluorescent beads measured with LATIS.

Fig. (a). Eight-selected spectral channels from the 46 spectral channels of tuning setting 2 in which the fluorescent beads (613 nm and 605 nm) are imaged. Fig. (b). The recorded spectra using tuning setting 1 of both beads superimposed. Fig. (c). The recorded spectra using tuning setting 2 of both beads. The smaller emission width is due to the improved spectral resolution.

Peaks no longer overlap when compared to the previous setting, giving an 8 nm separation

3.6. Fluorescence Imaging with “Static” LATIS

To gauge image quality with the static LATIS and to demonstrate larger data cubes, BPAE cells and mouse tissue, prepared off-site, were imaged. Samples were illuminated by the X-Cite lamp.

BPAE cells (Thermo Fisher F36924), containing Alexa Fluor 488 ($\lambda_{em} = 512$ nm) and MitoTracker Red ($\lambda_{em} = 599$ nm), were excited, and the signal was collected with a Zeiss oil immersion Plan-Apochromat 63x (1.4 NA) objective. To image BPAE cells, the LATIS's front objective was changed to a Zeiss EC Epiplan-Neofluar 1.25x (0.03 NA, $f = 132$ mm) objective (see Figure 3-7). The bandpass filter was changed to transmit 515 through 635 nm. The datacube size was 200x200x27 for all images acquired of BPAE cells. The integration time was .67 s, and camera gain was 25 dB. Eighteen reconstructed spectral channels of the 27 channels are displayed in Figure 3-12. The green channels were multiplied with a gain of 3.33x relative to the red channels to enhance the brightness of Alexa Fluor 488 for display purposes only. By observing the averaged spectrum of the region in the red box, the emission peaks of Alexa Fluor 488 and Mito Tracker Red can be distinguished. The difference in intensity between fluorophores is apparent, showing the Alexa Fluor 488 peak is 4.42x smaller. Mito Tracker red easily saturates at this integration time. With a brighter green dye, a shorter exposure time would be possible.

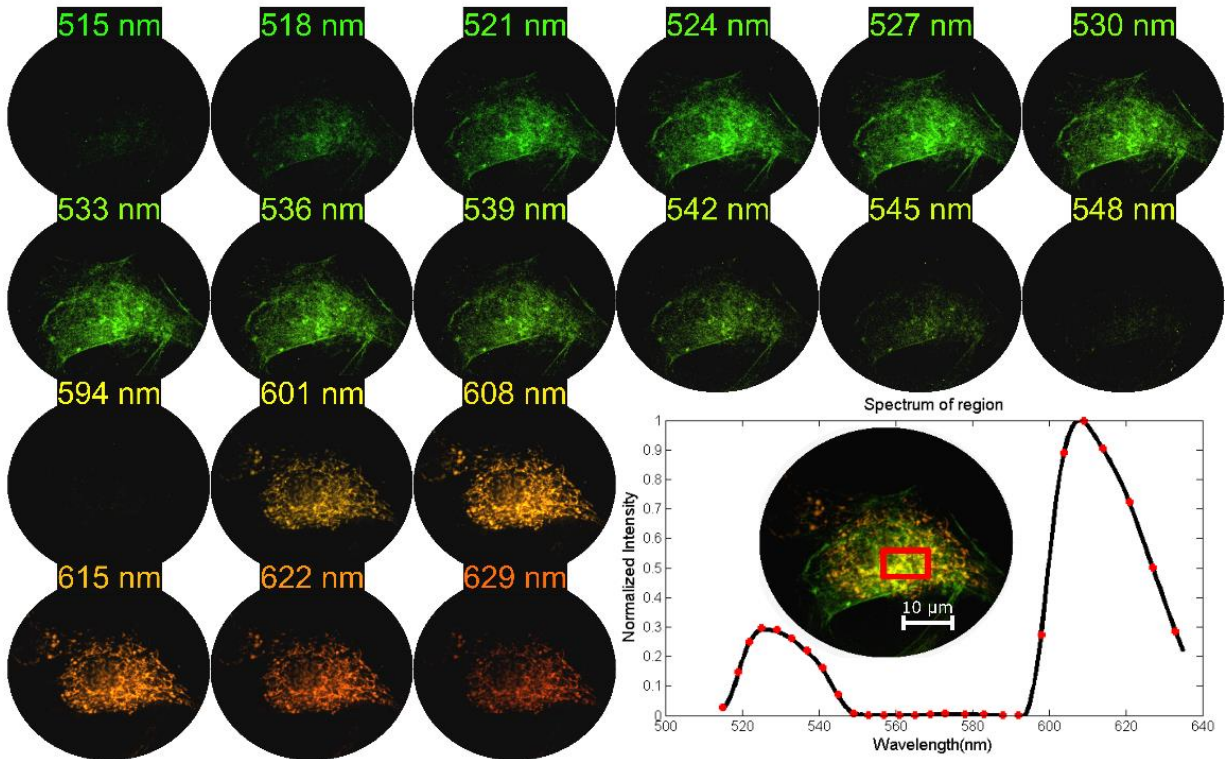


Figure 3-12. BPAE cell imaging with the static LATIS.

Using a bandpass filter of 515 to 635 nm, the datacubes acquired were 200x200x27. Eighteen spectral channels are displayed. The averaged spectrum in the red region is shown. Red markers are pixel values and the black lines are interpolated values.

The imaged mouse tissue contains Quantum dot 655, which was injected into the cerebrospinal fluid of the cisterna magna of live mice. Lymph nodes were harvested post-mortem, containing coalesced quantum dots. For further information, see [Mathieu 2013]. Fluorescence signal was gathered by a Zeiss Epiplan-Neofluar 5x (0.15 NA) objective. A new bandpass filter in LATIS limited the spectral range from 570 nm to 670 nm (see Figure 3-7). The front-optic magnification was 5x. Spectral sampling was 17 pixels in this configuration, giving a datacube size of 200x200x17

for all images of quantum dots. Datacubes were acquired with a 5 second exposure time of the Imperx camera with a 20 dB gain. Longer exposure times were required in this setup due to the low NA of the objective imaging the sample (0.15 NA), which was chosen for its lower magnification to see the entirety of the lymph node. Exposure times <1 sec are possible with higher camera gains. In Figure 3-13, 15 spectral channels of the total 17 are displayed and pseudocolored. A plot of the averaged spectrum of the region outlined in yellow box reveals the emission spectrum of the quantum dot. Red markers indicate actual pixel values, and the black lines indicate interpolated spectral values.

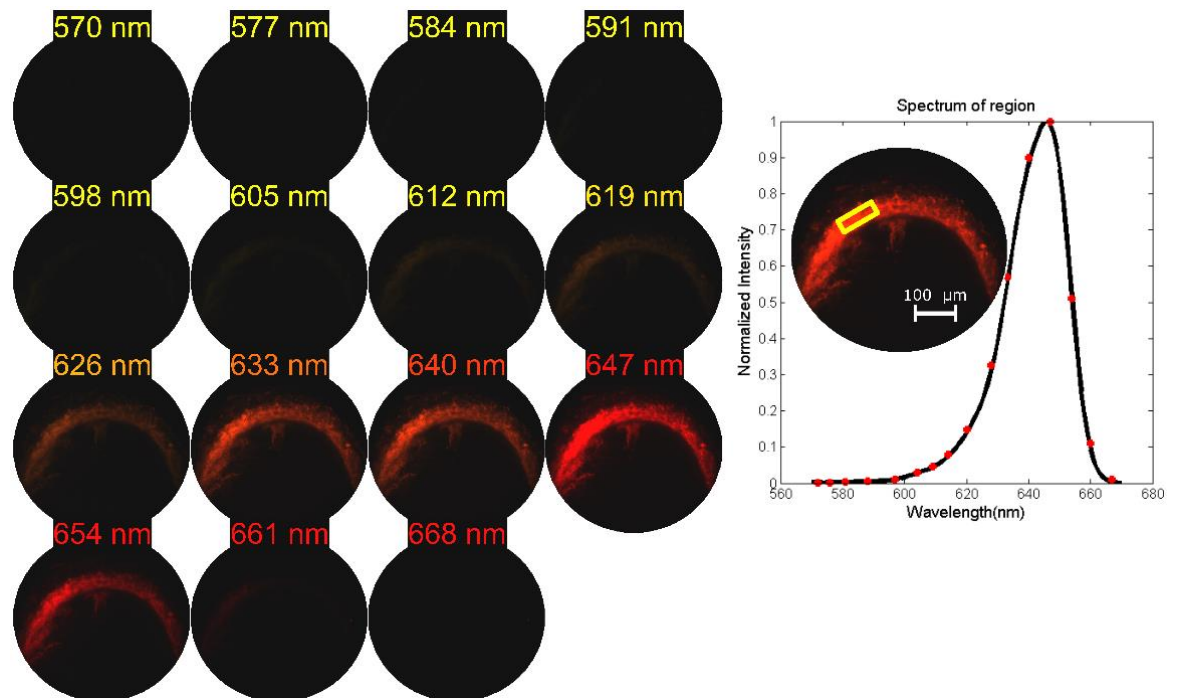


Figure 3-13. Quantum dot imaging of sectioned lymph node mouse tissue using the static LATIS.

Using the 570 to 670 nm bandpass filter, the datacubes acquired were 200x200x17. Fifteen spectral channels of the 17 channels are displayed. The averaged spectrum for the region boxed in yellow is plotted. Red markers indicate pixel values and the black lines are interpolated values.

3.7. Discussion

We have implemented and demonstrated IFS with lenslets for HFM. Additionally, we have designed and tested a system called LATIS with a tunable datacube size, capable of being changed from 80x80x22 to 88x88x46. Spectral resolution improvement is obtained by increasing the focal length of the refocusing lens by a factor of 2 and the focal length of the collimating lens by a factor of 1.5, giving a 33% percent improvement in the spectral resolution while increasing the spectral sampling from 22 to 46 pixels. Two settings were chosen for demonstration; however, the system allows continuous variation of the spectral and spatial sampling as a result of the continuous change between lens focal length settings. Smaller focal length increment changes over the entire focal range of the varifocal lenses can give more tuning settings. To the best of our knowledge, this is the first tunable snapshot spectrometer and a unique demonstration of tunability without a physical change to the dispersive element. To demonstrate applicability in microscopy, we aligned LATIS with the side port of a microscope system and imaged several different biological samples while characterizing the spectral resolution and image reconstruction quality. Only 3 images are necessary for calibration after alignment at each tuning setting. This is advantageous over other IFS systems. Due to the irregularity of fibers and the complex geometry of mirror systems, IMS [Bedard 2012] and IFS fiber systems [Allington-Smith 1998] require a spatial calibration component. The regularity and tightly controlled geometry of lenslet arrays obviated the need for this.

Reconstruction of a resolution target yielded a high quality image with minimal spatial artifacts as shown in Figure 3-8(c). A fixed magnification (“Static”) LATIS was implemented as well to demonstrate a larger FOV as shown in Figure 3-8(d). With off-the-shelf optics and only half the pixel space of a full-frame CCD detector, we demonstrated a datacube size of 200x200x27. Future systems using optimized, high-performance optics and the entire pixel space of a full-frame camera could potentially boast larger data cubes. The spectral resolution was measured using 4 different 1-nm filters for both tuning settings. In Table 3-1, we see a reduction in the measured FWHM of the spectral response of the IMS for all 4 wavelengths, 32.84% improvement at 514 nm, 33.96% at 532 nm, 37.39% at 589 nm, and 42.80% at 633 nm. The theoretical improvement at all wavelengths was expected to be 33.33%, which was achieved at 514 and 532 nm. The deviation from the theoretical improvement at 589 nm and 633 nm is attributed to chromatic aberration present in tuning setting 1. The larger f-number of the varifocal lenses at longer focal lengths mitigated the chromatic aberration seen at longer wavelengths. Future experiments are being planned to understand the extent of resolution and the irradiance per pixel trade-off.

Light throughput for both systems was limited due to the consumer-grade selection of lenslet arrays, collimating lenses, and refocusing lenses. The lenslet array, for example, lost light due to scattering at the polymer and glass interface. The present lenses were sufficient to demonstrate tunability and HFM, but future systems can be optimized for light throughput and better general performance to improve the

field of view and chromatic aberration. Future systems can also provide larger datacube sizes with higher grade varifocal optics. An important improvement we plan to make is the addition of a fixed image plane to prevent re-alignment of the detector at each new tuning setting. Defocus of the image plane is common for varifocal lenses, but future lenses can be parfocal zoom lenses.

A beneficial use of the system resides in situations where the level of expression of one fluorophore is less than the expression of another; the system can increase its dynamic range by acquiring the same scene with the same excitation energy and exposure time at different tuning settings. By processing these images, the system can acquire the spectra of the fluorophores that would otherwise have been outside the dynamic range or below the spectral resolution of a static system. Additionally, the system would prove beneficial for discerning the minimal spectral datacube content required for imaging novel experimental conditions. In biological imaging where every photon can matter, new and unexplored imaging scenarios can be viewed by LATIS. Optimal datacube size and resolution requirements can be ascertained for these imaging situations for future system design. Once desired parameters for a particular biological scenario can be identified, static systems meeting the exact requirements can be built and dedicated for that particular application. Improvements need to be made to the system such as better light throughput, but the results offer promising utility in HFM

Chapter 4

Oximetry of Retinal Vessels using the Image Mapping Spectrometer*

*The contents of this chapter have been published in the following journal article: Dwight JG, Weng CY, Coffee RE, Pawlowski ME, Tkaczyk TS, "Hyperspectral Image Mapping Spectrometry for Retinal Oximetry Measurements in Four Diseased Eyes," Int Ophthalmol Clin. 2016 Fall;56(4):25-38

This chapter presents a calibration-free technique by which the oxygen saturation values in retinal vessels can be measured. By using the IMS, we investigate the IMS's ability to distinguish arteries and veins while measuring the absorbance in each vessel

4.1. Introduction

Inadequate oxygenation of the eye perturbs retinal function and processes, and can lead to visual loss [Yu 2001]. The difference in oxygen saturation between the retinal arteries and veins correlates with oxygen metabolism. When light interacts with the retina, spectral reflectance is generated; this conveys information about the state and composition of retinal tissue, including oxygen saturation [Delori 1988, 1989]. Light has been used to estimate oxygen saturation levels non-invasively based on the unique spectral signatures of oxyhemoglobin and deoxyhemoglobin in the retinal blood vessels. Notable publications in the past have acquired oximetry data using only two- or three-wavelength measurements of the eye [Delori 1988, Hickam 1963, Laing 1975]. However, the acquisition of oxygen saturation values is complicated by undesired scattering and absorption effects due to heterogeneous tissue properties; extensive calibration procedures are required to account for these effects. Significant work has been done to address the challenges in obtaining accurate oxygen saturation measurements posed by vessel diameter differences, variations in pigment, and scattering and absorption effects of blood [Beach 1999, Smith 1999, 2000, 2001, Hammer 2008].

Two commercial retinal oximeters based on two-wavelength oximetry, the Oxymap T1 [Hardarson 2006, Geirsdottir 2012] and the Imedos oximeter [Hammer 2008], have been utilized in a significant portion of the clinical research done regarding saturation measurements in retinal diseases. These systems produce

automatic oxygen saturation maps, but are limited to retinal vessels. Oximetry of choroidal vessels with the Oxymap T1 can be done for lightly pigmented individuals, but its accuracy needs refinement [Kristjansdottir 2013]. Geirsdottir, et al. used the Oxymap T1 to demonstrate that oxygen saturation in retinal veins decreases with age in healthy eyes [Geirsdottir 2012]. Several studies have found reduced oxygen saturation values in occluded arteries and veins [Hammer 2009, Hardarson 2010, 2012, 2013] and increased venous oxygen saturation in patients with exudative age-related macular degeneration (AMD) [Geirsdottir 2014], advanced primary open-angle glaucoma [Olafsdottir 2011, 2014, Mordant 2014], diabetic retinopathy [Hardarson 2012, Hammer 2009, Khoobehi 2013], and retinitis pigmentosa [Eysteinnsson 2014, Ueda-Consolvo 2015]. For patients with retinitis pigmentosa, increased arterial oxygenation saturation and increased arteriovenous oxygen saturation differences have been observed, with age seemingly affecting these values [Battu 2015, Zong 2016]. Another study on primary open-angle glaucoma [Michelson 2006] indicated no change in venous oxygen saturation. Oxygen metabolism is clearly altered in many diseases and trends can be seen in published work, but studies that are more formal are needed to explore the variability amongst studies and better understand the physiological mechanism for altered oxygen metabolism.

Hyperspectral imaging (HSI) allows for the collection of multiple spectral bands in a single image and increasingly utilizes in measuring ocular oximetry [Mordant 2011, 2014, Johnson 2007, Kashani 2011, Jaime 2012, Khoobehi 2004, 2012, 2014]. HSI is advantageous over two- or three-wavelength oximetry in multiple

ways. There is a reduced need for system calibration due to the increased number of spectral channels, which reduces the level of spectral noise [Schweitzer 1995]. Given its greater number of spectral samples, HSI allows one to solve more complex oximetry models with multiple unknown parameters [Schweitzer 1999]. Traditional HSI requires scanning which has several drawbacks. Scanning times require eye fixation and image registration to reduce motion artifacts [Mordant 2011]. Additionally, the total amount of light collected is reduced by a factor proportional to the number of scanned frames required, compromising overall light collection efficiency [Hagen 2012]. Snapshot hyperspectral systems acquire spatial and spectral information of an object simultaneously, and due to the lack of scanning, allow for visualization of dynamic processes free of motion artifact. Previous work has been done utilizing snapshot retinal imaging technology in a system called Computed Tomography Imaging Spectroscopy (CTIS) [Johnson 2007, Kashani 2011, Jaime 2012]. Unfortunately, CTIS is significantly affected by the unfocused background commonly present in tissue imaging and requires long computational times to analyze results. Fiber bundles have also been used for snapshot spectral imaging, but the limited amount of fibers gives low spatial sampling of the fundus image of about 20x20 spatial values [Khoobehi 2012, 2014].

This study focuses on the Image Mapping Spectrometer (IMS), a snapshot HSI with high spatial sampling density (350x350) and 40 spectral channels, which acquires images at the frame rate of the CCD camera [Kester 2011]. This system overcomes previous snapshot limitations associated with CTIS and fibers. We

investigate absolute oxygen saturation values without any prior calibration for a patient with exudative AMD, a patient with non-exudative AMD and borderline glaucoma, a patient with retinitis pigmentosa, and a patient with chronic iridocyclitis to demonstrate applicability in various retinal milieu. Furthermore, we discuss upcoming enhancements of the technology and its algorithms as well potential future applications.

4.2. Materials and Methods

4.2.1. Image Mapping Spectrometry

The Image Mapping Spectrometer (IMS) uses a custom-fabricated mirror array constructed from aluminum to divide an imaged scene into 350 strips. These strips are mapped onto a monochromatic CCD pixel array (Imperx Inc. ICL-B4820M) with unused pixel space, called void space, separating the individual strips. Using a prism array, mapped strips are dispersed across the void space. The dispersed light contains the spectral signature of the imaged object being mapped by the strip. A pixel on the detector corresponds to a unique location in the hyperspectral datacube (x,y,λ) . The present spectral range is 470 to 670 nm, and is limited by the amount of void space separating mapped strips. Additional information about the IMS system can be found in our previous publications [Gao 2009, 2010, 2012, Bedard 2012].

The IMS was integrated with a Topcon TRC-50EX camera using the top port (Figure 4-1). The use of the IMS did not require any physical alteration to the fundus

camera besides a frame that mounted the system to the camera's body. The installation of the IMS did not affect the fundus camera's operation by the clinician. A model eye was used to align the imaging system. All images were captured with a 50° field of view, which allowed visualization of both the optic nerve and macula in a single image. The IMS's electronic shutter was synchronized with the Topcon's xenon flash using the TTL signal from the joystick. The xenon flash's brief duration avoided patient discomfort while providing enough light intensity for the IMS's full dynamic range. Due to a variable delay between the flash and TTL signal, the IMS's exposure duration was 200 ms once triggered. The flash intensity was controlled through 21 different flash settings on the dashboard of the TRC-50EX to adjust for different levels of fundus reflectivity. The discrete settings range from 12 Ws (Watt-seconds) to 300 Ws and increase logarithmically. Typical flash settings used on patients were between 12 Ws and 50 Ws. To prevent saturation of the IMS camera at 12 Ws, a neutral density filter with an optical density of 0.3 was inserted into the aperture stop of the IMS system. The IMS camera was triggered by a dedicated flash button integrated with the fundus camera joystick. Acquired raw data was analyzed off-site in Matlab.

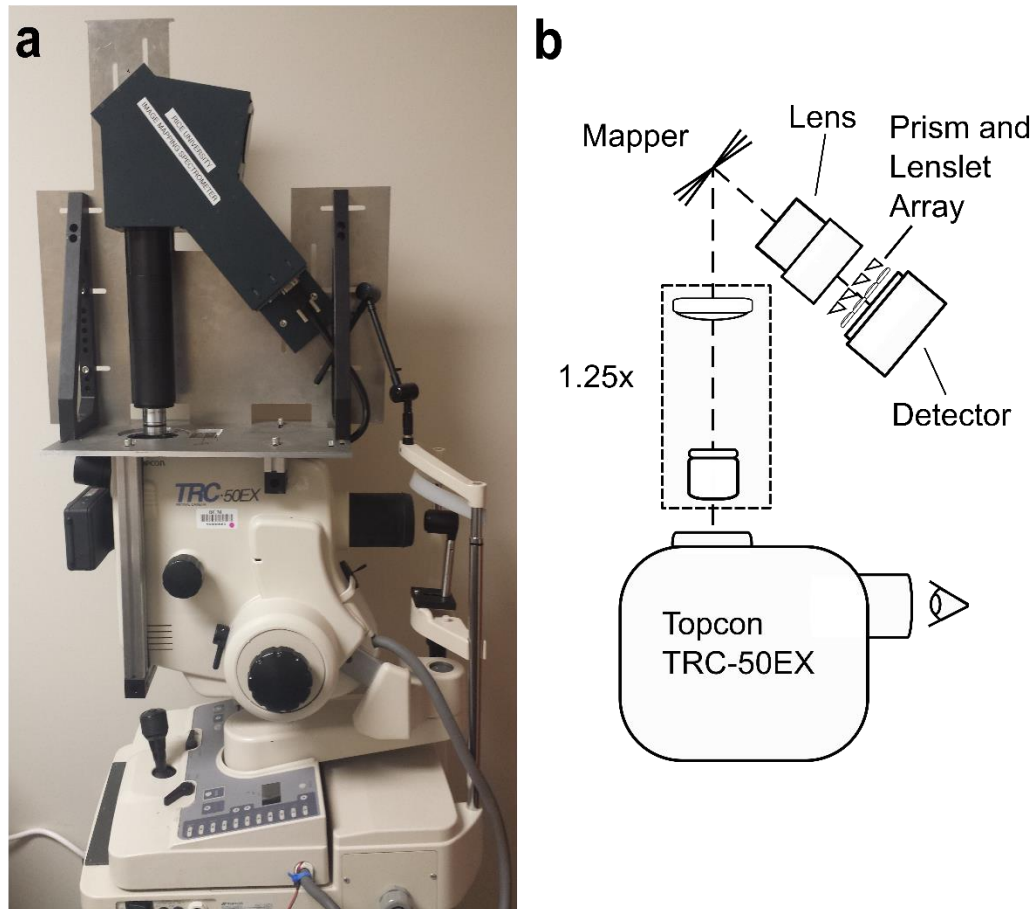


Figure 4-1. The IMS mounted onto a TRC-50EX fundus camera.

Fig(a). The IMS provides a 1.25x magnification of the top port image. Fig(b). The mapper splits the image into 350 strips and images these strips onto the detector (Imperx Inc. ICL-B4820M).

These strips are dispersed onto the detector via a prism and lenslet array. The hyperspectral datacube size is 350x350x40 once the unprocessed images are reconstructed in Matlab.

4.2.2. Oximetry

The calculation of oxygen saturation is based on the equation for the absorbance of whole blood.

$$A_{\lambda} \cong S(\lambda) + s * c * d \left[OS * \left(\varepsilon_{HbO_2}(\lambda) - \varepsilon_{Hb}(\lambda) \right) + \varepsilon_{Hb}(\lambda) \right]$$

Equation 4-1. Absorbance of whole blood

Where c is the total hemoglobin concentration, d is the path length, OS is the oxygen saturation, and s and $S(\lambda)$ are scattering terms caused by red blood cells [Delori 1988]. When $S = 0$ and $s = 1$, the equation reduces to the absorption for hemolyzed blood. $\varepsilon_{HbO_2}(\lambda)$ is the extinction coefficient of oxy-hemoglobin, and $\varepsilon_{Hb}(\lambda)$ is the extinction coefficient of deoxyhemoglobin. The values of these coefficients have been previously published [Meinke 2007]. Absorbance is related to the transmittance of the vessel in accordance with the Beer-Lambert law by

$$A_{\lambda} = -\log(T_{\lambda})$$

Equation 4-2. Conversion from transmittance to absorbance

Since transmission measurements of the vessels are not accessible in the eye, the transmittance is calculated as

$$T_{\lambda} = \frac{V_{\lambda}}{B_{\lambda}}$$

Equation 4-3. Transmittance approximation in the eye

Where V_λ is vessel reflectance and B_λ is the fundus background reflectance adjacent to the vessel. This relationship gives approximated transmittance values. The normalization of vessel reflectance by adjacent fundus background reflectance removes spectral components associated with the background. This approximation does not account for all scattering effects, such as lateral diffusion from adjacent tissue and may affect the estimate's accuracy. For the purposes of simplicity, the calculation of OS is reduced to the calculation of OS for hemolyzed blood. The parameters c , d , and OS are solved by a best least squares fit (LSQ) to the measured absorbance of the vessels using the IMS's 40 spectral values. The term, cd , is bound from 0 to 1, and the oxygen saturation, OS, is bound from 0% to 100%. Oxygen saturation is found by averaging the absorbance measurements using every pixel within a certain region in the vessels.

To account for the difference in spectral resolution between the IMS and the spectrometers used to acquire published extinction coefficient data, the published values [Meinke 2007] were mathematically convolved with the spectral response of the IMS. The IMS's spectral response was modeled by measuring the spectrum of 5 filters with a 1-nm bandwidth at different positions in the spectral range and interpolating the response at all wavelengths (Figure 4-2).

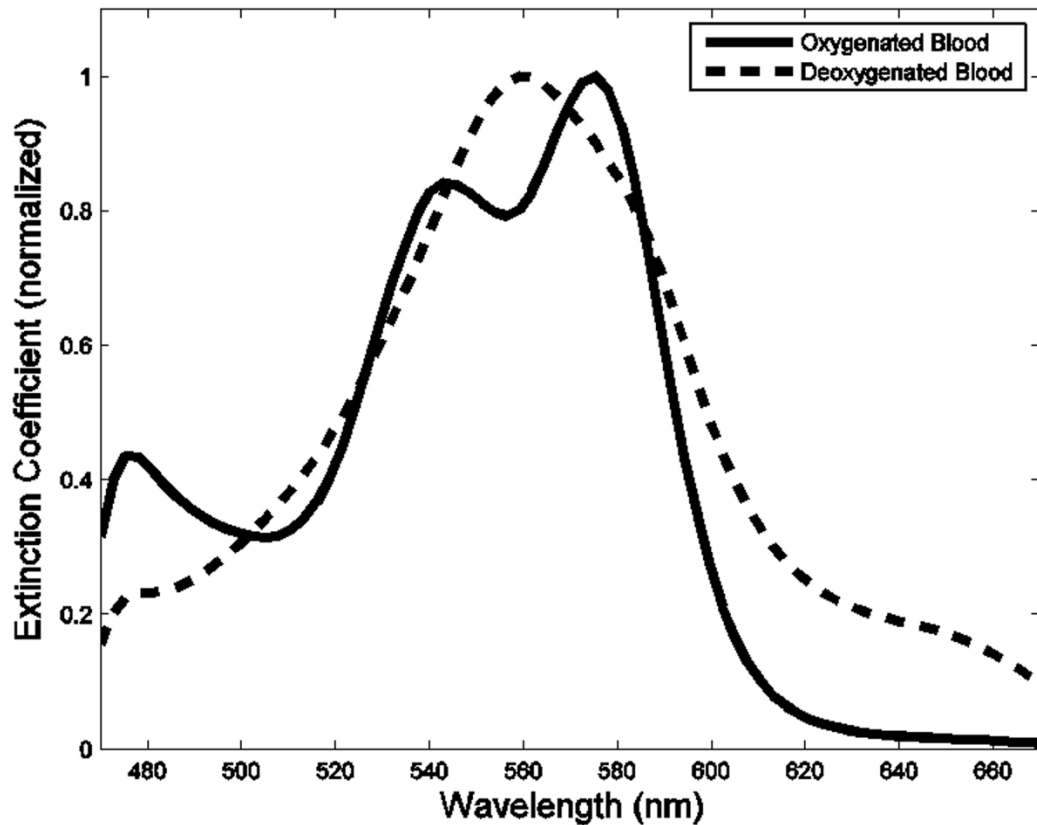


Figure 4-2. The normalized extinction coefficients of oxygenated and deoxygenated blood after convolution with the spectral response of the IMS

4.2.3. Oximetry Maps

Oximetry maps overlay oximetry values along the lengths of retinal vessels in a pseudo-colored fundus image to demonstrate the change in OS with respect to position. Oximetry maps allow researchers to observe oxygen change in diseased eyes and have elucidated oxygen metabolism for a variety of conditions [Hardarson 2006, Hardarson 2013]. To construct oximetry maps with the IMS, the vessels were separated from the fundus background by manually drawing a mask in Matlab. The

mask was then segmented into separate 100-pixel areas. The reflectance spectrum was averaged for each 100-pixel segment. To calculate transmittance, the averaged reflectance spectrum was divided by the mean background reflectance spectrum defined as a 100-pixel sampling of the fundus background adjacent to the vessel segment.

4.2.4. Patients

This study included four patients with different retinal pathologies (exudative AMD, non-exudative AMD with borderline glaucoma, retinitis pigmentosa, and chronic iridocyclitis) with the aim of obtaining their absolute oximetry measurements with the IMS. Patients were identified during routine clinical visits at the Alkek Eye Clinic at the Baylor College of Medicine in Houston, TX; all patients were from the panel of a single provider. Patients were formally consented for this HIPAA-compliant study, which was approved by the Baylor College of Medicine Institutional Review Board. Images were acquired by a trained clinician. Images with poor quality were excluded from analysis.

4.3. Results

4.3.1. Hyperspectral Images

Hyperspectral image stacks were acquired for each patient. Each hyperspectral image stack has a datacube size of 350x350x40. We selected eight

spectral channels ranging from 470 nm to 670 nm for display in Figure 4-3. The channels were pseudocolored using a wavelength-to-RGB conversion algorithm [Bruton]. The field-of-view (FOV) of the images was centered on the optic nerve. Contrast between retinal vessels and the fundus background is greatest between 500 nm and 600 nm due to the high absorption of blood at these wavelengths. At the 670 nm wavelength, the contrast between the vessel and the fundus background is very poor. Visualization of choroidal structures is enhanced at wavelengths greater than 600 nm (Figure 4-3). Composite images were formed by combining all 8 spectral channels for each patient (Figure 4-4).

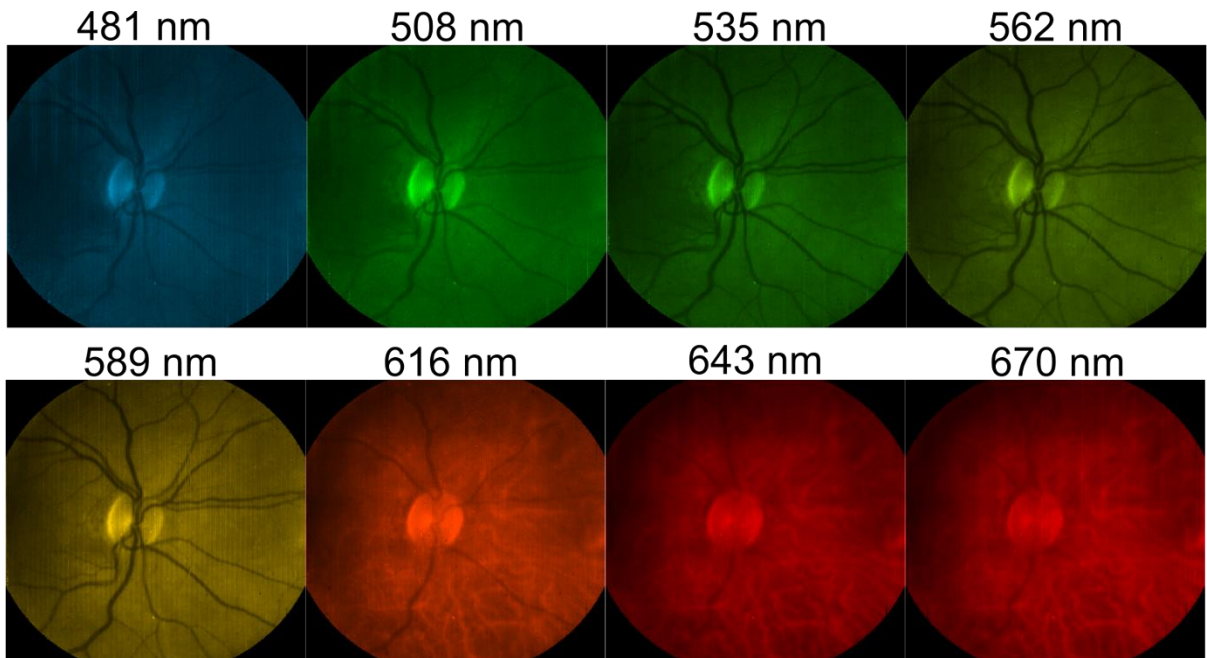


Figure 4-3. Selected spectral channels from an image stack acquired from a patient with AMD. Each spectral channel has been pseudocolored with an RGB value. Notice the artifact from stray light seen in the upper left corner of the image captured at 481 nm; this occurred when the top port of the imaging system was not shielded from ambient light in the room.

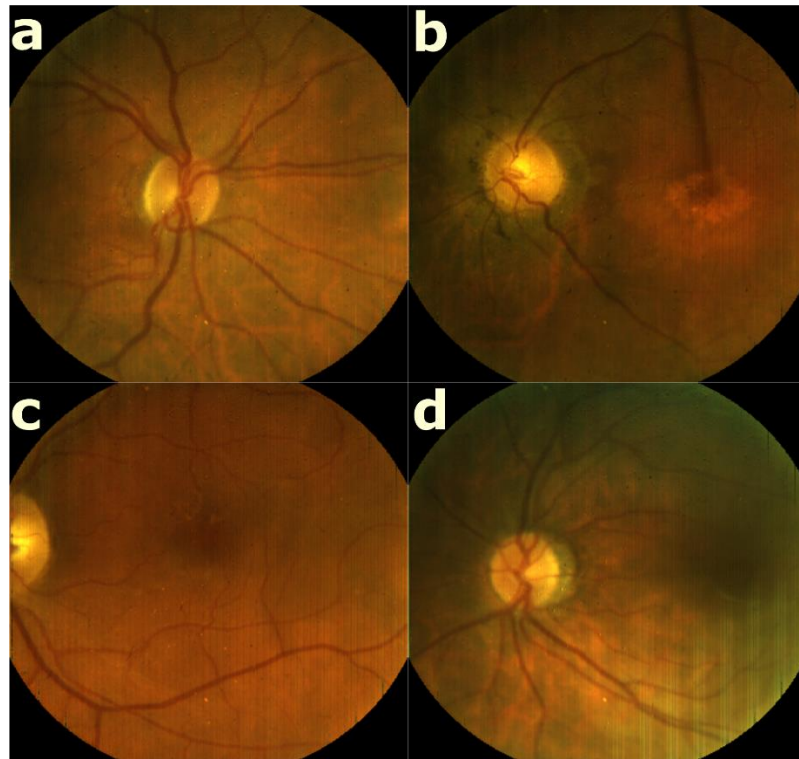


Figure 4-4. Composite images of 8 spectral channels.

Fig(a) a patient with non-exudative AMD and borderline glaucoma, Fig(b) a patient with retinitis pigmentosa, Fig(c) a patient with exudative AMD Fig(d), and a patient with chronic iridocyclitis.

4.3.2. Oximetry

A plot of measured absorbance from the patient with AMD and borderline glaucoma for a 50-pixel region in the retinal artery and a 50-pixel region in the retinal vein is shown [Figure 4-5(a)]. An LSQ fit is also plotted with estimated oxygen saturation [Figure 4-5(b)(c)]. Table 4-1 shows the average oxygen saturation values for all patients. Each oxygen saturation value is derived from a constant region in the patient's eye averaged over several image stacks. Oxygen saturation was found to be 88.6% (± 1.9) and 34.1% (± 7.0) for the retinal artery and vein of the patient with non-

exudative AMD and borderline glaucoma, 100.0% (± 0.0) and 50.4% (± 8.2) for the patient with exudative AMD, 100.0% (± 0.0) and 45.2% (± 7.0) for the patient with retinitis pigmentosa, and 94.1% (± 2.5) and 44.9% (± 5.6) for the patient with chronic iridocyclitis. The arteriovenous differences in oxygen saturation were 54.5% (non-exudative AMD w/ borderline glaucoma), 49.6% (exudative AMD), 54.8% (retinitis pigmentosa), and 49.2% (chronic iridocyclitis).

Table 4-1. Average oxygen saturation in 4 diseased eyes

Patient condition (n = # of measurements)	Artery (%)	Vein (%)	Arteriovenous difference of means (%)
Non-exudative AMD w/ borderline glaucoma (n=5)	88.6 (± 1.9)	34.1 (± 7.0)	54.5
Exudative AMD (n=5)	100.0 (± 0.0)	50.4 (± 8.2)	49.6
Retinitis pigmentosa (n=5)	100.0 (± 0.0)	45.2 (± 7.0)	54.8
Chronic iridocyclitis (n=3)	94.1 (± 2.5)	44.9 (± 5.6)	49.2
Mean (n=18)	95.8 (± 5.1)	43.5 (± 8.9)	52.3

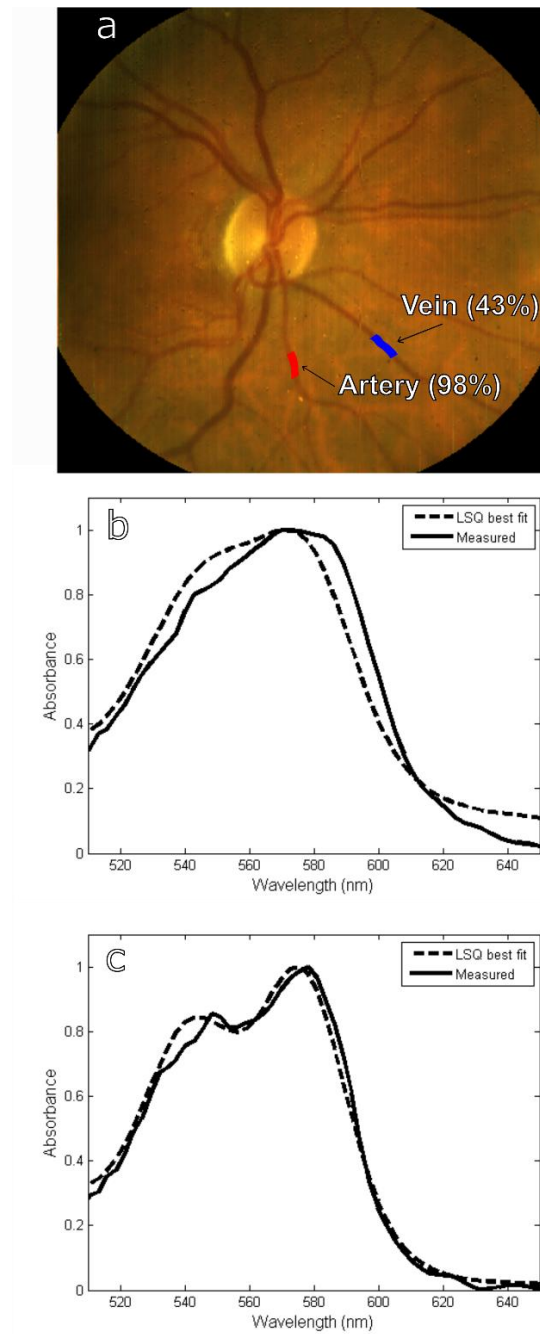


Figure 4-5. Oxygen saturation calculations for two 50-pixel regions.

Fig(a). Using LSQ fitting, the oxygen saturation is estimated for a retinal vein and artery. The fitted curve against the measured absorbance is shown for the retinal vein Fig(b) and the retinal artery Fig(c).

4.3.3. Oximetry map

An oximetry map was generated for the patient with AMD and borderline glaucoma (Figure 4-6). Each segment is 100 pixels in area and color-coded based on oxygen saturation.

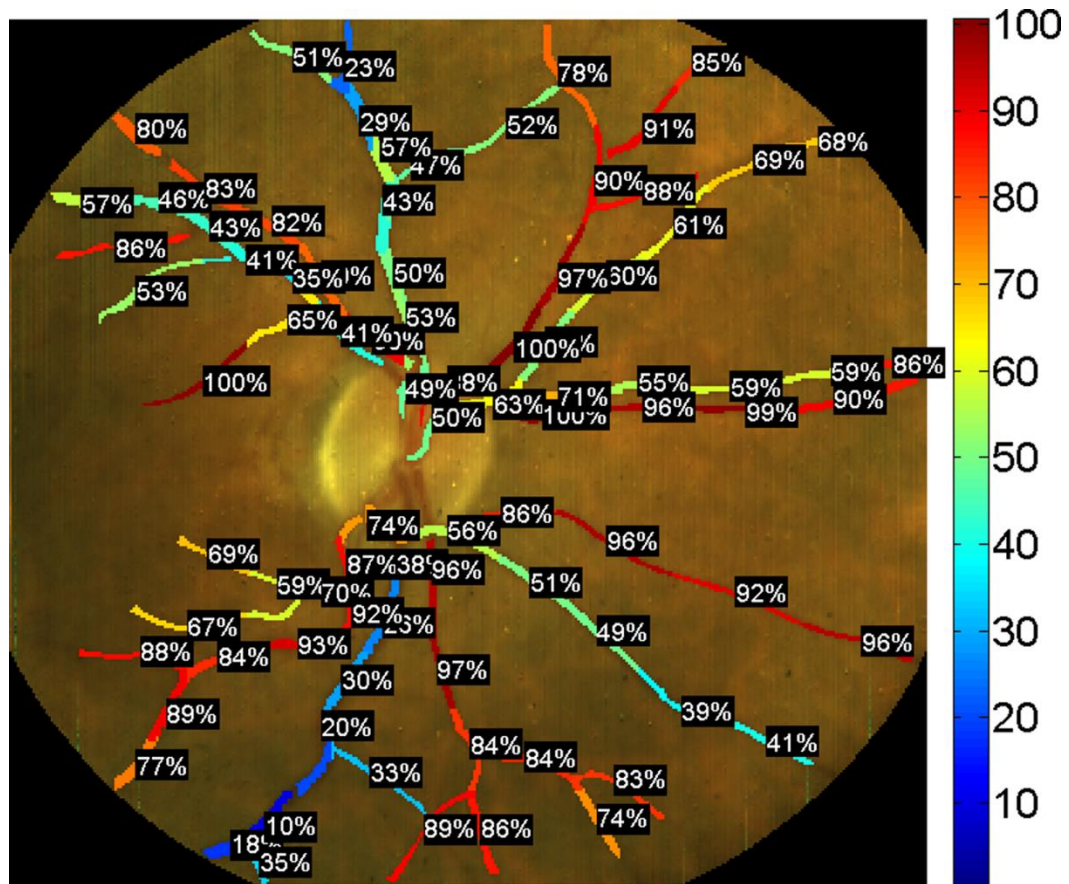


Figure 4-6. Oxygen saturation map of the patient with AMD and borderline glaucoma. Oxygen saturation values are overlaid onto the map in proximity to vessel segments. Vessel segments are color-coded based on oxygen saturation.

4.4. Discussion

The results of this study demonstrate the capability of the Image Mapping Spectrometer to perform oxygen saturation calculations of the retinal vessels in different fundus conditions. The incorporation of the IMS with the TRC-50EX camera did not impede the clinician's ability to observe the fundus and acquire images, although the configuration can potentially be improved. For example, the present CCD camera (Imperx Inc. ICL-B4820M) can be replaced with an sCMOS camera (pco.edge 5.5) to improve detector array performance. The sCMOS detector array offers a faster maximum frame rate (100 fps vs 7.2 fps), wider dynamic range (88.6 dB vs 65 dB), diminished readout noise ($1.0 e^-$ at 30 fps vs $16.0 e^-$ at 3.2 fps), and better quantum efficiency when compared to the present CCD detector array [Semiconductor Components Industries, LLC, pco.edge]. The quantum efficiency is greatly improved in the red and near-infrared region of the electromagnetic spectrum. This region is useful for visualizing the choroidal vasculature due to the deeper penetration of longer wavelengths. Despite the IMS system's high light throughput efficiency of 58% [Bedard 2012], the level of halogen illumination sufficient for image acquisition often caused the patient discomfort. The improved detector array performance of the sCMOS would enable image acquisition with the lower intensity halogen settings, preventing patient discomfort. Thus, hyperspectral images of the eye could be acquired at the frame rate of the camera since halogen illumination is emitted continuously versus the xenon flash, which is emitted intermittently. This allows for

videos of oxygen dynamics in the eye. Another potential area for improvement concerns real-time construction of the hyperspectral data cubes. Currently, this is occurring post-image acquisition, but real-time reconstruction is possible with the IMS [Kester 2011] and would allow the clinician to correct any field-of-view or alignment issues while the patient was still positioned in the machine.

Oximetry calculations performed in this study were based on previous publications using the hemolyzed version of the whole blood oximetry equation. An LSQ solution was used for each measured absorbance spectrum for the pixels sampling a region of retinal vessels (Figure 4-5). Average oxygen saturation was calculated for four patients (Table 4-1). Over 4 patients and with 18 total measurements, the average arterial oxygen saturation was 95.8% (± 5.1) and the average venous oxygen saturation was 43.5% (± 8.9) with an arteriovenous difference of 52%. The variance of oxygen saturation values was small between patients despite different disease states. Using a scanning hyperspectral system and measured mean oxygen saturation values for healthy patients, Schweitzer [Schweitzer 1999, 2001] suggested a normal oxygen saturation of 92.2% (± 4.1) for arteries and 57.9% (± 9.9) for veins with a mean arteriovenous difference of 35%. It is reasonable to assume that different disease states are associated with different levels of oxygen saturation. Elevated oxygen saturation levels have been found in diseased eyes [Geirsdottir 2014, Olafsdottir 2011, Hardarson 2012, Eysteinnsson 2014], but reliable data for healthy controls does not yet exist in order to validate this trend. Another current challenge in interpreting retinal oxygenation saturation values is that different oximetry

systems and techniques tend to produce different measures. Further experiments are needed to validate the oxygen saturation measurements obtained here. The oxygen gradient maps show clear distinction between retinal arteries and veins as expected, but the variation of oxygen saturation values seen with vessel location warrants further investigation.

IMS technology offers multiple advantages over two-wavelength systems. The Oxymap T1 and other two-wavelength systems provide reliable oxygen saturation maps; however, these systems are limited to retinal vessels and do not provide choroidal oximetry for all patients. The IMS's spectral range can be modified to span from green to near-infrared wavelengths, which would also enable the simultaneous visualization of the choroidal and retinal vessels for oximetry. Two-wavelength systems require somewhat arbitrary calibration procedures [Hammer 2008] due to the limited number of wavelength channels. In contrast, hyperspectral systems use more complex oximetry models, mitigating the need for calibration. Additionally, the multi-band spectral signatures of the IMS allow for the probing of more biomolecular signatures, such as different drusen types in AMD [Lee 2010]. The cost of the Oxymap T1 is significantly higher than that of the IMS prototype used in this study (\$72,000 vs \$35,000) [Gao 2012]. The IMS has high spatial sampling compared to other snapshot modalities. In this study, low magnification settings were chosen in order to maximize the FOV, but it might be insightful to evaluate smaller regions of the posterior segment with higher vasculature resolution in future experiments. Additionally, the IMS avoids heavy computational times, and is minimally affected by

unfocused background light. Further improvements to the current setup and algorithms are being planned. Video rate oximetry maps of retinal vasculature would provide useful information about oxygen dynamics. Additionally, there is still little known about choroidal oxygen saturation dynamics, and the IMS technology may provide insight into this area.

We are still learning about the clinical significance of retinal oxygenation saturation levels, but they may play a key role in better understanding disease states and guiding treatment. IMS might be able to provide clinicians with this potentially important data. While the technology still requires validation studies and further investigation into the interpretation of its data output, it holds promise to become a novel and valuable imaging modality in the future.

Chapter 5

Oxygen signal extraction and the measurement of oxyhemoglobin concentration from heterogeneous fundus tissue using hyperspectral Image Mapping Spectrometry

This chapter presents a new way to assess the oxygen content and its spatial distributions within the eye. The aim of this chapter is to use the full capabilities of

the IMS to create a new diagnostic technique for clinicians to determine the health of the fundus.

5.1. Introduction

Oximetry of the retina has received a renewed interest in recent years [Hammer 2008, Hardarson 2006, 2013, Geirsdottir 2012, Beach 2014], despite dating back to the late 1950s [Hickam1959]. However, efforts to improve the power of retinal oximetry using advanced calibration methods [Beach 1999, Smith 1999, 2000, 2001, Hammer 2008], to enable this technique to be used as a clinical diagnostic tool has remained elusive. Work with the commercial retinal oximeters, the Oxymap T1 and the Imedos Oximeter, have contributed to the understanding of the overall oxygen metabolism of the eye for a variety of diseases [Hammer 2009, Hardarson 2012, Geirsdottir 2014], but they have not been successfully integrated into the instrument repertoire of the standard ophthalmology clinic. Common issues with retinal oximeters include an uncertainty of the accuracy of oxygen saturation measurements due to large intravessel variability, difficulty of validation without invasive techniques, and the relegation of oximetry to only large diameter retinal arteries and veins.

Hyperspectral imagers (HSI) in conjunction with fundus camera imaging enables the acquisition of many spectral bands (λ) in the eye in addition to spatial information [Delori 1988, 1989, Khoobehi 2004]. The absorption of chromophores

and the refractive index mismatch between different tissue components in the fundus can modulate the spectral signature of the illumination source of the specialized fundus cameras used in fundus photography. This effect can be measured and exploited to estimate the composition of fundus tissue using reflectance data [Delori 1988, 1989]. A growing area of interest for HSI has been the monitoring of tissue dynamics [Gao 2016]. Indeed many HSI have been employed to measure oxygen saturation within retinal vessels [Mordant 2011, Schweitzer 1999, 2001] and many of these techniques have been non-scanning (“snapshot”) [Johnson 2007, Kashani 2011, Gao 2012, Dwight 2016, Khoobehi 2012, 2014, Alabboud 2007] due to their ability to minimize the effects of eye saccades. The true advantage of these systems over existing dual wavelength retinal oximeters like the Oxymap T1 and Imedos Oximeters lies in their ability to use advanced spectral unmixing algorithms. Using their many spectral bands, they can unmix hemoglobin signatures buried within heterogeneous bulk tissue [Konecky 2015].

The snapshot hyperspectral imager, the Image Mapping Spectrometer [IMS] [Gao 2009, 2010, Bedard 2012], has demonstrated its ability to acquire distinct absorbance spectra from the superior and inferior papillary retinal vessels and its ability to fit oxygen saturation values to these vessel regions [Gao 2012, Dwight 2016]. Owing to their large diameter on the order of 100 to 200 microns, these vessels are well sampled by the IMS with vessel widths being sampled by 3-5 pixels of the IMS’s detector. However, these vessels branch off into smaller capillary vessels, creating a dense network of unresolvable vessels using a conventional wide-angle

setting on a fundus camera. As a result, the absorbance signal of these smaller vessel networks is spectrally buried in individual pixels due to the spectral and spatial overlap of many chromophores in the eye and the tissue heterogeneity in the eye. Using the IMS's 40 spectral channels, we demonstrate a novel technique using a ratio of reflectance between the avascular fovea with the vascularized macula to spectrally unmix these obscured oxyhemoglobin signatures to construct a map of the fundus revealing the spatial distribution of oxyhemoglobin abundance in the eye. The clinical improvement this technique offers over existing oximetry techniques is the ability to co-locate a measurement of oxyhemoglobin abundance with a spatial region of interest in the eye and not exclusively large retinal vessels. We also offer potential improvements over Fluorescein Angiography (FA) as our technique compared to FA is non-invasive and quantifies the abundance of oxy-hemoglobin within the retina. Additionally, we use the technique of non-negative matrix factorization (NNMF) [Ma 2014], a blind source separation technique, which is only possible with a hyperspectral system, to further separate the signal contributions of hemoglobin from the other major chromophores in the eye such as melanin, macular pigment (Lutein and Zeaxanthin), and ocular media [Beatty 1999, Delori 1989]. Previous snapshot HSI techniques have used NNMF to isolate macular pigment absorption spectra from fundus tissue [Fawzi 2011, Smith 2014] and drusen signatures [Lee 2012], but none have attempted to separate oxy-hemoglobin. Linear unmixing has been used to qualitatively enhance the contrast between tissue with high oxy-hemoglobin content and tissue with low oxy-hemoglobin content. [Alabboud 2007],

but has not been explored further. After extraction of these signals, we created a standards curve to convert the signal seen in the eye into oxy-hemoglobin concentration values using a human finger model to relate absorbance measurements made with the IMS to pulse oximetry measurements. This technique is outlined in methods and validated using a small patient cohort composed of two healthy eyes and two diseased eyes, one with age-related macular degeneration (AMD) and one with non-proliferative diabetic retinopathy (NPDR). To the best of our knowledge, this is the first demonstration of an oxygen map of the entire fundus, and the first non-invasive quantification of oxy-hemoglobin concentration in the retina.

5.2. Methods

5.2.1. IMS and Fundus Camera setup

The IMS was integrated onto the top port of a Topcon TRC-50EX fundus camera [Figure 5-1(a)]. The IMS monochromatic detector (Imperx Inc. ICL-B4820M) was synced to the xenon flash of the fundus camera to acquire a hyperspectral image of the relayed fundus image at the top port in a single integration time. The details of this setup have been outline in chapter 4, section 4.2.1.

Using a mirror array, the IMS fractionalizes images relayed from the top port into separated spatial and spectral information with no scanning. Recorded images can be reformatted with minimal computational power into a hyperspectral datacube

(350x350 spatial values, 40 spectral values) over the wavelength of 470 to 670 nm
[Figure 5-1(b)].

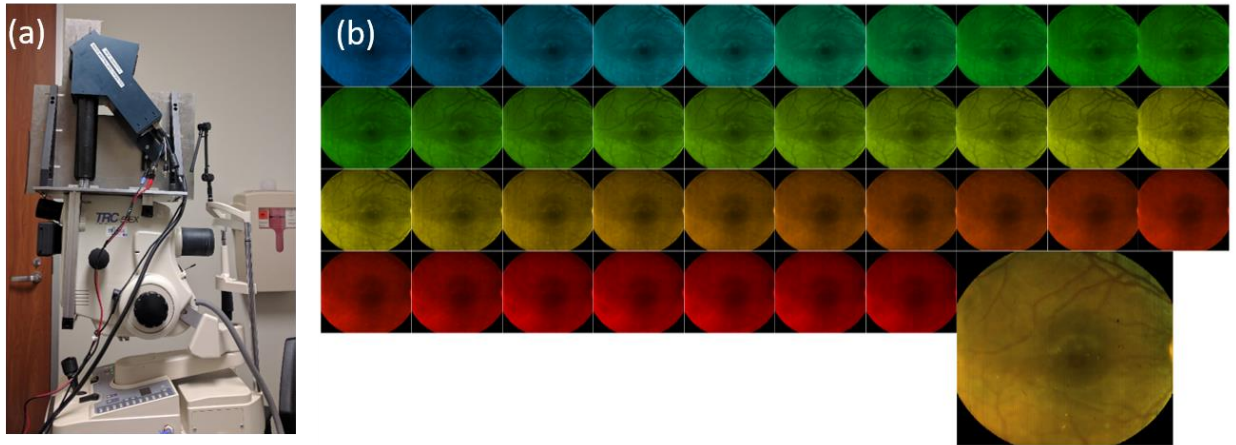


Figure 5-1. IMS setup on Fundus.

Fig(a). IMS mounted to top port of the fundus camera. Fig(b) Selected spectral channels from an fundus image acquired with the IMS spanning the range from 470 to 670 nm.

5.2.2. Oxygen signal Extraction

An average reflectance spectrum from the foveal avascular zone of the macula is used to normalize the average spectrum from different vascular regions of the eye with increasing distance from the fovea. Using a simple model of reflectance based on the Beer-Lambert law [Delori 1989],

$$R_{\lambda} = R_{SC} 10^{-2 * (\sum_p k_{p,\lambda} * d_{\lambda})}$$

Equation 5-1. Reflectance in eye

where R_λ is reflectance, R_{sc} is the reflectance of the posterior sclera, $k_{p,\lambda}$ is the extinction coefficient of macular pigment, p , at wavelength, λ , and d_λ is the optical path length, we can build a model of the reflected signal by dividing vascular regions in the eye, reg , by the avascular fovea, fov ,

$$\frac{R_{reg,\lambda}}{R_{fov,\lambda}} = \frac{R_{sc} 10^{-2(k_{mp,\lambda}d_{mp,reg} + k_{me,\lambda}d_{me,reg} + k_{HbO_2,\lambda}d_{HbO_2})}}{R_{sc} 10^{-2(k_{mp,\lambda}d_{mp,fov} + k_{me,\lambda}d_{me,fov})}} + N$$

Equation 5-2. Division of the reflectance from eye regions

where mp is macular pigment, me is melanin, HbO_2 is oxyhemoglobin, representing 3 major chromophores within the eye, and N is spectral noise. Reducing this equation gives us

$$-\log\left(\frac{R_{reg,\lambda}}{R_{fov,\lambda}}\right) = 2 * k_{HbO_2,\lambda}d_{HbO_2} + 2 * k_{mp,\lambda}(d_{mp,reg} - d_{mp,fov}) + 2 * k_{me,\lambda}(d_{me,reg} - d_{me,fov}) + N$$

Equation 5-3. Simplification of Equation 5-2

and reveals the abundance of oxyhemoglobin within the eye. However, the signal is influenced by the addition of the path length difference of the other chromophores from the different regions in the eye. This path length difference reduces the contribution of these chromophores to the signal. We can further simplify this equation to a representation of weighted spectral absorbances, which are equal to the

-log transformation of the reflectance spectrum of a region with high HbO₂ divided by the reflectance spectrum of a region with low HbO₂.

$$\phi_x = -\log\left(\frac{R_{HighHbO_2}}{R_{LowHbO_2}}\right) = A_{HbO_2}S_{HbO_2} + A_{MP}S_{MP} + A_{ME}S_{ME} + N$$

Equation 5-4. Weighted abundances of different chromophores

Where A is abundance and S is the spectral absorbance for each chromophore. By representing this signal as a weighted sum, we can justify the use of NMF to further separate oxyhemoglobin signal, which is distorted by noise and the spectral contributions of other chromophores. Figure 5-2 demonstrates the change in spectral signature at different regions in the eye using Equation 5-4. The reflectance spectrum retrieved from each region is divided by the reflectance spectrum in region 4. For display purposes, the mean value of each absorbance signature is subtracted from each spectral channel to center the signals across 0. We will refer to the signature, Φ , as absorbance or OD in this chapter. The spectral influence of the xenon source was removed earlier by dividing all spectral values in collected data cubes by the reflected spectral values from a white paper in front of the front objective of the fundus camera. Region 1 shows an increase in oxyhemoglobin signal (characteristic peaks at 540 and 580 nm) when compared to the other regions, indicating the region is more vascularized despite no resolvable vessels within these regions.

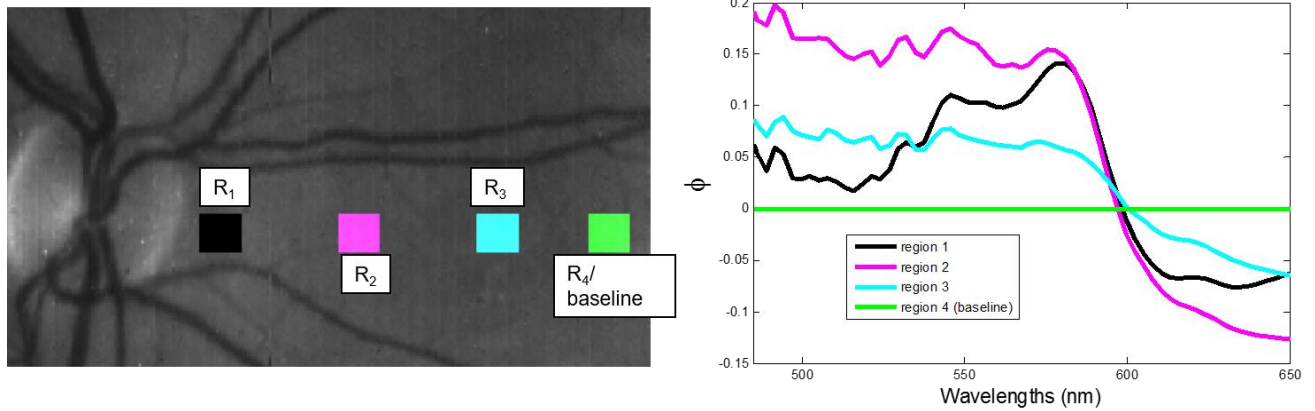


Figure 5-2. The calculated absorbances in an eye by dividing 4 regions by a low oxyhemoglobin region (R4).

5.2.3. Non-negative matrix factorization algorithm

NNMF has been employed in the past to separate oxyhemoglobin from melanin in epithelial tissue [Galeano 2011]. The advantage of NNMF lies in its non-negativity constraint [Montequet 2010], which benefits the imaging scenario we find in biological imaging as spectral endmembers should be positive. Optimization methods to produce a spectral decomposition minimize a cost function [Paatero 1994] to converge to a solution to find the spectral endmember matrix, H ,

$$\min \|A - WH\|_F^2$$

$$s. t. W, H \geq 0$$

Equation 5-5. Cost function for NNMF

where A is a matrix of spectral absorbance retrieved from each eye and W is the weights applied to H . To isolate a pure signal of oxyhemoglobin from the retrieved absorbance signatures in the patient eyes, A , we used an NNMF decomposition using an alternating least squares (ALS) update rule [Paatero 1994]. We started with a rank 2 decomposition for each eye and increased the rank until a distinguishable oxyhemoglobin absorbance spectrum could be identified from the spectral endmember result, H . The algorithm had no limit to the amount of repetitions it could perform until it converged on a result. No constraints or a prior initialization schemes were imposed on the algorithm, hence the selection of ALS due to its performance with no initialization. To analyze the variance between algorithm repetitions, we performed NNMF 50 times and calculated the standard deviation between an endmember's spectral channels.

5.2.4. Finger oximetry model

To validate the oximetry results in the eye, we created a model for oxyhemoglobin concentration change by imaging a human finger with the IMS. We induced the arterial oxygen saturation to lower within the finger over time. The subject was compliant with a Rice University Internal Review Board protocol. To induce arterial oxygen saturation change, thus oxyhemoglobin concentration change, within the patient's finger, the patient held their breath for over two minutes. To ensure his comfort and safety, the patient hyperventilated for several minutes before holding his breath, enabling him to hold his breath for longer than average without

severe discomfort. Using a Masimo Rad-57[®] pulse oximeter attached to the finger of interest, the arterial oxygen saturation could be monitored over time. The finger was illuminated with a halogen lamp (Figure 5-3). A Computar 55 mm prime lens was installed as the front objective of the IMS to image the finger at a distance of a few feet. Hyperspectral data cubes were acquired with the IMS every .5s and the internal memory of the pulse oximeter recorded pulse oximetry values every 2s. The internal clock of the oximeter was synced to the time on the clock in Figure 5-3. Data from the pulse oximeter was uploaded using Trendcom[™] software. The arterial oxygen saturation changed at around 1:20s into the patient's breathholding. The patient released their breath at 2:40s. The lowest arterial oxygen saturation value occurred at around 2:35 seconds. A mean reflectance spectrum was taken at this time (black box in Figure 5-3) and used as the region of low oxygen to calculate absorbance in the finger (Equation 5-4). Absorbance spectra at each acquisition were calculated as a rolling average of three time adjacent spectra signatures. Since the other chromophores within the finger should be constant for this experiment, the absorbance should be a perfect model of oxyhemoglobin concentration change.

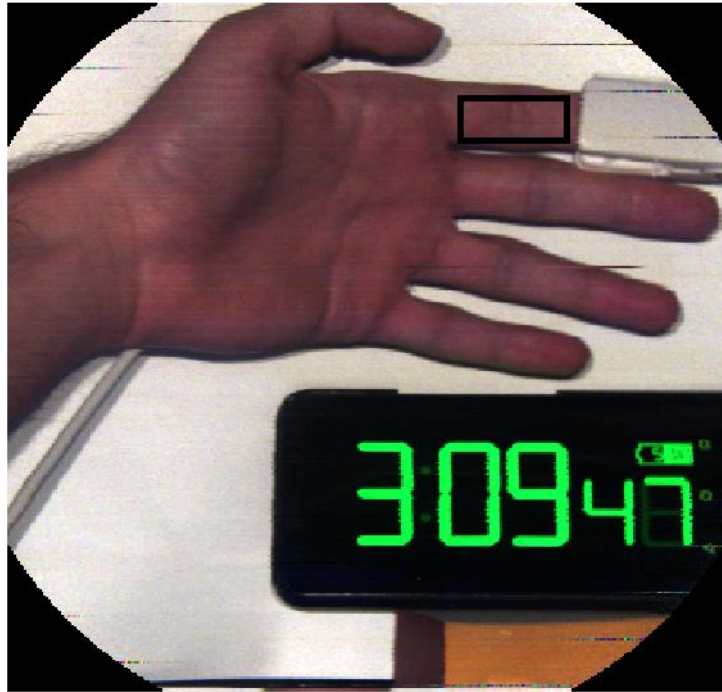


Figure 5-3. Recorded image using the IMS of the finger oximetry setup

5.2.5. Oxyhemoglobin radial maps

Due to the reflectance spectrum similarity between the fovea and the other regions in the eye, the division of signal between them obscures the oxyhemoglobin signal with noise. Using the mean reflectance spectra from the pixel region that represents the fovea (radius of 15 pixels), we explored the effects of using different amounts of pixels for the mean reflectance of the vascularized portion of the eye. The noise level was 17.5% percent at 1 pixel, 9.5% at 5 pixels, 5.8% percent at 10, and 4.8% percent at 40 pixels (Figure 5-4).

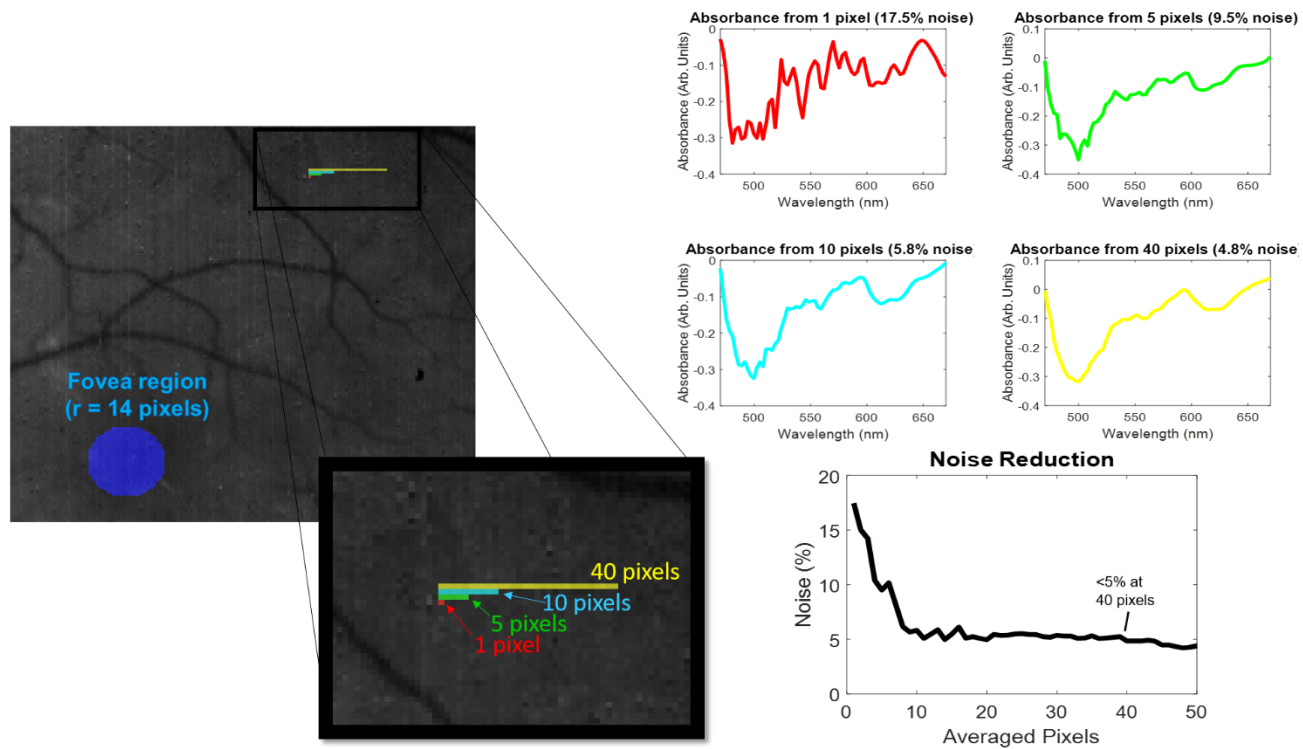


Figure 5-4. Noise reduction of the absorbance spectrum.

To reduce the noise in retrieved absorbance spectra in the eye. The signal was averaged over 40 pixels to reduce the level of noise to <5%.

Radial maps were created and centered on the fovea of each eye. Using 40 pixel regions due to the <5% noise level, the map was divided into 5 rings, each with an increasing radius of 25 pixels. These rings were further divided into 40 pixel segments based on the change in angle in the radial map (Figure 5-5). Absorbance values were calculated for 1518 segments in the two normal eyes and the eye with NPDR. The radial map for the eye with AMD only had 1439 segments due to the map falling out of the FOV of the acquired hyperspectral datacube.

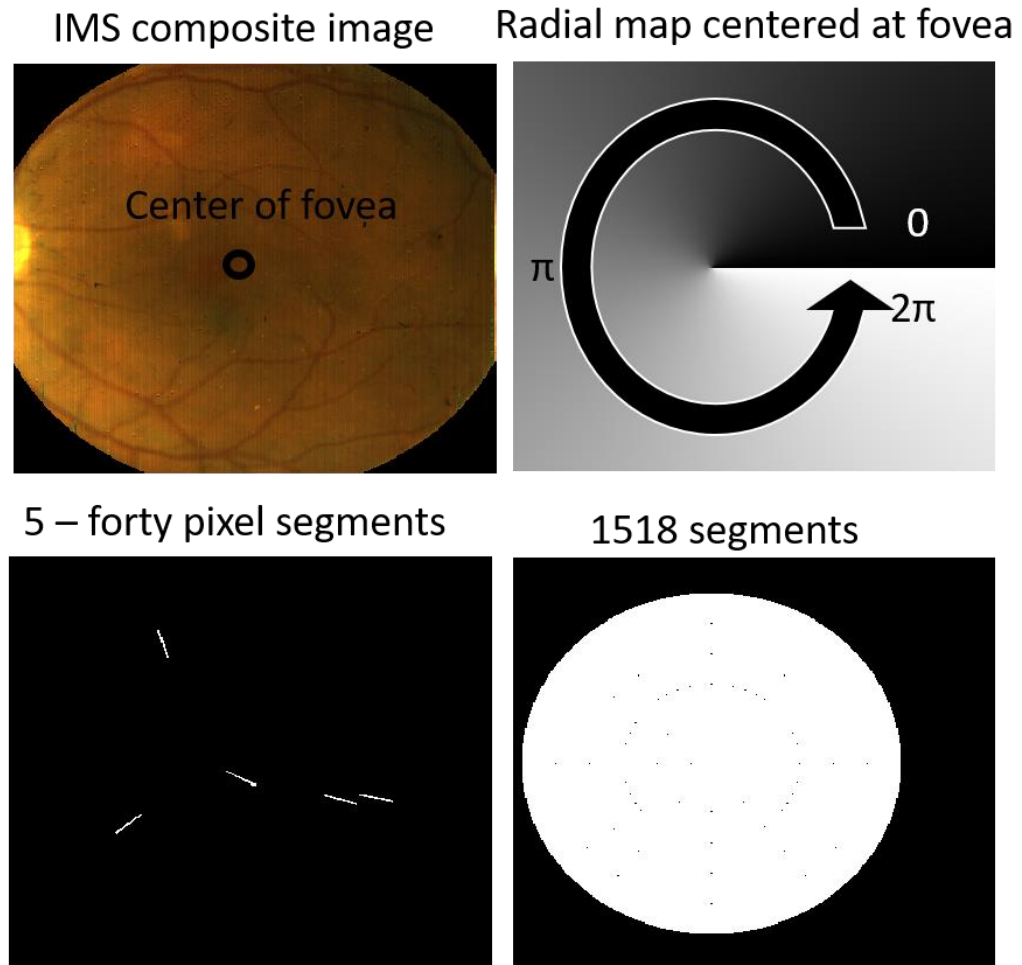


Figure 5-5. Segmentation of a radial map for retinal tissue oximetry.

Using the NMF algorithm to separate oxyhemoglobin from the remaining spectral constituents in the absorbance, each radial region was spectrally decomposed. The normal eyes underwent a rank 2 decomposition, the eye with NPDR underwent a rank 4 decomposition, and the eye with AMD underwent a rank 3 decomposition. To calculate the amount of oxyhemoglobin within each radial

segment, the OD difference between the peak signal intensity between 540-580 nm and the signal at the isobestic wavelength at 500 nm was determined.

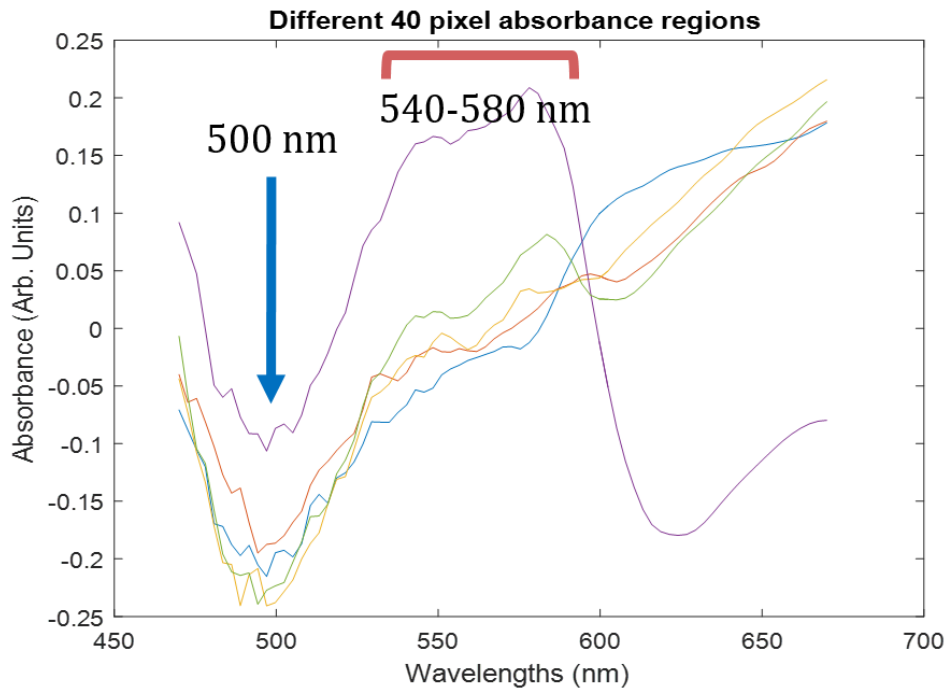


Figure 5-6. Example absorbance spectra from a normal eye, pointing out the isobestic point at 500 nm and the peak oxygen signal between 540-580 nm.

5.2.6. Patients

This study included four patients, two normal eyes, one with NPDR, and one with AMD. Patients were identified during routine clinical visits at the Alkek Eye Clinic at the Baylor College of Medicine in Houston, TX. All patients were from the panel of a single provider. Patients were formally consented for this HIPAA-compliant

study, which was approved by the Baylor College of Medicine Institutional Review Board. Images were acquired by a trained clinician.

5.3. Results

5.3.1. Composite images of eyes

Composite images were created from each eye using eight spectral channels from across the spectral range of the IMS. The channels were weighted with RGB values based on a RGB-to-nm conversion algorithm [Bruton]. Composite images are displayed in Figure 5-7.

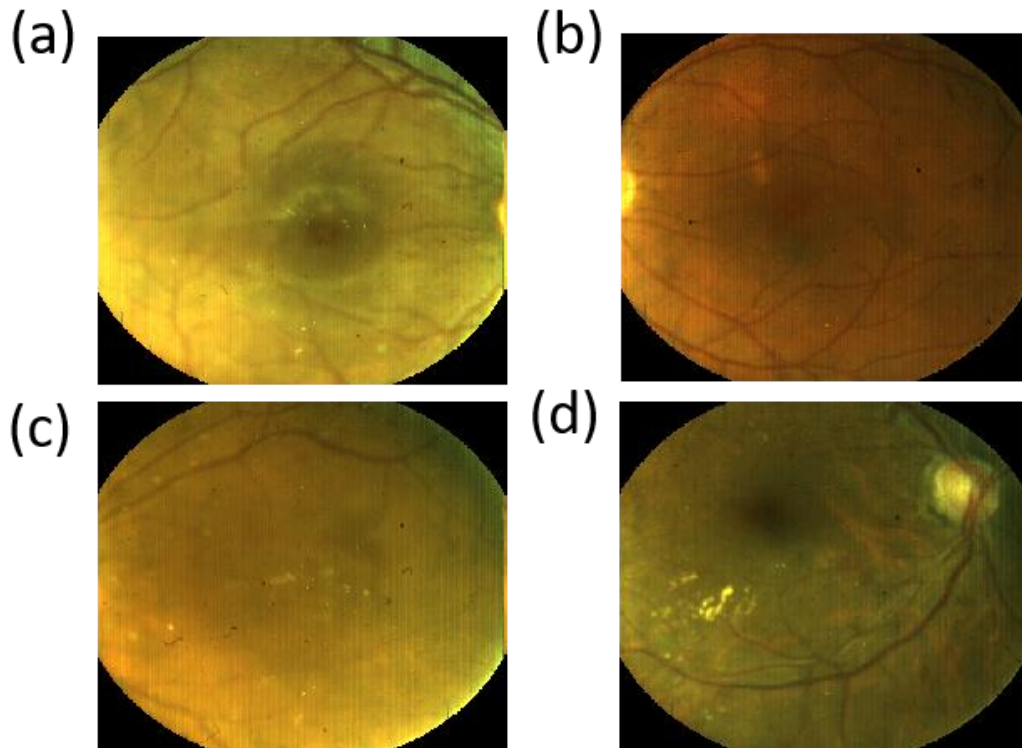


Figure 5-7. Composite images of patient eyes.
Fig(a). normal eye #1. Fig(b) normal eye #2. Fig(c) NPDR. Fig(d) AMD

5.3.2. Finger Oximetry

The absorbance spectra of the finger are shown as a surface plot in Figure 5-8(a). The plot is scaled from 0 to 100 seconds; however, it takes place between 1:20 seconds and 3 minutes of the breathholding. From 0 to 75 seconds in the plot, there is a gradual flattening of the absorbance spectrum. The breath is released at 80 seconds, and we see sharp increase in the absorbance spectrum as it returns to the original absorbance spectral shape of oxyhemoglobin.

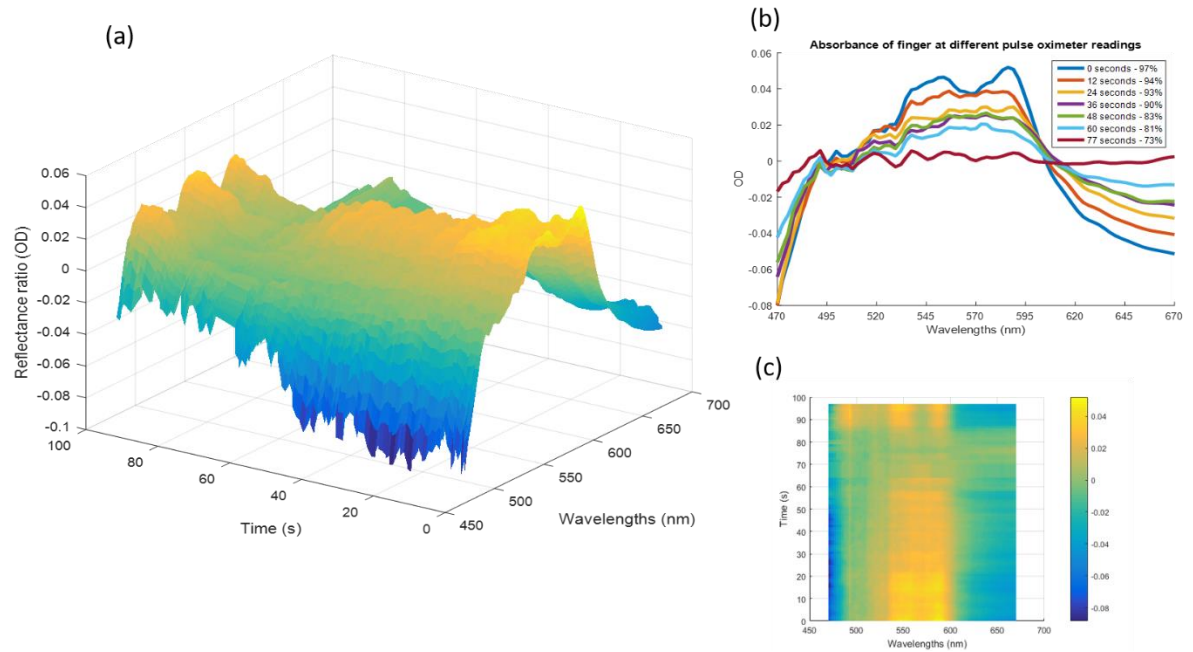


Figure 5-8. Finger oximetry absorbance data.

Fig.(a) Surface plot. Fig(b). Selected spectra at different times Fig(c). :A heatmap showing the change in absorbance

In Figure 5-9, the peak absorbance between 540 and 580 nm was found and OD at 500 nm was subtracted from it. This difference was plotted against time. Additionally, oxygen saturation values recorded from the pulse oximeter were overlaid, shown on the second y-axis. Based on these values, we see a linear dependence of the OD difference on the oxygen saturation values. Best least squares fits were plotted to further illustrate the linear trend.

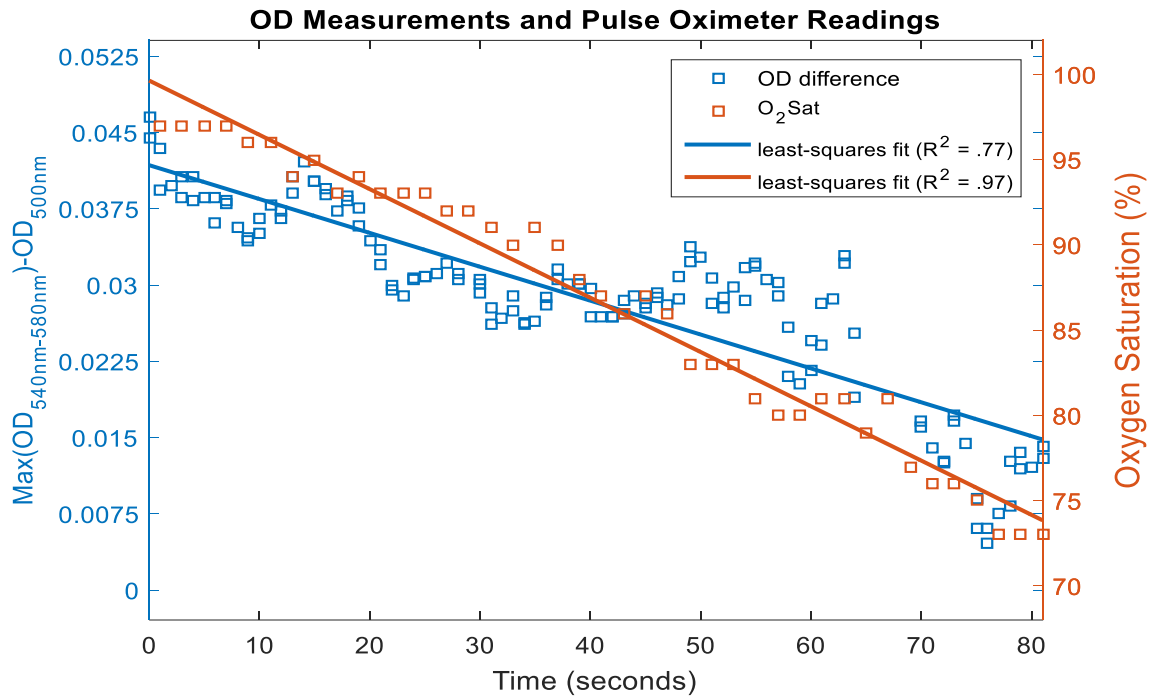


Figure 5-9. Plot of finger OD difference vs time and oxygen saturation vs time.

A goal of these measurements was to create a standards curve to convert the OD difference in signal to a quantitative value of oxyhemoglobin. Oxygen saturation depends on the concentration of oxyhemoglobin and hemoglobin by

$$SO_2 = \frac{C_{HbO_2}}{C_{HbO_2} + C_{Hb}} * 100$$

Equation 5-6. Oxygen saturation

Where SO_2 oxygen saturation, C_{HbO_2} is the concentration of oxyhemoglobin and C_{Hb} is the concentration of deoxyhemoglobin. Since the dependence of oxygen saturation of

blood is linear with respect to oxyhemoglobin concentration, the values of oxygen saturation can be converted into oxyhemoglobin concentration. The average healthy male has hemoglobin concentration of 15 g/dL [Collins 2015]. Based on the best least-squares fit in Figure 5-9, a plot of O₂Sat vs OD was made (Figure 5-10). Further, a plot of OD change vs oxyhemoglobin concentration change was created based off the assumption that the oxyhemoglobin concentration was close to 15 g/dL when the finger's arterial O₂Sat was maximum. A standards curve was thus created to convert OD change within the eye into oxyhemoglobin concentration

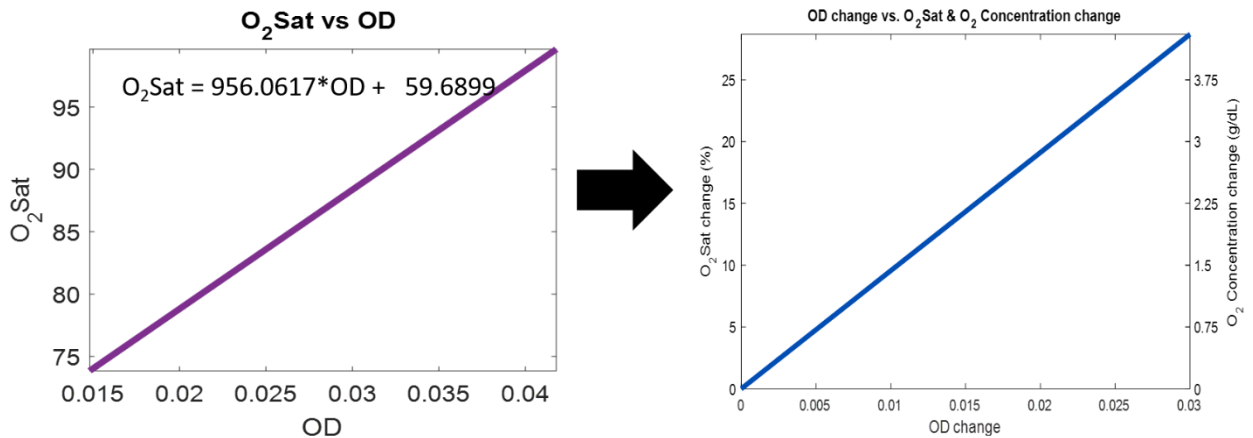


Figure 5-10. Standards curve based off of finger oximetry data.

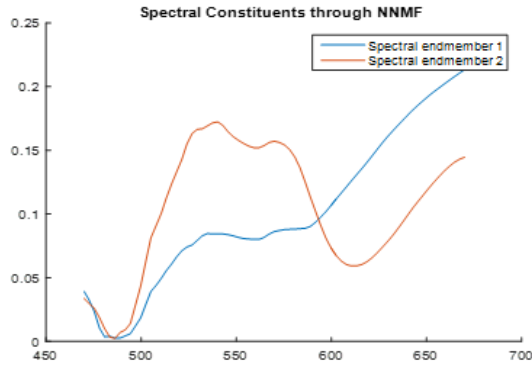
5.3.3. Non-negative matrix factorization

The spectral decomposition using NMF for both normal eyes, the eye with NPDR, and the eye with AMD is shown in Figure 5-11. The normal eyes reliably returned the oxyhemoglobin spectrum at the second spectral endmember location.

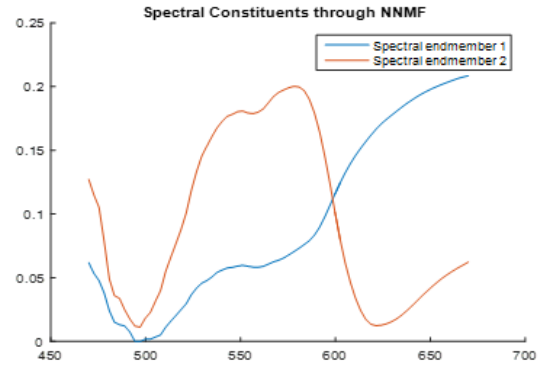
The diseased eyes required higher ranks (4 for NPDR and 3 for AMD) to return oxyhemoglobin. While they consistently returned the oxyhemoglobin spectrum for the 50 repetitions, the spectral endmember number that it was returned as changed at every repetition. This produced high variance for the diseased eyes when compared to the healthy eyes. However, the solution to this problem only required the manual selection of the oxyhemoglobin endmember by the user for these two eyes. If the user selects the correct spectral endmember as oxyhemoglobin, the variance reduces to the level seen with the healthy eyes, which is almost negligible.

Spectral endmembers from NNMF

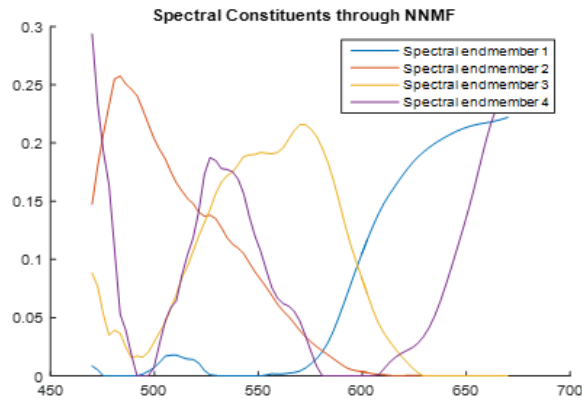
Normal #1



Normal #2



NPDR



AMD

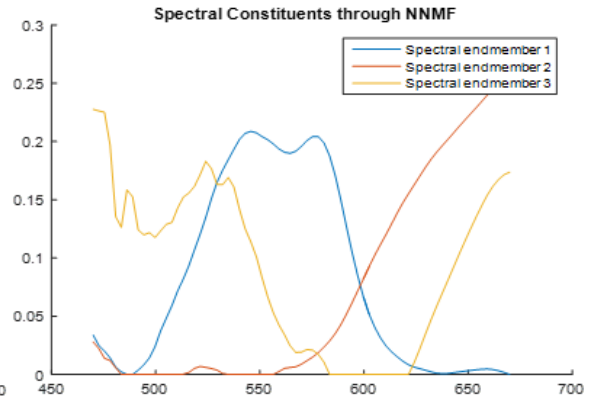


Figure 5-11. Spectral decomposition using NNMF for all eyes.

Variance between 50 iterations

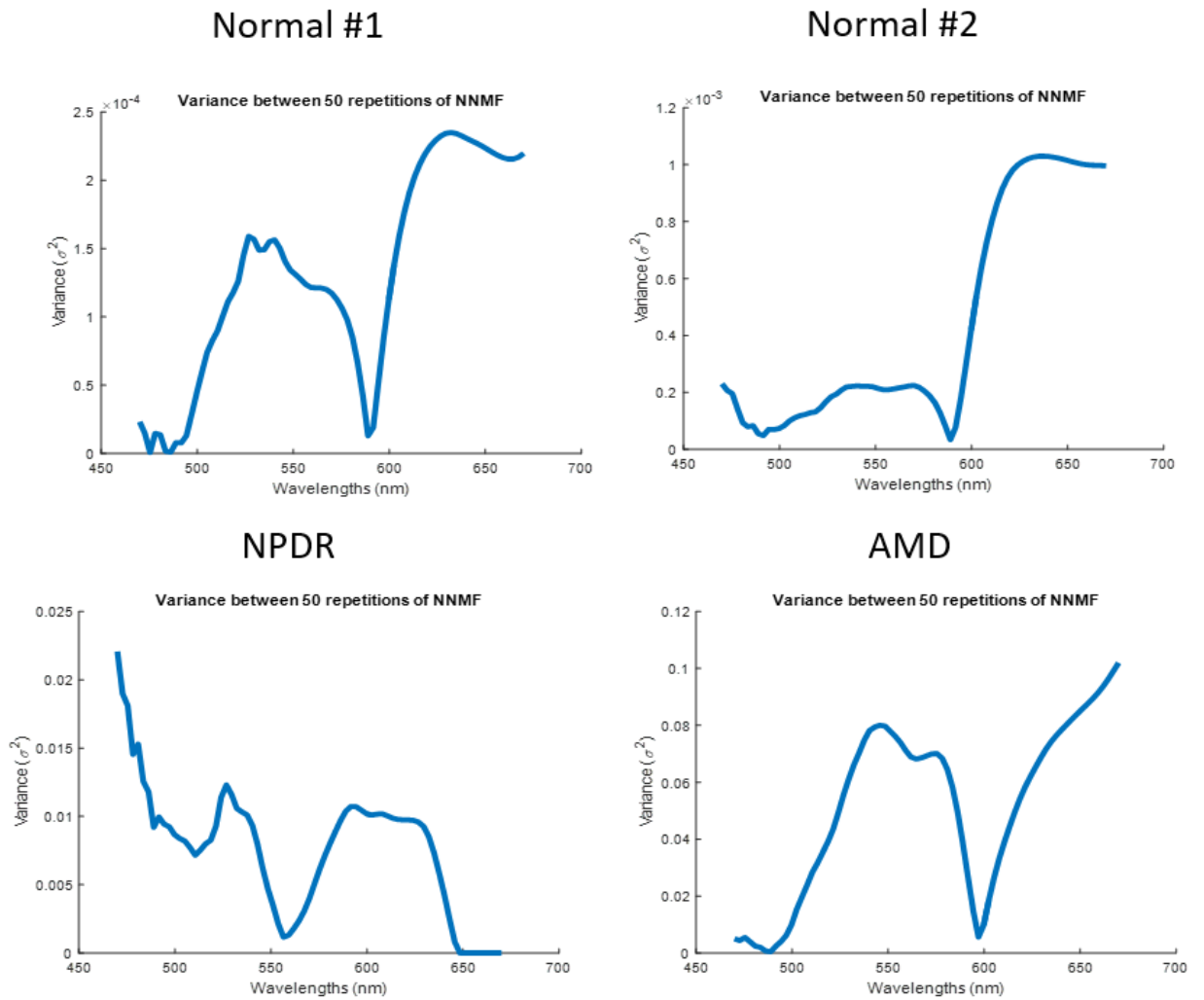


Figure 5-12. Variance between spectral endmember 2 after 50 repetitions of NNMF.

Figure 5-13 shows the original absorbance spectrum at segment 100, 500, 739, 1000, and 1500 (1400 for the eye with AMD). After the spectral decomposition using NNMF, the spectral member representing oxyhemoglobin was weighted based on the returned matrices of W and H (Equation 5-5).

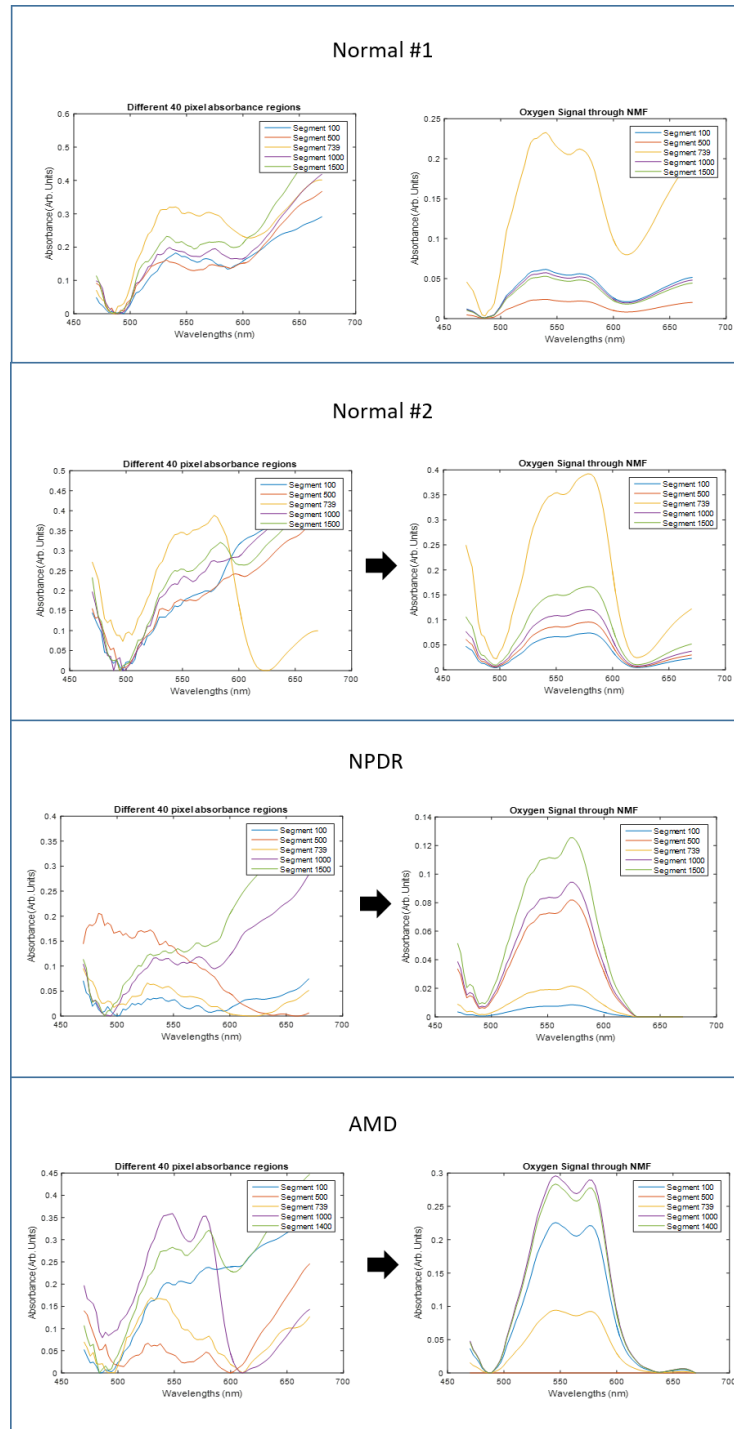


Figure 5-13. Results of NNMF decomposition for 5 segments in all 4 eyes. The left side contains the absorbance data at segments 100, 500, 739, 1000, and 1400/1500. The right side is the oxyhemoglobin oxygen signal weighted after performing NNMF

5.3.4. Oxyhemoglobin radial maps

The mean absorbance acquired at the five radial regions reveals the difference in magnitude between a normal eye and diseased eye with NPDR (Figure 5-14).

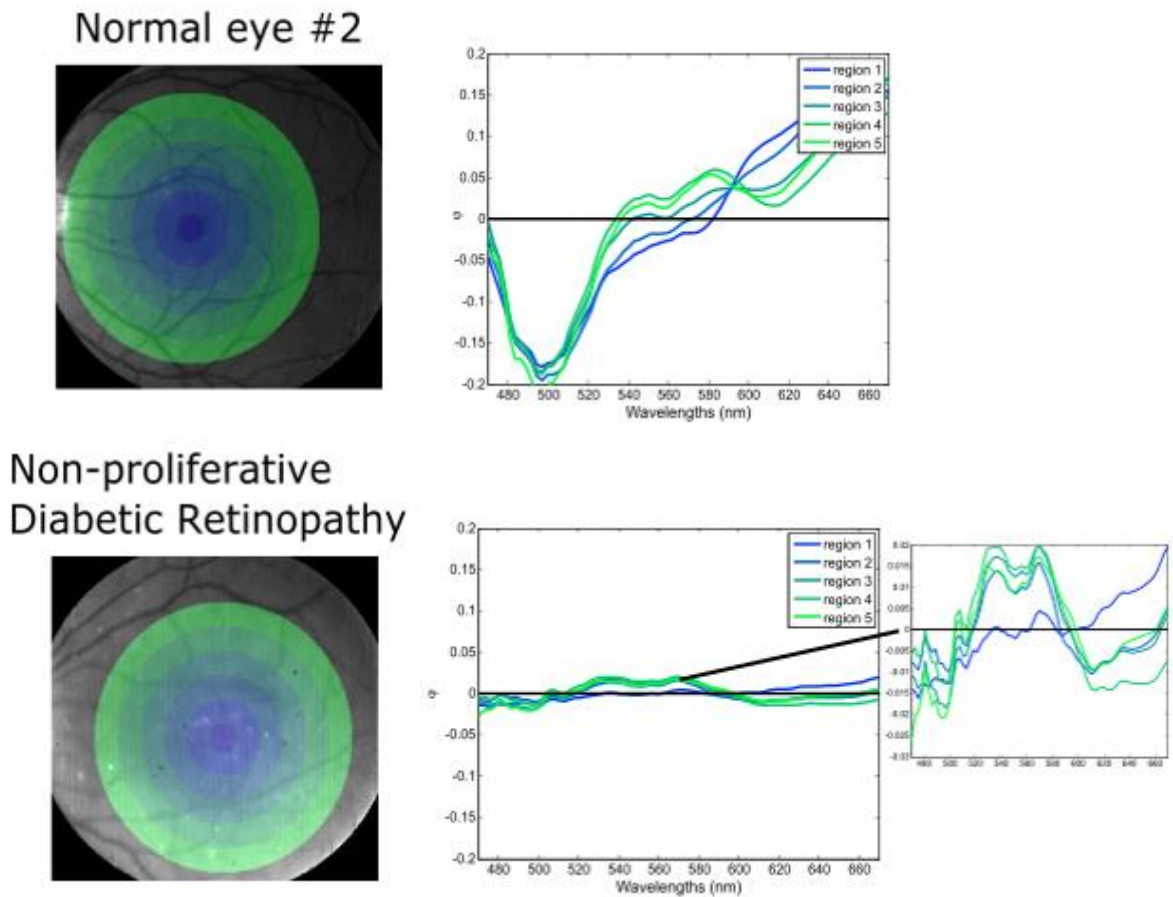


Figure 5-14. Mean absorbance from the 5 radial regions in the normal eye and the eye with NPDR.

OD NMF maps were created for all eyes using all segments from the radial maps. Each segment's value is the difference between the maximum OD peak between 540 and 580 nm and the OD value at 500 nm after NMF decomposition.

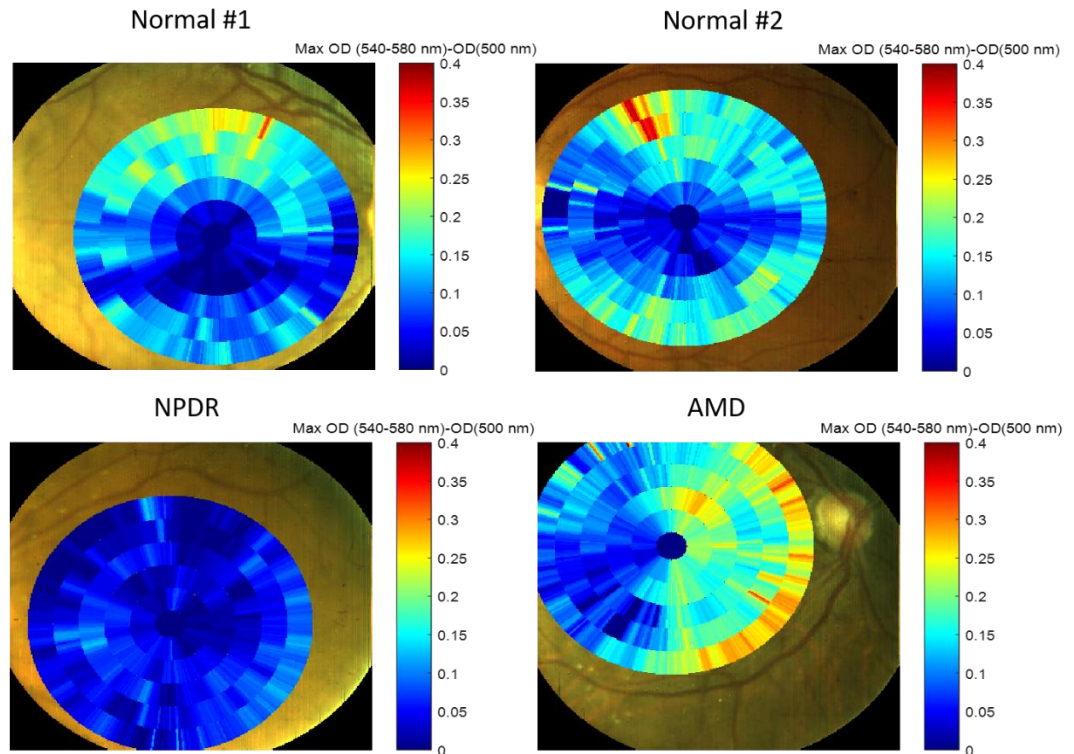


Figure 5-15. OD NMF maps for all eyes.

Using the values from the OD NMF radial maps and standards curve from the finger oximetry validation test (Figure 5-10), an HbO₂ concentration radial map was created for all eyes in Figure 5-16. These maps reveal different oxyhemoglobin abundance at different regions in the eye.

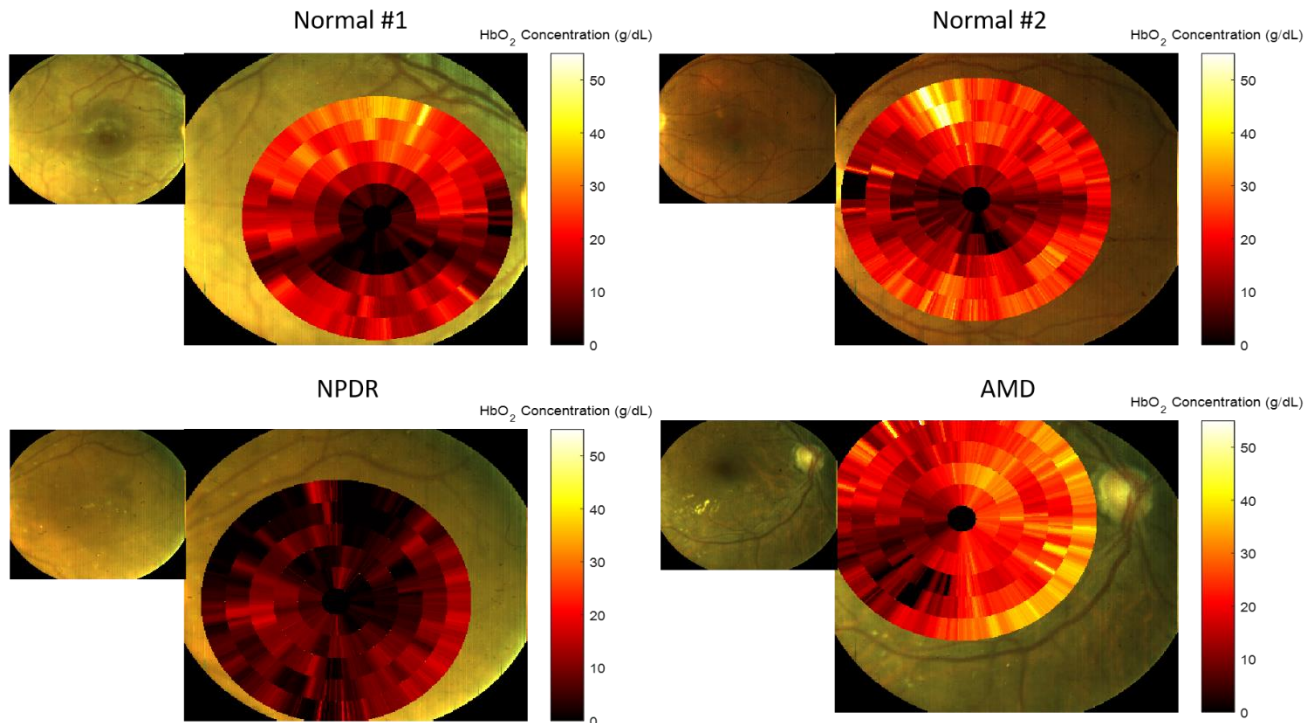


Figure 5-16. HbO₂ concentration maps for all eyes.

5.4. Discussion

The work presented here demonstrates to the best of our knowledge the first non-invasive estimation of oxygen abundance and oxygen concentration in the fundus tissue of the eye with non-resolvable vasculature. Distinct spectral peaks associated with oxyhemoglobin at 540 nm and 580 nm can be seen in Figure 5-14. As the radius increases in the map, the magnitude of these peaks increases, indicating increased oxygen content at different regions. This trend is validated by the finger

oximetry model and a prior knowledge of the vasculature distribution in the eye through FA results. Using the pulse oximeter reflectance images of a finger model, a standards curve could be generated, converting OD difference between a non-oxygen sensitive wavelength and an oxygen sensitive wavelength into oxyhemoglobin concentration based on the assumption that the OD signal scales linearly with oxyhemoglobin concentration. Since the spectral influence of macular pigment, melanin, and other chromophores cannot be entirely removed through division of different fundus regions, NNMF was employed to isolate a purer signal of oxyhemoglobin. Radial maps revealed clear differences between the normal eyes and diseased eyes. NPDR reveals low levels of oxygen concentration throughout the entire eye, supporting the theory of low perfusion in this disease. The normal eyes show symmetry in oxygen concentration between top and bottom halves of the eyes. A band of low oxygen concentration runs through both eyes in the center. This result supports the idea that vessels run from top to bottom, diverging into smaller and more dispersed capillaries as they approach the center of the eye. The radial map of AMD reveals an interesting result. The region populated by drusen is lower in oxyhemoglobin concentration relative to the rest of the eye. Potentially, these deposits disrupt the amount of oxygen that can be delivered to these regions; thus, they disrupt the health of the surrounding fundus tissue.

An interesting result was returned during the NNMF spectral decomposition. The normal eyes returned similar spectral endmember results and only required a rank 2 decomposition. It is probable that these eyes are more homogenous than the

diseased eyes; thus, simpler to unmix. Indeed, the absorbance spectra for five different regions in the diseased eyes reveal greater variation in their shape. This supports the idea that the diseases have a greater variation of chromophores throughout the eye, causing greater heterogeneity.

Future tests are being planned to further validate the accuracy and sensitivity of this new oximetry technique within the eye, but these initial results offer promising utility in the eye. The advantage of this technique over existing oximetry methods is the ability to co-locate an oximetry value over all regions of the eye. When diagnosing diseases and monitoring treatments, clinicians will have a greater ability to associate oxygen values with regions of interest.

Chapter 6

Conclusion

Fluorescence microscopy and biological imaging have seen an augmentation in the demand for snapshot hyperspectral imaging for scenarios that prioritize speed and light collection. For in vivo imaging, involuntary movements of the patient (e.g. eye saccades in fundus imaging) can hinder the effectiveness of scanning hyperspectral systems. In microscopic imaging, fluorophores can undergo photochemical alteration when exposed to large excitation energy; thus, restricting the amount of luminescence. Snapshot hyperspectral imaging offers utility to these situations. As the demand for more speed, efficiency, spectral and spatial data content for these imagers grows, the ability to record high fidelity spectral and spatial information becomes limited by the size of the detector. For example, sCMOS

detectors, which operate at better quantum efficiencies and faster speeds than their interline CCD counterparts, are increasing in popularity for biological applications; however the chip sizes are generally 75% smaller, limiting the total hyperspectral datacube size. This thesis presented a novel snapshot spectral imager capable of dynamically trading spatial content for spectral content in one integrated system to offset datacube limits set by present-day detectors and optics. By enabling “tunability”, a single snapshot imager can acquire a controllable amount of spectral and spatial information as dictated by the needs of the imaging scenario. The theory behind its operation and the construction of a working prototype were detailed. Future systems can be scaled up for improved performance with customized optics and mechanics. More tunability settings can also be achieved. This system will require additional optomechanics before its installation onto a fundus camera. The advantages that it provides should offer new insight into fundus imaging. Spectral resolution affects the accuracy of spectral unmixing and oximetry of the retina; however, limited detector space for snapshot imagers creates a trade-off between FOV and spectral resolution. LATIS can understand this trade-off and how it affects the quality of the spectral data. Additionally, LATIS can understand the differences in oximetry values between different imaging systems by observing the same region in the eye at different settings.

Retinal oximetry has enabled researchers to observe the oxygen metabolism within the retina. For example, increased venous oxygen saturation values have been correlated with decreased oxygen metabolism. HSI improves oximetry over existing

2-wavelength oximetry by reducing the influence of spectral noise, circumventing the need for extensive calibration, and enabling more sophisticated oximetry algorithms. We presented a calibration-free technique by which the oxygen saturation values in retinal vessels can be measured. By using the IMS, we investigated the IMS's ability to distinguish arteries and veins while measuring the absorbance in each vessel. The shape of the absorbance spectrum enabled us to estimate the oxygen saturation values. Presented here was the first demonstration of absolute oxygen saturation measurements in the eye using IMS technology, setting the foundation for improved oximetry algorithms and new SHSI systems for future data acquisition.

Retinal oximetry has yet to be integrated into the catalog of routine ophthalmology diagnostics despite its great use as a research tool. Limitations as to which regions of the eye can be measured and large intravessel variability preclude diagnostic power of these techniques. The IMS demonstrated the ability to utilize more sophisticated analytical tools and algorithms to extract measurements of oxygen content spectrally buried within regions of the fundus with no-resolvable vessels. The IMS due to its snapshot acquisition has clear advantages over scanning systems because it can perfectly synchronize with the flash of the fundus camera and mitigate the effects of eye movements. The radial maps presented here offer a novel and potentially important step towards improved retinal oximetry. We can co-locate oxyhemoglobin values with regions in the eye, extending beyond individual vessels. But possibly a more interesting consequence of this new technique is that we have demonstrated that the spectra can reveal dramatic differences between eyes based

clearly on the shape of the absorbance signatures. When the composite images of the eyes in Chapter 5 are compared, they look reasonably alike; however, the radial maps we have created revealed that each eye is spectrally unique. The results have indicated that the full appreciation of this uniqueness can only be obtained through hyperspectral imaging.

Future work will consist of moving forward with the installation of LATIS onto a fundus camera. For preliminary results, we will use a static LATIS before construction of a fully tunable system. Additionally, we will continue to improve the algorithms for retinal oximetry. Different unmixing methods may be employed in the future to separate not only oxyhemoglobin from the retina, but melanin, macular pigment, and deoxyhemoglobin. Blind source separation is a rapidly improving area, and there are algorithms that may be better suited for spectral unmixing of tissue.

References

Alabboud I, Muyo G., et. Al. "New spectral imaging techniques for blood oximetry in the retina," in Novel Optical Instrumentation for Biomedical Applications III, C. Depeursinge, ed., Vol. 6631 of Proceedings of SPIE-OSA Biomedical Optics (Optical Society of America, 2007), paper 6631_22.

Allington-Smith J and Content R, "Sampling and Background Subtraction in Fiber-Lenslet Integral Field Spectrographs," Publ. Astron. Soc. Pac. 110(752), 1216–1234 (1998).

Alm A and Bill A, "Blood flow and oxygen extraction in the cat uvea at normal and high intraocular pressures," Acta Physiol Scand 80: 19–28 (1970)

Ambati J., Atkinson JP, Gelfand BD, "Immunology of age-related macular degeneration," Nature Reviews Immunology 13, 438–451 (2013)

Bacon R, Adam G, Baranne A., Courtes G, Dubet D, Dubois JP, Emsellem E, Ferruit P, Georgelin Y, et. Al. "3D spectrography at high spatial resolution. I. Concept and realization of the integral field spectrograph TIGER," Astron. Astrophys. Supp. Ser. 113, 347 (1995).

Bacon R, Copin Y, Monnet G, Miller BW, Allington-Smith JR, Bureau M, Carollo CM, Davies RL, Emsellem E, Kuntschner H, Peletier RF, Verolme EK, and de Zeeuw PT, "The SAURON project–I. The panoramic integral-field spectrograph," Mon. Not. R. Astron. Soc. 326(1), 23–35 (2001).

Bacon R., "The integral field spectrograph TIGER: results and prospects," In *IAU Colloq. 149: Tridimensional Optical Spectroscopic Methods in Astrophysics*, G. Comte, M. Marcelin, ed. (Astronomical Society of the Pacific, 1995).

Battu R, Mohan A, Khanna A, et. al. Retinal oxygen saturation in retinitis pigmentosa and macular dystrophies in asian-Indian eyes. *Invest Ophthalmol Vis Sci*. 2015;56(5):2798-802.

Beach JM, Schwenzer KJ, Srinivas S, et al. Oximetry of retinal vessels by dual wavelength imaging: calibration and influence of pigmentation. *J Appl Physiol*. 1999;86(2):748-58.

Beatty S, Boulton M, Henson D, et al, "Macular pigment and age related macular degeneration," *British Journal of Ophthalmology* 1999;83:867-877

Bedard N., Schwarz RA, Hu A, Bhattar V, et. al., "Multimodal snapshot spectral imaging for oral cancer diagnostics: a pilot study," *Biomed. Opt. Express* 4(6), 938–949 (2013).

Bedard N., Hagen N., Gao L., and Tkaczyk T.S., "Image mapping spectrometry: calibration and characterization," *Opt. Eng.* 51(11), 111711 (2012).

Bodkin A, Sheinis A, Norton A, Daly J, Beaven S, and Weinheimer J, "Snapshot hyperspectral imaging: the hyperpixel array camera," *Proc. SPIE* 7334, 73340H (2009).

Bodkin A, Sheinis A, Norton A, Daly J, Roberts C, Beaven S, and Weinheimer J, "Video-rate chemical identification and visualization with snapshot hyperspectral imaging," *Proc. SPIE* 8374, 83740C (2012)

Bodkin A., Sheinis A., and Norton A., "Hyperspectral imaging systems," U.S. patent US20060072109 A1 (2006).

Bruton D. Color Science. <http://www.midnightkite.com/color.html>. Accessed April 23, 2016.

Chudakov DM, Lukyanov S, and Lukyanov KA, "Fluorescent proteins as a toolkit for in vivo imaging," *Trends Biotechnol.* 23(12), 605–13 (2005).

Collins JA, Rudenski A, Gibson J, Howard L, O'Driscoll R, "Relating oxygen partial pressure, saturation and content: the haemoglobin–oxygen dissociation curve," *Breathe*. 2015;11(3):194-201.

Courtes G, "An integral field spectrograph (IFS) for large telescopes," In *Instrumentation for Astronomy with Large Optical Telescopes*, C.M. Humphries, ed. (Springer Netherlands, 1982).

Courtes G, "Le télescope spatial et les grands télescope au sol," *Application de la Photométrie Bidimensionnelle à l'Astronomie* 1, 241 (1980).

Courtes G, Georgelin Y, R Bacon, et. al., "A New Device for Faint Objects High Resolution Imagery and Bidimensional Spectrography," In *Instrumentation for Ground-Based Optical Astronomy*, L.B. Robinson, ed. (Springer New York, 1988).

Cutler PJ, Malik MD, Liu S, Byars JM, DS Lidke DS, and Lidke KA, "Multi-Color Quantum Dot Tracking Using a High-Speed Hyperspectral Line-Scanning Microscope," *PLoS ONE* 8(5), e64320 (2013).

Delori FC, Pflibsen KP. Spectral reflectance of the human ocular fundus. *Appl Opt.* 1989;28(6):1061-77.

Delori FC. Noninvasive technique for oximetry of blood in retinal vessels. *Appl Opt.* 1988;27(6):1113-25.

Dwight J.G. and Tkaczyk T.S., "Lenslet array tunable snapshot imaging spectrometer (LATIS) for hyperspectral fluorescence microscopy," *Biomed. Opt. Express* 8(3), 1950–1964 (2017).

Elliott AD, Bedard N., Ustione A, Baird MA, Davidson MW, Tkaczyk TS, and Piston DW, "Imaging Live Cell Dynamics using Snapshot Hyperspectral Image Mapping Spectrometry," *Microsc. Microanal.* 19(S2), 168–169 (2013).

Elliott AD, Gao L, Ustione A., Bedard N., Kester R., Piston DW, and Tkaczyk TS, "Real-time hyperspectral fluorescence imaging of pancreatic β -cell dynamics with the image mapping spectrometer," *J. Cell Sci.* 125(20), 4833–4840 (2012).

Eysteinson T, Hardarson SH, Bragason D, et al. Retinal vessel oxygen saturation and vessel diameter in retinitis pigmentosa. *Acta Ophthalmol.* 2014;92(5):449-53.

Fawzi AA, Lee N, Acton JH, Laine AF, and Smith RT, "Recovery of macular pigment spectrum in vivo using hyperspectral image analysis," *J Biomed Opt.* 2011 Oct;16(10)

Ford BK, Volin CE, Murphy SM, Lynch RM, Descour MR, "Computed tomography-based spectral imaging for fluorescence microscopy," *Biophys J.* 2001 Feb;80(2):986-93.

Frank JG, Elder AD, Swartling J, Venkitaraman AR, Jeyasekharan AD and Kaminski CF, "A white light confocal microscope for spectrally resolved multidimensional imaging," *J. Microsc.* 227, 203–215 (2007)

Friedman DS, O'Colmain BJ, Munoz B, et al., "Prevalence of age-related macular degeneration in the United States," *Arch Ophthalmol*,122:564-572 (2004)

Galeano J, Jolivot R, Marzani F. Analysis of human skin hyper-spectral images by non-negative matrix factorization advances. *Soft Comput.* 2011; 7095:431–442

Gao L and Smith RT, "Optical hyperspectral imaging in microscopy and spectroscopy - a review of data acquisition," *J Biophotonics*. 2015 Jun; 8 (6):441-56

Gao L, Hagen N, Tkaczyk TS. Quantitative comparison between full-spectrum and filter-based imaging in hyperspectral fluorescence microscopy. *J Microsc*. 2012 May;246(2):113-23.

Gao L, Kester RT, and Tkaczyk TS, "Compact Image Slicing Spectrometer (ISS) for hyperspectral fluorescence microscopy," *Opt. Express* 17(15), 12293–12308 (2009).

Gao L, Kester RT, Hagen N, and Tkaczyk TS, "Snapshot Image Mapping Spectrometer (IMS) with high sampling density for hyperspectral microscopy," *Opt. Express* 18(14), 14330–14344 (2010).

Gao L, Kester RT, Tkaczyk TS. Compact Image Slicing Spectrometer (ISS) for hyperspectral fluorescence microscopy. *Opt Express*. 2009;17(15):12293-308.

Gao L, Smith RT, and Tkaczyk TS, "Snapshot hyperspectral retinal camera with the Image Mapping Spectrometer (IMS)," *Biomed. Opt. Express* 3(1), 48–54 (2012).

Geirsdottir A, Hardarson SH, Olafsdottir OB, et al. Retinal oxygen metabolism in exudative age-related macular degeneration. *Acta Ophthalmol*. 2014;92(1):27-33.

Geirsdottir A, Palsson O, Hardarson SH, et al. Retinal vessel oxygen saturation in healthy individuals. *Invest Ophthalmol Vis Sci*. 2012;53(9):5433-42.

Gorman A, Fletcher-Holmes D. W., Harvey A. R., "Generalization of the Lyot filter and its application to snapshot spectral imaging," *Opt. Express* 18(6), 5602–5608 (2010)

Gray H, "Anatomy of the Human Body," in *Anatomy of the Human Body*, Lewis WH ed. (Lea and Febiger), plate 514.

Hagen N, and Kudenov MW, "Review of snapshot spectral imaging technologies," *Opt. Eng*. 52(9), 090901--090901 (2013).

Hagen N, Kester R, Gao L. Snapshot advantage: a review of the light collection improvement for parallel high-dimensional measurement systems. *Opt Eng*. 2012;51(11).

Hammer M, Riemer T, Vilser W, et. al. A new imaging technique for retinal vessel oximetry: principles and first clinical results in patients with retinal arterial occlusion and diabetic retinopathy. *Proc. SPIE 716*. Available at:

<http://spie.org/Publications/Proceedings/Paper/10.1117/12.807817>. Accessed April 25, 2016.

Hammer M, Vilser W, Riemer T, et. al. Diabetic patients with retinopathy show increased retinal venous oxygen saturation. *Graefes Arch Clin Exp Ophthalmol*. 2009;247(8):1025-30.

Hammer M, Vilser W, Riemer T, et. al. Retinal vessel oximetry-calibration, compensation for vessel diameter and fundus pigmentation, and reproducibility. *J Biomed Opt*. 2008;13(5):054015.

Hardarson SH, Elfarsson A, Agnarsson BA, et al. Retinal oximetry in central retinal artery occlusion. *Acta Ophthalmol*. 2013;91(2):189-90.

Hardarson SH, Stefánsson E. Oxygen saturation in branch retinal vein occlusion. *Acta Ophthalmol*. 2012;90(5):466-70.

Hardarson SH, Stefánsson E. Oxygen saturation in central retinal vein occlusion. *Am J Ophthalmol*. 2010;150(6):871-5.

Hardarson SH, Stefánsson E. Retinal oxygen saturation is altered in diabetic retinopathy. *Br J Ophthalmol*. 2012;96(4):560-3.

Hardarson SH1, Harris A, Karlsson RA, et al. Automatic retinal oximetry. *Invest Ophthalmol Vis Sci*. 2006;47(11):5011-6.

Hardarson SH. Retinal oximetry. *Acta Ophthalmol*. 2013;91(5):489-90.

Hickam JB, Frayser R, Ross JC. A study of retinal venous blood oxygen saturation in human subjects by photographic means. *Circulation*. 1963; 27:375-85.

Hickam JB, Sieker HO., and Frayser R., "Studies of retinal circulation and A-V oxygen difference in man," *Trans Amer Clin Climat Ass* 71(34), 1959

Jaime GR, Kashani AH, Saati S. Acute variations in retinal vascular oxygen content in a rabbit model of retinal venous occlusion. *PLoS One*. 2012;7(11):e50179.

Johnson WR, Wilson DW, Fink W, Humayun M., and Bearman G, "Snapshot hyperspectral imaging in ophthalmology," *J. Biomed. Opt.* 12(1), 014036–014036 (2007).

Kashani AH, Kirkman E, Martin G, et. al. Hyperspectral computed tomographic imaging spectroscopy of vascular oxygen gradients in the rabbit retina in vivo. *PLoS One*. 2011;6(9):e2448.2

Kasili PM and Vo-Dinh T, "Hyperspectral imaging system using acousto-optic tunable filter for flow cytometry applications," *Cytometry Part A* 69A(8), 835–841 (2006).

Kester RT, Bedard N., Gao L, and Tkaczyk TS, "Real-time snapshot hyperspectral imaging endoscope," *J. Biomed. Opt.* 16(5), 056005--056005 (2011).

Khoobehi B, Beach JM, Kawano H. Hyperspectral imaging for measurement of oxygen saturation in the optic nerve head. *Invest Ophthalmol Vis Sci*. 2004; 5(5):1464-72.

Khoobehi B, Firn K, Rodebeck E, and Hay S., "A new snapshot hyperspectral imaging system to image optic nerve head tissue," *Acta Ophthalmol*. 92(3), e241--e241 (2014).

Khoobehi B, Firn K, Thompson H, et. al. Retinal arterial and venous oxygen saturation is altered in diabetic patients. *Invest Ophthalmol Vis Sci*. 2013;54(10):7103-6.

Khoobehi B, Khoobehi A, Fournier P. Snapshot hyperspectral imaging to measure oxygen saturation in the retina using fiber bundle and multi-slit spectrometer. *Proc. SPIE 8229*. Available at: <http://proceedings.spiedigitallibrary.org/proceeding.aspx?articleid=1344452>. Accessed April 24, 2016.

Konecky SD, Wilson RH, Hagen N, et al, "Hyperspectral optical tomography of intrinsic signals in the rat cortex," *Neurophoton*. 0001;2(4):045003.

Kristjansdottir JV, Hardarson SH, Harvey AR, et al. Choroidal oximetry with a noninvasive spectrophotometric oximeter. *Invest Ophthalmol Vis Sci*. 2013;54(5):3234-9.

Kudenov MW and Dereniak EL, "Compact real-time birefringent imaging spectrometer," *Opt. Express* 20, 17973-17986 (2012)

Laing RA, Cohen AJ, Friedman E. Photographic measurements of retinal blood oxygen saturation: falling saturation rabbit experiments. *Invest Ophthalmol*. 1975;14(8):606-10.

Larson J.M., "The Nikon C1si combines high spectral resolution, high sensitivity, and high acquisition speed," *Cytometry Part A* 69(8), 825–834 (2006).

Lee D, Haynes R, Ren D, and Allington-Smith J, "Characterization of lenslet arrays for astronomical spectroscopy," *PASP* 113(789), 1406 (2001).

Lee N, Wielaard J, Fawzi AA, et. al. In vivo snapshot hyperspectral image analysis of age-related macular degeneration. *Conf Proc IEEE Eng Med Biol Soc.* 2010;2010:5363-6

Lee N, Wielaard J, Fawzi AA, Sajda P, Laine AF, Martin G, Humayun MS, and Smith RT, "In vivo snapshot hyperspectral image analysis of age-related macular degeneration," *Conf Proc IEEE Eng Med Biol Soc.* 2010; 2010:5363-6.

Lerner JM, "Imaging Spectrometer Fundamentals for Researchers in the Biosciences--A Tutorial," *Cytometry Part A* 69A:712–734 (2006)

Lichtman JW and Conchello JA, "Fluorescence microscopy," *Nat. Methods* 2(12), 910–9 (2005).

Lu G and Fei B, "Medical hyperspectral imaging: a review," *J. Biomed. Opt.* 19(1):010901 (2014)

Marmor MF, "Retinal Pigment Epithelium," in *Ophthalmology*, (Elsevier, 2014), pp 423-425.

Mathieu E., Gupta N., Macdonald R.L., AI J., and Yucel Y.H. Yucel, "In Vivo Imaging of Lymphatic Drainage of Cerebrospinal Fluid in Mouse," *Fluids Barriers CNS* 35(10), (2013).

Meinke M, Müller G, Helfmann J, et. al. Empirical model functions to calculate hematocrit-dependent optical properties of human blood. *Appl Opt.* 2007;46(10):1742-53.

Michelson G, Scibor M. Intravascular oxygen saturation in retinal vessels in normal subjects and open-angle glaucoma subjects. *Acta Ophthalmol Scand.* 2006;84(3):289-95.

Montcuquet AS, Herve L., et. al, "Nonnegative matrix factorization: a blind spectra separation method for in vivo fluorescent optical imaging," *Journal of Biomedical Optics*, Society of Photo-optical Instrumentation Engineers, 2010, 15 (5), pp.0560091-14.

Mordant DJ, Al-Abboud I, Muyo G, et. al. Oxygen saturation measurements of the retinal vasculature in treated asymmetrical primary open-angle glaucoma using hyperspectral imaging. *Eye (Lond)*. 2014;28(10):1190-200.

Mordant DJ, Al-Abboud I, Muyo G, et. al. Spectral imaging of the retina. *Eye (Lond)*. 2011;25(3):309-20.

Nunes RP, Rosenfeld PJ, Filho CA, Yehoshua Z, Martidis A, Tennant MTS, "Age-Related Macular Degeneration," in *Ophthalmology*, (Elsevier, 2014), pp 423-425.

Olafsdottir OB, Hardarson SH, Gottfredsdottir MS, et. al. Retinal oximetry in primary open-angle glaucoma. *Invest Ophthalmol Vis Sci*. 2011;52(9):6409-13.

Olafsdottir OB, Vandewalle E, Abegão Pinto L, Geirsdottir A, et. al. Retinal oxygen metabolism in healthy subjects and glaucoma patients. *Br J Ophthalmol*. 2014;98(3):329-33.

Paatero P and Tapper U, "Positive matrix factorization: A non-negative factor model with optimal utilization of error estimates of data values," *Environmetrics* 5(2), 111-126 (1994)

pco.edge. sCMOS Cutting Edge Imaging. v1.00. 1-15.

Pietraszewska-Bogiel A and Gadella TW, "FRET microscopy: from principle to routine technology in cell biology," *J. Microsc*. 241(2), 111-8 (2011).

Pollreisz A, Magdalena B, Katharina K, et. al., "Retinal oximetry in eyes with geographic atrophy due to age-related macular degeneration. *Invest. Ophthalmol. Vis. Sci*. 55(13):5893 (2014)

Regatieri CVS, Roh S, Weiter JJ, "Retinal and Choroidal Circulation," in *Ophthalmology*, (Elsevier, 2014), pp 426-429

Resnikoff S., Pascolini D., et. al., "Global data on visual impairment in the year 2002," *Bull World Health Organ*. 82(11):844-51 (2004)

Schultz RA, Nielsen RT, Zavaleta JR, Ruch R, Wyatt R, and Garner HR, "Hyperspectral imaging: A novel approach for microscopic analysis," *Cytometry* 43(4), 239-247 (2001).

Schweitzer D, Hammer M, Kraft J. In vivo measurement of the oxygen saturation of retinal vessels in healthy volunteers. *IEEE Trans Biomed Eng*. 1999;46(12):1454-65.

Schweitzer D, Leistriz L, Hammer M, et. al. Calibration- free measurement of the oxygen saturation in human retinal vessels. *Proc. SPIE 239*. Available at: <http://proceedings.spiedigitallibrary.org/proceeding.aspx?articleid=988525>. Accessed April 24, 2016.

Schweitzer D, Thamm E, Hammer M. A new method for the measurement of oxygen saturation at the human ocular fundus. *Int Ophthalmol*. 2001;23(4-6):347-53.

Semiconductor Components Industries, LLC. KAI-16000 Image Sensor 4872 (H) X 3248 (V) Interline CCD Image Sensor. Device Performance Specification. Revision 6. 2012. 1

Sinclair MB, Haaland DM, Timlin JA, and Jones HDT, "Hyperspectral confocal microscope," *Appl. Opt.* 45, 6283–6291 (2006).

Smith MH, Denninghoff KR, Lompado A, et al. Effect of multiple light paths on retinal vessel oximetry. *Appl Opt.* 2000;39(7):1183-93.

Smith MH, Denninghoff KR, Lompado A, et al. Minimizing the influence of fundus pigmentation on retinal vessel oximetry measurements. *Proc. SPIE*. 2001;11: 135-145.

Smith MH. Optimum wavelength combinations for retinal vessel oximetry. *Appl Opt.* 1999;38(1):258-67.

Smith RT, Post R, Johri A, et al., "Simultaneous decomposition of multiple hyperspectral data sets: signal recovery of unknown fluorophores in the retinal pigment epithelium. *Biomedical Optics Express*. 2014; 5(12)

Sparks WB and Ford HC, "Imaging spectroscopy for extrasolar planet detection," *Astrophys. J.* 578(1), 543 (2002).

Sutherland VL, Timlin JA, Nieman LT, et. al., "Advanced imaging of multiple mRNAs in brain tissue using a custom hyperspectral imager and multivariate curve resolution," *J. Neurosci. Methods* 160(1), 144–148 (2007).

T. Zimmermann, "Spectral imaging and linear unmixing in light microscopy," *Adv. Biochem. Eng. Biotechnol.* 95, 245–265 (2005).

Tkachuk DC, Pinkel D, Kuo WL, Weier HU, and Gray JW, "Clinical applications of fluorescence in situ hybridization," *Genet. Anal Tech. Appl.* 8(2), 67–74 (1991).

Toomre DK, Langhorst MF, and Davidson MW, "Introduction to Spinning Disk Confocal Microscopy," <http://zeiss-campus.magnet.fsu.edu/articles/spinningdisk/introduction.html>.

Tornquist P and Alm A, "Retinal and choroidal contribution to retinal metabolism in vivo. A study in pigs," *Acta Physiol Scand* 106: 351–357. (1979)

Ueda-Consolvo T, Fuchizawa C, Otsuka M. Analysis of retinal vessels in eyes with retinitis pigmentosa by retinal oximeter. *Acta Ophthalmol.* 2015;93(6):e446-50.

Vane G, Green RO, Chrien RG, Enmark HT, Hansen EG, and Porter WM, "The airborne visible/infrared imaging spectrometer (AVIRIS)," *Remote Sens. Environ.* 44(2-3), 127–143 (1993).

Vermaas WF, Timlin JA, Jones HD, Sinclair MB, Nieman LT, Hamad SW, DK Melgaard, and Haaland DM, "In vivo hyperspectral confocal fluorescence imaging to determine pigment localization and distribution in cyanobacterial cells," *PNAS* 105(10), 4050–4055 (2008).

Wagadarikar AA, Pitsianis NP, Sun X, and Brady DJ, "Video rate spectral imaging using a coded aperture snapshot spectral imager," *Opt. Express* 17, 6368-6388 (2009)

WK Ma, JM Bioucas-Dias, et. al, "A Signal processing perspective on hyperspectral unmixing: insights from remote sensing," *IEEE Signal Process* 31(1). 2014

Woltman SJ, Jay GD, and Crawford GP, "Liquid-crystal materials find a new order in biomedical applications," *Nature Materials* 6, 929–938 (2007).

Yu D, Cringle SJ. Oxygen Distribution and Consumption within the Retina in Vascularised and Avascular Retinas and in Animal Models of Retinal Disease. *Prog Retin Eye Res* 2001;20:175-208.

Zimmermann T, Rietdorf J, and Pepperkok R, "Spectral imaging and its applications in live cell Microscopy," *FEBS Lett.* 546(1), 87–92 (2003).

Zong Y, Lin L, Yi C. Retinal vessel oxygen saturation and vessel diameter in retinitis pigmentosa at various ages. *Graefes Arch Clin Exp Ophthalmol.* 2016;254(2):243-52